Persistent Homology Tools for
Image Analysis

By

Aras Tawfeeq Asaad

School of Computing

University of Buckingham

United Kingdom

A thesis

Submitted for the Degree of Doctor of Philosophy in

Mathematics to the School of Computing in

The University of Buckingham

January 2020

ABSTRACT

Topological Data Analysis (TDA) is a new field of mathematics emerged rapidly since the first decade of the century from various works of algebraic topology and geometry. The goal of TDA and its main tool of persistent homology (PH) is to provide topological insight into complex and high dimensional datasets. We take this premise onboard to get more topological insight from digital image analysis and quantify tiny low-level distortion that are undetectable except possibly by highly trained persons. Such image distortion could be caused intentionally (e.g. by morphing and steganography) or naturally in abnormal human tissue/organ scan images as a result of onset of cancer or other diseases.

The main objective of this thesis is to design new image analysis tools based on persistent homological invariants representing simplicial complexes on sets of pixel landmarks over a sequence of distance resolutions. We first start by proposing innovative automatic techniques to select image pixel landmarks to build a variety of simplicial topologies from a single image. Effectiveness of each image landmark selection demonstrated by testing on different image tampering problems such as morphed face detection, steganalysis and breast tumour detection.

Vietoris-Rips simplicial complexes constructed based on the image landmarks at an increasing distance threshold and topological (homological) features computed at each threshold and summarized in a form known as persistent barcodes. We vectorise the space of persistent barcodes using a technique known as persistent binning where we demonstrated the strength of it for various image analysis purposes. Different machine learning approaches are adopted to develop automatic detection of tiny texture distortion in many image analysis applications. Homological invariants used in this thesis are the 0 and 1 dimensional Betti numbers.

We developed an innovative approach to design persistent homology (PH) based algorithms for automatic detection of the above described types of image distortion. In particular, we developed the first PH-detector of morphing attacks on passport face biometric images. We shall demonstrate significant accuracy of 2 such morph detection algorithms with 4 types of automatically extracted image landmarks: Local Binary patterns (LBP), 8-neighbour super-pixels (8NSP), Radial-LBP (R-LBP) and

centre-symmetric LBP (CS-LBP). Using any of these techniques yields several persistent barcodes that summarise persistent topological features that help gaining insights into complex hidden structures not amenable by other image analysis methods.

We shall also demonstrate significant success of a similarly developed PH-based universal steganalysis tool capable for the detection of secret messages hidden inside digital images. We also argue through a pilot study that building PH records from digital images can differentiate breast malignant tumours from benign tumours using digital mammographic images.

The research presented in this thesis creates new opportunities to build real applications based on TDA and demonstrate many research challenges in a variety of image processing/analysis tasks. For example, we describe a TDA-based exemplar image inpainting technique (TEBI), superior to existing exemplar algorithm, for the reconstruction of missing image regions.

I dedicate my thesis to my wife Suriyah

And

To my family

ACKNOWLEDGMENT

ABBREVIATIONS

8-NSP	8 Neighbour Superpixels
ABC	Automatic Border Control
Acc	Accuracy
B_k	Betti number in dimension k
$\mathcal{C}_k$	Chain complex at dimension k
CNN	Convolutional Neural Networks
CS-LBP	Centre-Symmetric Local Binary Patterns
DDSM	Digital Database for Screening Mammography
EBI	Exemplar-based Inpainting
eMRTD	Electronic Machine-Readable Travel Documents
FNR	False Negative Rate
FPR	False Positive Rate
H_k	Homology groups at dimension k
ISOMAPS	Isometric Mappings
KNN	k-Nearest Neighbour
LBP	Local Binary Patterns
LSB	Least Significant Bit
MDS	Multi-Dimensional Scaling
Mini-MIAS	Mini Mammographic Image Analysis Society
P&S	Print-scanned
PH	Persistent Homology
PID	Principle Ideal Domain
R-LBP	Radial-Local Binary Patterns
Rips	Vietoris-Rips
SC	Simplicial Complexes
SNF	Smith Normal Form
ISOMAPS	Isometric Mappings
$\mathbb{S}$	Simplicial Complex set
STEM	Science Technology Engineering and Mathematics
SUNIWARD	Spatial Universal Wavelet Relative Distortion
SVM	Support Vector Machines

TDA	Topological Data Analysis
TEBI	Topological Exemplar-based Inpainting
TNR	True Negative Rate
TPR	True Positive Rate
ULBP	Uniform Local Binary Patterns
∂_k	Boundary operator of dimension k
σ	simplex

CONTENTS

LIST OF FIGURES

LIST OF TABLES

DECLARATION

I, hereby declare that presented work has not previously been submitted towards any qualification degree or diploma in the University of Buckingham or any other university.

I also declare that to the best of my knowledge and belief, the thesis contains no material previously published or written by another person except where due reference is made in the thesis itself.

Aras Tawfeeq Asaad

Chapter 1

Introduction

Nowadays in almost all areas of science, engineering and even social sciences we store and gather data from different types of activities at an ever-increasing rate. This is due to the availability of affordable high-performance powerful computing devices on one hand, and the emergence of new innovative computational paradigms of data analysis on the other hand. The generated data vary considerably in terms of complexity, volume, diversity and quality. In applications where one deals with data records of high-dimensional numerical type, non-numerical descriptive/ordinal type, or of mixed types, the challenge of visualizing/comprehending the collected data is far beyond human capabilities. Realistically, such applications are only susceptible to analysis by machine learning based software inspired and guided by rigours mathematical concepts and techniques. Moreover, recent BigData and computer vision applications provide ample evidences of the claim that "Data has shapes" and incentivise the use of known topological invariants of shapes for advanced approaches to data analysis [1]. Indeed, this has naturally energised research interest in using computational topology and its tools as means of understanding shapes of data leading to the emergence of the field of *Topological Data Analysis* (*TDA*). In turn, the emergence of TDA over the last few years, generated new challenges in computational topology investigations of which could have significant implications on data analysis and beyond. This thesis aims to investigate and present a new strategy for the development of innovative TDA-based image analysis and forensic schemes. We are generally interested in detecting image distortions that could occur intentionally, maliciously or as a result of changes in the imaged objects such as disease-related changes to scanned human tissue/organs. Our main case study application will focus on malicious detection of morphing attacks on face images which is becoming a serious threat to biometric based identification. Our strategy will be based on extracting simplicial complexes of image landmarks and computing the topological invariants of which are sensitive to tiny image distortions.

The first two sections of this introductory chapter are concerned with the problem statements of research conducted in this thesis. We first describe the general area of data analysis and how the field of TDA emerged, before describing the problem of image tampering detection. In the rest of the chapter, we present the main aim and objectives of the research project, describe main challenges and existing approaches, our strategy and contributions, and thesis organisation.

1.1 Introduction to Data Analysis

Data analysis is not a new field of research. Mathematics and scientific endeavours, throughout the human history, are based on collecting data and observations about events and objects, build concise models of the collected data, and invent increasingly more advanced algorithms to extract information and create knowledge. Indeed, mathematical modelling, statistical analysis and various other fields of mathematics were developed for the purposes of interpreting data, discovering patterns, and making predictions. Moreover, the more analysis capabilities were developed the more data analysis became tractable and this dynamical relationship remains a distinctive characteristic of human endeavours. Naturally, the advents of computer and communication technologies quickened the pace of progress and led to the emergence of more sophisticated applications as well as tougher challenges in data analysis. With this, methods of analysis became more complex and the need for automation resulted in the development of a variety of machine learning tools and models, the latest being Deep Learning schemes using various convolutional neural network (CNN) models.

In general, data analysis applications involve a set of objects/events represented by data records and the challenge is to search for patterns of relationships between groups of the underlying objects/events. More and more, the data records are becoming more complex in terms of dimensionality, volume, and mix of types. For example, in the health service a patient record consists of a combinations of personal identifier data, x-ray and MRI images, history of illnesses, treatments, surgeries, etc. Analysis of such complex dataset is a serious challenge well beyond conventional statistical analysis and even more sophisticated tools. The emergence of a variety of deep learning architecture models and the rapid growth in their deployment may be seen as diminishing the need for more research in data analysis. However, such models work as black box, without interpreting its decisions, and have many

shortcomings in terms of overfitting and vulnerability to adversarial attacks [2]. Ironically, the only obvious explanation of their high performances, in image analysis applications, is attributed to the massive amounts of extracted features. Indeed, explaining deep learning decisions suffers from the effect of "curse of features" analogous to the challenge of curse of dimension that is apparent in image processing/analysis [3].

Regardless of the data records complexity, in data analysis applications one needs some means of measuring similarity/distances between pairs of records in terms of which the analysis tasks are meant to discover hidden informative patterns of similarity/dissimilarity. Discovering hidden data patterns is akin to clustering the data in terms of the similarity information. Consequently, data analysis maybe characterised as cluster analysis tasks that can naturally benefit from network analysis problems where the records are associated with the nodes and arcs connecting two nodes are given weights of the similarity measure between the end nodes.

Focusing on pairwise relations/similarities was one of the fundamental building blocks of mining bigdata that have been extensively investigated in the past [4]. In general, the larger the volume of the data records and/or the dimensionality of the numerical data records present major challenges in terms of efficiency of operations and sensitivity to noise besides difficulties in interpreting the results. Accordingly, ample research were, and are, conducted to reduce dimensionality of records with minimal loss of information and in creating visualisation tools to help humans to interpret/justify decisions.

For image analysis applications, dealing with the volume and dimensionality challenges is a common source of investigations and dimension reduction is, to some extent, a dominant mitigating approach. Variants of the principle component analysis (PCA) and compressive sensing based random projections are only few examples of these approaches. But most have limitations and shortcomings [5][6]. However, over the years researchers investigating the analysis/classification of high dimensional data records, questioned the wisdom of modelling the records by a linear metric space (e.g. Euclidean) and considered the possibility that such data may reside on (or approximated by) a lower dimensional sub-manifold. Nonlinear dimension reduction techniques have been developed for the purpose of manifold learning/modelling of

high dimensional data including: Multi-dimensional Scaling (MDS), isometric mapping methods (ISOMAPS), Laplacian Eigenmaps and Spectral techniques. Unlike the linear dimension reduction schemes, most of these schemes ignore the internal structures of the data records, associated with coordinates/entries, of the actual records and generally work by finding a configuration of points in a low-dimensional space whose distance matrix approximates that of the original data records. Point configurations in 2 or 3 dimensions are perfect for visualization of the clustering of the data records in terms of the intended analysis. However, it is not clear how can one discern characterizing information on the contents of the original records, in particular for images and high dimensional data records.

Many applications greatly benefit from both approaches in terms of performance and efficiency, but two main shortcomings obstruct the chance of achieving reliable analysis. While linear dimension reduction helps mitigating the sever effects of curse of dimension, the projected image data remain of relatively large dimension, and the shape generated by the specific application samples continue to be treated as a linear metric space. On the other hand, manifold learning techniques incorporate nonlinear distance functions for curved shapes of the record samples, they do not seem to provide means of determining the characterising topological features of the learnt manifolds (i.e. the number of connected components, holes, tunnels, etc.).

The manifold learning schemes, mentioned above, rely on the basic assumption that, in many data analysis applications, the data records are sampled from a low-dimensional manifold shape embedded in a high-dimensional space. Indeed, there has been plenty of applications where data have been suspected to have some recognisable shapes. By the shape of data, we mean the 'global shape' of data which may supply useful information concerning the underlying phenomena which the data represents. Building and studying shape of data/objects is the core concern of the well-known branch of mathematics known as topology. The most image-relevant example of this, is the excellent mathematical demonstration that the space of normalised high-contrast 3x3 patches (i.e. 9-dimensional data records) of natural images are mappable onto the points of the 2-dimensional, Riemann surface of a Klein Bottle [7][8]. Interestingly, this was established without using linear/non-linear dimension reduction. Instead it exploited the fact that high contrast 3x3 image patches convey texture information. This result establishes the well understood Klein Bottle

manifold as the space of all positions of the 3x3 patches of natural images (i.e. its so-called Phase space). It shows that image analysis could benefit greatly by focussing on local texture features as a source of discriminating different groups of images. In this respect, we recall that the concept of "feature" selection is a well-known and practiced in some data analysis applications, that involve large number of feature fields (i.e. coordinates not necessarily all real numbers), using some criteria that selects the coordinates that are most relevant to the intended analysis. It is worth noting that conventional linear dimension reduction, for image applications, is based on selecting features that are based on linear combinations of image pixels [6], but these features may depend on pixels spread out in the image that are useful in reducing redundancies rather than being associated with texture features essential for image analysis. These results and considerations suggest that certain types of image analysis applications can greatly benefit from feature selection, by extracting certain texture-based features, and investigate the topological parameters of their spatial distributions. The approaches to image analysis adopted in this thesis are to some extent influenced by these hypotheses and uses algebraic topology tools to distinguish between the topological shapes of image landmarks determined by certain types of local image features extracted from the sought after different classes of images. The most prominent such tool is that of Persistent Homology (PH) that determines the pattern of changes to the characterising topological parameters of simplicial complex shapes, of the chosen landmarks, at a monotonically increasing finite sequences of distance/similarity thresholds. This topological approach benefits from the availability of rich research resources accumulated over several decades, while its suitability stems from the fact that the topology of simplicial complexes is invariant under small deformations, independent of landmark coordinate representation. The PH tool provides a compressed topological representation of data shapes which can be computed and analysed efficiently regardless of the complexity of the data records. The PH of a data shape can be visualised in terms of a set of barcodes (one for each topological invariant such as number of connected components, number of holes…etc.).

1.2 The Focus of Image Tampering/Degradation Problem

In general, image analysis is a set of computer vision methods aim to extract useful information from digital images, automatically or semi-automatically, that can be

used to distinguish different classes of images depending on the objective(s) of the specific application. It provides a descriptive/numeric output to each input image, and it may be preceded by some image processing techniques for quality enhancement, denoising, restoration, and/or segmentation. A major type of image analysis applications is that of classification/identification, such as face biometrics, whereby task-related image features (mainly texture/structure related) are extracted and represented in a certain format (such as texture statistics and histograms) to be input into some classification tools. The adopted classifier either determine the appropriate class to which the image belongs to and/or output a probability that this is true. Image classification algorithms work by the assumption that the input image has one or more features whose representations are shared by images belonging to a unique class. The determination of class discriminating features is done through a training process using sufficiently large dataset of image samples drawn meant to be a good representative of the relevant image population. The training process is either supervised (where the class of the training samples are known) or unsupervised where the features are meant to partitioned into distinguishable classes. In a supervised classification framework, an analyst specifies the class beforehand whereas in an unsupervised scenario the classes will be automatically specified through clustering-like methods. In this thesis, we are mainly interested in investigating Topological image analysis for automatic binary image classification schemes, i.e. when the aim is to discriminate images into two classes of images. The areas of such applications include a variety of multi-media security and medical abnormality diagnostics of scanned body tissues/organs. In such applications, the target image classes are expected to differ at the microscale of texture that are not visibly detectable, although in the medical field highly trained clinician may have own established quantitative and qualitative rules to predict an image class. By no means, confining our investigations to the above-mentioned range of classification challenges is a limitation of the application of topological image analysis. We shall now describe briefly the motivation for our choice, by illustrating the growing range of computer vision applications that require the type of analysis covered by our specific scenario.

The availability of a variety of sophisticated image processing tools made the task of image manipulation to be easy without leaving visual traces. Image tampering can include changes which are not malicious, i.e. the intention is not to change the overall

message the image conveys, and also changes where the sole purpose is to alter the truth in which the image represents. Adding/removing noise, blurring, changing lighting condition, inpainting, cropping, resizing are examples of image processing tasks that manipulate the image either maliciously or for beautification purposes. The ease with which digital images/videos are manipulated/faked together with the wide spread of internet and social media platforms, raises serious ethical issues not only about the integrity of digital images but have adverse implications in every aspects of local/global economic and political activities. Therefore, discriminating genuine digital images from manipulated ones is of a strong demand by media forensic community in one hand, and by the public to access the truth on the other hand.

Several morph detection algorithms proposed and investigated in the last few years whereby the majority of them rely on statistical measurements of texture features and mainly build on the wealth knowledge in the field of media forensics. This thesis is motivated by rapid advances in the field of Topological Data Analysis. In particular, Persistent Homology (PH), the main tool in TDA, associated with automatically selected image landmarks used to design sophisticated morph detection algorithms.

Another area that results in image manipulation is in *steganography* whereby secret messages are embedded in innocuous images without distorting the visual quality of the image. Steganalysis, is the science of detecting hidden messages inside digital images. Regardless of the robustness of the secret embedding method, existing steganalysis tools expect that tiny local texture-information will be distorted one way or another. Hence, TDA is expected to provide effective tools for detection of hidden messages by analysing local tiny distortion/tampering.

In biomedical image classification, the task of classifying scan images into different disease related categories is becoming an essential part of health care system that is well beyond the human expert resources of most national health services. For instance, detecting ovarian or breast cancer in an early stage through images to help speeding up the diagnostic process is of a great importance due to the high number of cases in UK and around the world. Growing evidence from systems biology research into cancer, demonstrate that cancer cells spread within a body tissue by changing cellular networks of the texture of cysts [9]. This is a strong indication to the viability

of using TDA to classify image scans of tissue tumor into benign and malignant cases.

In summary, we investigate the use of TDA for the detection of image tampering in general, and building TDA tools for automatic detection of malicious face image morphing attacks in particular. We shall also demonstrate applicability of the developed TDA image analysis schemes to detect a variety of image distortion including disease caused distortion of tissue/organ scan images as well as a Steganalysis tool to detect hidden secret transactions.

1.3 Thesis Objectives

TDA witnessed considerable success in recent years by providing a new innovative paradigm to solve a variety of complex data analysis problems (e.g. [10],[11],[12]). However, there are a number of challenges in using the theory of TDA, the most obvious being the selection of an appropriate data model with topological characteristics that enables the construction of a simplicial complex filtration given a sample data records or their representation. This allows the computation of the PH of the data shape using persistent barcodes and/or persistent diagram. The appropriate choice should make the representation of the corresponding PH sensitive to the purpose of the data analysis. For image analysis, we remind the reader that in our approach the images themselves are not the node of the simplicial complexes (SC), but rather we build SCs from sets of specific texture features associated with image landmarks. On the other hand, from application point of view, many image tampering approaches tend to ignore the rich topological information one can extract to gain more insight about different tampering problems. With these limitations in mind, this thesis seeks to achieve the following objectives:

- Developing automatic techniques to choose various image landmarks to facilitate the constructing of a filtration of their simplicial complexes.
- Extracting topological parameters of the landmarks SC filtrations from persistent barcodes, that are sensitive to the image tampering act (i.e. highly discriminative of different image classes of interest).
- Conducting extensive experimental investigation to illustrate the effectiveness of the proposed image landmarks and persistent barcode information extraction on large image datasets gathered from different domains.

- Developing innovative PH-based morph detection algorithms which relies on the discriminating power of the pattern of change in homological features extracted from filtered simplicial complexes build on image landmarks. Beside 'digital' images, we are investigating the print-scanned (P&S) images which are closer to real life scenarios.

- Investigating the use of TDA scheme as an image quality assessment. Especially, to assess the presence of shadows and blurring as well as detecting image alteration as a result of applying different image inpainting algorithms. Also, improving current digital image inpainting techniques using ideas from TDA where we proposed a topological exemplar-based inpainting method that outperforms state-of-the-art exemplar-based inpainting approaches.

- Proposing TDA-based steganalysis tool to detect 'stego' images where a secret message being hidden by different steganographic techniques.

- Establishing the 'Persistent classification' approach for tampered digital images which is critical in realizing the effect of PH in image classification stage.

To fulfill above objectives, we mainly investigate the use of different approaches of image landmark selection and benefit from the wealth topological information developed recently in the mathematical field of TDA.

1.4 Thesis Contributions

The research conducted in this thesis achieved a number of contributions which provide innovative way of designing image tampering detection algorithms that depend on TDA. It also provides new techniques where one can build topology from digital images from a variety of image analysis purposes. Hence, the research in this thesis claims the following major contributions:

1. The first contribution of this thesis is proposing novel automatic image landmark selection procedures to build topology from digital images. Specifically, four techniques proposed in which they are based on uniform local binary patterns (ULBP), centre-symmetric LBP (CS-LBP), radial LBP (R-LBP) and 8-neighbor superpixels (8-NSP). The effectiveness of these techniques is investigated extensively on large image datasets and for

different image tampering detection purposes such as morphing detection, steganalysis and image quality assessment.

2. A novel feature extraction method introduced to summarize topological inference from the space of persistent barcodes, which we call Persistent Binning. Furthermore, we partition the space of persistent barcodes into P_i −equidistance partition and observe the number of d-dimensional homology groups at each i, where $i = 0,1,2, … ,100$ and $d = \{0,1\}$. We show that the topological features summarized in this manner , from persistent barcodes, are sensitive to different image tampering tasks.

3. Novel PH-based morph detectors introduced to prevent morphing attacks on automatic border control (ABC) systems and support officers at border controls with an automatic morph detection algorithm. Extensive experimental investigations show that PH-based morph detectors provide a rich source of tamper-sensitive parameters that can be used for morphing detection.

4. Our investigation to detect morphed face images conducted on three datasets, two different digital datasets and one for P&S scenario. Classification results from the three datasets show high accuracy in detecting morphed faces in both digital and P&S scenario.

5. We designed a novel PH-based steganalysis technique to detect stego images where information been hidden through different steganographic methods. This approach is the first step towards building a universal PH-based steganalysis tool.

6. Another contribution of this thesis is in digital image inpainting field. Below we summarize the contributions accordingly:

    i. The conducted research argues that TDA is the next tool need to be used for image quality assessment in which it showcases the change occur in the image via inpainting process.

    ii. We improved exemplar based inpainting (EBI) by quantifying textures surrounding the missing region using TDA scheme.

7. Persistent Classification introduced as a new approach for tampered image classification which can be used as stopping criteria of building filtered simplicial complexes in TDA scheme. Although the original idea of persistent barcode is to construct topology at different scales from 0 to ∞. But

in practice, beyond certain scales constructed/extracted topological features do not contribute much into classification procedure.

1.5 Publications, Conference Talks and Awards

During the life of this thesis, a number of publications, conference talks and posters being produced as well as some awards being received which we list them accordingly.

1.5.1 Peer-Reviewed Publications

1- Aras Asaad and Sabah Jassim (2019).” Persistent Homology Detector of Face Image Morphing on Electronic ID”, journal of IEEE Transactions on Pattern Analysis and Machine Intelligence. (***Under Review***)

2- Sabah Jassim and Aras Asaad (2018). “*Automatic Detection of Image Morphing by Topology-based Analysis”* in 26th European Signal Processing Conference (EUSIPCO), doi: 10.23919/EUSIPCO.2018.8553317, IEEE, Rome, Italy.

3- Rasber D. Rashid, Aras Asaad, and Sabah Jassim. (2018). “*Topological data analysis as image steganalysis technique”* in Proc. SPIE 10668, Mobile Multimedia/Image Processing, Security, and Applications 2018, 106680J; doi: 10.1117/12.2309767; https://doi.org/10.1117/12.2309767, Florida, USA.

4- Ahmed K. Al-Jaberi, Aras Asaad, Sabah A. Jassim, and Naseer Al-Jawad (2018) “Topological data analysis to improve exemplar-based inpainting” in Proc. SPIE 10668, Mobile Multimedia/Image Processing, Security, and Applications 2018, 1066805; doi: 10.1117/12.2309931; https://doi.org/10.1117/12.2309931, Florida, USA.

5- Asaad A., Jassim S. (2017) “Topological Data Analysis for Image Tampering Detection”. In *Digital Forensics and Watermarking. IWDW 2017*. Lecture Notes in Computer Science, vol 10431. Springer, Cham, Magdeburg, Germany. https://doi.org/10.1007/978-3-319-64185-0_11

6- Aras T. Asaad, Rasber Dh. Rashid, and Sabah A. Jassim (2017) “Topological image texture analysis for quality assessment” in Proc. SPIE 10221, Mobile Multimedia/Image Processing, Security, and Applications 2017, 102210I (10

May 2017); doi: 10.1117/12.2268471; https://doi.org/10.1117/12.2268471, California, USA.

1.5.2 Conference Talks

1- Presented (Topology for Image Quality Assessment) in Mobile Multimedia/Image Processing, Security, and Applications conference (SPIE Commercial + Scientific Sensing and Imaging), 2017, Anaheim, California, USA.

2- Presented (Topological Data Analysis for Image Degradation Assessment) in EGL-2017 on 8-9th June, in University of Greenwich, London , UK.
https://www.gre.ac.uk/ach/research/events/recent-events/eglmathsworkshop .

3- Presented (TDA for Image Tampering Detection) in *Digital Forensics and Watermarking. IWDW 2017,August 23-25th,* in Magdeburg, Germany.
https://iwdw2017.cs.ovgu.de/cms/front_content.php .

4- Presented two papers (paper No. 3 and 4 in previous section) in Mobile Multimedia/Image Processing, Security, and Applications conference (SPIE Commercial + Scientific Sensing and Imaging) , Orlando, Florida, USA.

5- Presentation of (Breast cancer detection using Topological Analysis of digital Mammograms) in EGL 2018 Workshop on Optimisation, Applies and Numerical Mathematics, in University of Essex, UK, on 6th – 7th June 2018, https://www.essex.ac.uk/events/2018/06/06/egl-2018-workshop-on-optimisation,-applied-and-numerical-mathematics.

6- Presented (TDA-based Image Analysis) in London Mathematical Society (LMS) summer graduate student meeting in London, 29th June 2018, UK.
https://www.lms.ac.uk/civicrm/event/info?reset=1&id=30 .

7- Presented (Topology-based analysis for Image Tamper Detection and Related Applications) in Young researchers in Mathematics (YRM2018), 23rd July 2018, in Southampton University, UK. https://yrm2018.wordpress.com .

8- Presentation of (Topology-based analysis for Image Tamper Detection and Related Applications) in Dragon Applied Topology, 11-14th September 2018, Swansea, Wales, UK. https://sites.google.com/view/dragon-applied-topology .

9- Presented (Persistent Homology to Detect Fake Face Images) in London Mathematical Society (LMS) summer graduate student meeting in London, 28th June 2019, UK.

1.5.3 Awards

- **Best Paper Award** in Digital Forensics and Watermarking. IWDW 2017,August 23-25th, in Magdeburg, Germany for the paper "Topological Data Analysis for Image Tampering Detection", and a prize by Springer international publishing for the same paper.

- **Best Presentation/work Award** by London Mathematical Society for presentation (LMS) for the talk "Persistent Homology to Detect Fake Faces" in London Mathematical Society-Graduate Student Meeting, London, June 2019.

1.6 Thesis Outline

The rest of the thesis is organised as follows; Chapter 2 include a mathematical introduction into the concepts of Topological Data analysis used in the thesis. In Chapter 3, we introduce the building blocks of building topologies from digital images including image landmark selection methods. The first Homology-based algorithm to detect image tampering is introduced in chapter 4 whereby the type of tampering focused on is face image morphing. In Chapter 5, the homology-based morph detection algorithm in chapter 4 is improved together with extending the datasets and the image landmark selection methods. Beyond morphing, we present 3 case studies to show the effectiveness of our approach of using topological data analysis to tampering detection in chapter 6. The thesis ends in chapter 7 by reporting the conclusion and further research direction.

Chapter 2
Topological Data Analysis

Topological data analysis (TDA) is a new algorithmic paradigm in data analysis that evolved rapidly in recent years, but its theoretical and rigorous mathematical roots go back to the 17th century. TDA recently developed tools which have their roots in the field of *Algebraic Topology* when *Homology theory* was developed to exploit the computational simplicity provided by group theory and algebra for the computation of characterizing topological invariants of topological spaces in general and manifolds in particular. The range of TDA applications in Science, Technology, Engineering and Medicine (STEM) is growing fast but not as much as its potentials can facilitate perhaps due to its perceived complexity. The main goal of this chapter is to describe the well-founded topological terminology and processes for the analysis of large and complex datasets of records in terms of meaningful interpretations of the shape of data. While we attempt to maintain, as much as possible, a rigorous mathematical description of the various concepts and processes we shall attempt to make the chapter accessible to non-mathematicians as well as those early career topologists.

We first start by an introduction to basic concepts in Topology of shapes (section 2.1), to be followed by describing simplicial complexes modeling of topological manifolds (section 2.2) and the corresponding singular homology of the space. In section 2.3, we introduce the Vietoris-Rips simplicial complex and filtrations for the computation of the singular homology and the various algebraic topology invariants. The chapter ends by introducing the two main TDA tools which are *Persistent Homology* and *Mapper Algorithm*.

2.1 Introduction

Topology is the field of mathematics that is concerned with the study of geometric properties of objects/spaces in terms of the closeness and connectivity properties of its elements that are unaffected by continuous deformations. The fundamental idea

behind using topology for data analysis is that one can extract patterns from complex and high dimensional datasets and then obtaining deep insight about them.

A topological space consists of a non-empty set X, and a set of subsets of X, called open sets, which includes the empty set as well as X and is closed under sets union and finite sets intersection. Euclidean spaces are obvious examples of topological spaces with the open sets being the union of any number of open balls. Topological spaces are not limited to sets of numerical records, but the most interesting category of topological spaces, relevant to data analysis, is that of manifolds. An n-dimensional manifold M is a topological space for which every point $p \in M$ belongs to an open set U_p that is homoeomorphic to a unit open ball of the Euclidean space $\mathbb{R}^n$, satisfying certain properties. Here, U_p is a curved version of the unit ball in $\mathbb{R}^n$ and the imposed set of properties facilitate easy generalisation of Euclidean geometry parameters on M. These open sets form what is known as an *atlas* which together with the associated homeomorphisms act as coordinate charts to define the manifold by parametric equations. For more details on general topology and theory of manifolds the reader may consult a plethora of books and manuscripts (e.g. see [13][14][15][16]). The rest of this brief introduction will focus on the process of modelling data shapes by topological manifolds.

Low-dimensional manifolds are extensively studied and widely used to model many geometric objects/shapes often embedded in higher dimensional Euclidean spaces. Straight lines, close curves, trees, and graphs of wave functions are examples of 1–dimensional manifolds that are embedded in higher dimensional Euclidean/non-Euclidean spaces.
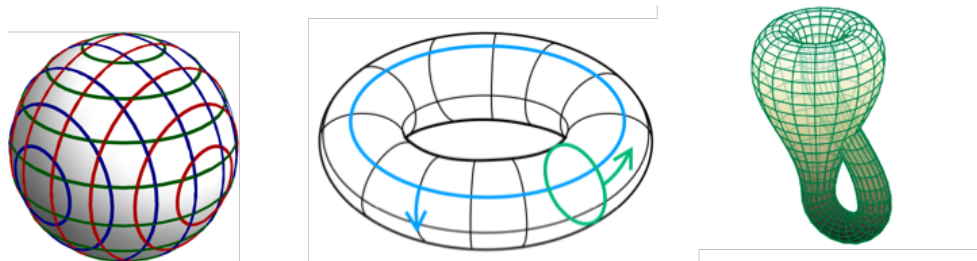
Figure 2-1: Surfaces of different manifolds. (Right)Sphere (Middle)Torus and (Left) Klein Bottle [17].

The surfaces of the Sphere, Torus, Klein bottle and most other Manifold models of intricate shapes can be constructed by a sequence of cutting, bending and gluing different subspaces of n-dimensional Euclidean space, where n is the perceived dimension of the modelled object. This process of forming manifolds by cutting, bending and gluing patches of subspaces of a Euclidean space $\mathbb{R}^n$, results in a tessellation/tiling of the constructed topological manifold with the sets of patch edges and faces forming a partition of the manifold formed by the patches and their common borders [18].
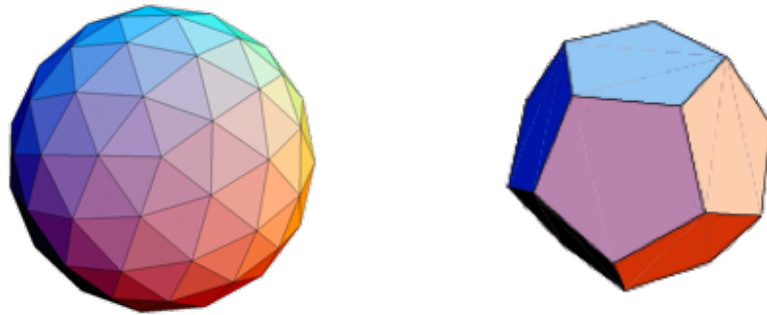
Figure 2-2: Two-dimensional manifold constructed using polygonal/triangular patches.

In the above examples, the 2-dimensional manifolds were constructed from using different patches of polygonal and triangular shapes. In this respect, Penrose kites and darts have been used intensively for defining tessellations of curved surfaces [18]. This well-established mathematically proven approach of using simple polygonal shapes to construct solid models of low dimensional manifolds, together with the emergence of sophisticated computer graphic tools has provided excellent opportunities to efficiently generate intriguing manifolds, including the following visualisation of 10-dimensional universe [19].
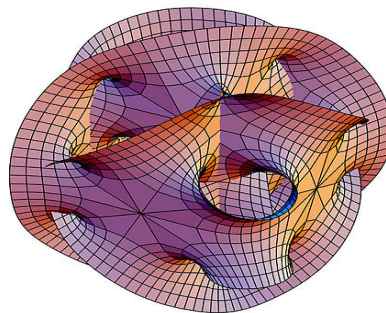
Figure 2-3: Calabi-Yau manifold projected into 3D which represent a universe of 10 dimension [19].

16

More interestingly, this approach has been adopted to model many known shapes, not only for their mathematical values but to address many modern challenging STEM applications including the complex folded shape of the human brain cortical surface [20]. Typically, the cortex surface geometric model is constructed by gluing a set of curved triangles covering the entire surface with no overlapping excepts at the boundaries, i.e. the triangular edges and vertices.

Applying the individual actions of manifold construction process in a slightly different order may result in topologically different manifolds. For example, the construction of a torus and a Klein-Bottle from a flat rectangular sheet only differ in the way the opposite borders of the rectangle are glued together.
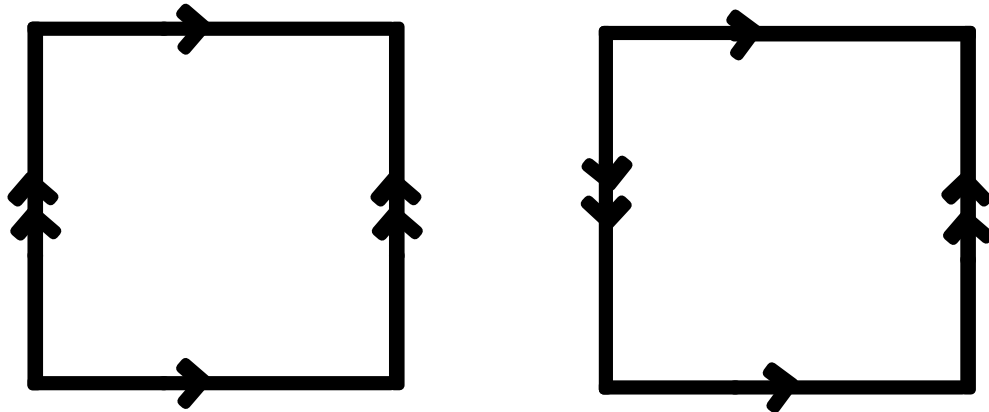
Figure 2-4:Illustration of a flat torus and a flat Klein bottle.

In the case of modelling the brain cortex, see figure (2-5), researchers confronted with the possibility of getting different topologies during the process of building the manifold and asked whether two such constructions are equivalent. Interestingly, to make sure a constructed topology is not a defect, they considered the use of known algebraic topology invariants such as the Euler Characteristic of the constructed map [20].
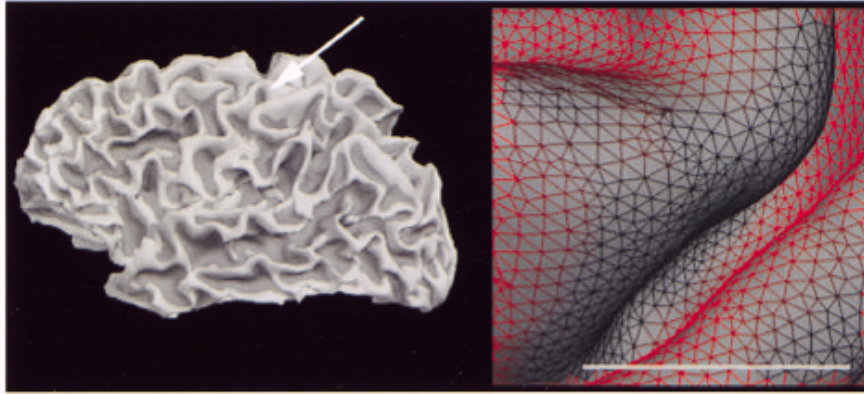
Figure 2-5: Topologically folded surface of brain and close-up tessellation of a small selected region (white arrow)[20].

What makes this approach to model the topology of shapes applicable to many applications is that the generated topological manifolds are known to be invariant under continuous deformation, its coordinate invariance, and provides compressed representation of the modelled shape [21]. Invariance under deformation means that the topological parameters of the modelled shapes do not change when squashing, stretching or deforming the shape geometrically without tearing/cutting, i.e. such operations generate homoeomorphic spaces. Figure (2-6)-left, illustrates different homoeomorphic versions of a circle. The coordinate invariance of topology refers to the fact that topological properties of the modelled shapes remain unchanged by rotation, translation and/or scaling (see figure (2-6)-middle). Employing these actions facilitates the compressed representation property. Figure (2-6)-right, illustrate this property whereby a smooth circle is represented by a Hexagon.

Far from being a diversion from the main theme of this thesis, the above rather brief discussion of the approach adopted for constructing and visualising manifold modelling of solid shapes provides a well-known and understood approach on how to model topological shapes of data. Also, how to use the wealth of knowledge acquired from the last century in the field of Algebraic topology as a source of computationally efficient data analysis tools.

| Continuous Deformation | Coordinate Invariance | Compressed Representation |
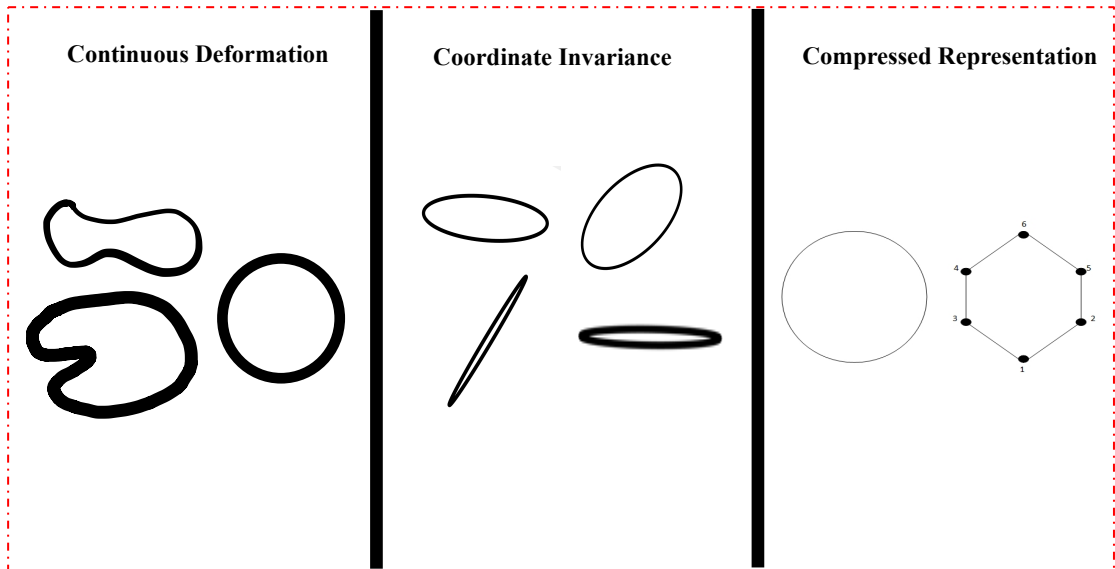
Figure 2-6: Topological properties of a circle.

However, we note that in the above examples one assumes a pretty good knowledge of expected topology. In the absence of advanced knowledge, a number of manifold learning algorithms have been developed over the years. Such algorithms often start by a data pre-processing step. One common pre-processing constructs a neighbourhood graph $\mathfrak{G}_t$, for each t, that connects each data point p to all data points within a radius of t. Another, manifold learning pre-processing scheme, constructs a graph $\mathcal{G}_k$ by connecting the k-nearest neighbours of each data point. Constructing these graphs, provide systematic approach to discover connectivity information and introducing Geodesic based metric space on the data shape. However, beyond connectivity these schemes do not reveal explicitly other topological properties of the learnt manifold. For that, one need to have reliable scheme of filling the regions bounding connected sets of edges with the interior of an appropriate polygonal shapes. A sensible filling scheme can be based on the assumption that the edges of any n-clique of the graphs are to be modelled as the bounding edges of a deformed n-simplex (n-dimensional triangle). This approach, adopted in this thesis, will model the shape of data records as a simplicial complex, and allows an efficient computation of the topological parameters of the data shape using known algebraic topology techniques. These concepts and procedures will be described and reviewed in the next three sections.

Selecting appropriate values for t (or k) for the above manifold learning schemes is considered as a challenge, however this challenge can be turned into a source of a deeper analysis by considering persistence of the topological invariants over a sequence of t values. This is the basis of the algebraic topology tool of Persistent Homology that will be employed in this thesis, and described in section 2.5.

2.2 Simplicial Complexes

A simplicial complex (SC) is a topological space constructed from a set of different-dimensional triangular subset of $\mathbb{R}^n$, by gluing together some of them along boundary components (nodes, edges, and faces). In general, SC have been used as an effective and easy to build topological shapes and modelling datasets of points in any metric space. A finite combinatorial process developed by topologists to efficiently compute the topological parameters of, and/or to visualize, a given manifold using a sample of its points. Topological data analysis deploys this process to construct SC models of point cloud data 'shapes'. SCs serve as a link between the continuous domain of topological spaces and the discrete space of data. Next, we give the formal definition of simplicial complex, together with the notion of 'simplex' and 'face' which are necessary to define SC.

Definition (simplicial Complex (SC)) [22]:

Consider $V = \{v_0, v_1, \dots, v_n\}$ to be the set of vertices. A SC with a vertex set V is a collection $\mathbb{S}$ of subsets of V whereby the following two conditions satisfied:

- The singleton $\{v\} \in \mathbb{S}$, where $v \in V$.
- Let $\tau \in \mathbb{S}$ and $\sigma \subset \tau$, then $\sigma \in \mathbb{S}$.

In words, τ is called a n-simplex which is basically the convex hull of $(n + 1)$ affinely independent points and σ is called a *face* of the simplex τ. Note that, this definition allows constructing simplexes from sets of not necessarily numerical data,

There is a binary relation between a simplex τ and its face σ which is known as pre-order, written as $\sigma \leqslant \tau$. We denote the set of d-dimensional simplices in $\mathbb{S}$ as $\mathbb{S}_d$, for $d \geq 0$. It is straightforward to see from the first condition of SC definition that the set of $\mathbb{S}_0$ correspond to the vertex set V in a one-to-one manner. In other words, one can interpret the building blocks of a SC as follows: a 0-simplex is a vertex (or point), 1-

simplex is a 1-dimensional edge (or line segment) between two vertices, 2-simplices are basically the 'filled' triangles formed by 1-simplices (edges) and a tetrahedron is a 3-simplex formed by 4 filled triangles. We name the low-dimensional simplices by their names, but in general an n-simplex is a n-dimensional subspace in $\mathbb{R}^n$. In figure (2-7) below, we illustrate graphically examples of simplices in different dimensions.
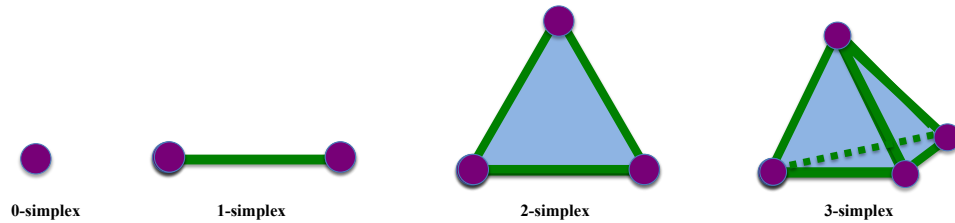
Figure 2-7: Simplices of different dimensions.

Note that, the above definition allows constructing simplicial complexes from sets of not necessarily numerical data. The example, below, illustrates the various concepts discussed above.

***Example* 1**: Consider the set of 0-dimensional simplices (i.e. vertex set) $V = \{a, b, c, d, e\}$ as depicted below.
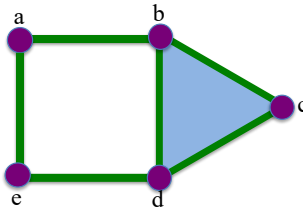
This SC is built iteratively dimension by dimension. The set of 0-dimensional simplices is:

$$\mathbb{S}_0 = \{\{a\}, \{b\}, \{c\}, \{d\}, \{e\}\}$$

Or simply

$$\mathbb{S}_0 = \{a, b, c, d, e\}.$$

$\mathbb{S}_1 = \{ab, bc, cd, db, de, ea\}$, is the set of 1-dimensional simplices. There is only one 2-dimensional simplex, namely the shaded triangle:

$$\mathbb{S}_2 = \{bcd\}.$$

21

No higher dimensional simplex is included in this example. One can easily realize that, fixing $\mathbb{S}_1$ immediately restricts which 2-dimensional simplex(s) can lie in $\mathbb{S}_2$. It is straightforward to see that $\mathbb{S}$ consists of one connected component and has one enclosed hole.

Two simplicial complexes, constructed with the same number of nodes, are topologically equivalent if they have the same topological invariant parameters. In general, these topological parameters enumerate the number of connected component, the number of 1-dimensional holes, i.e. closed sequence of edges that do not bound a 2-dimensional subspace, and number of 2-dimensional void cavity, i.e. a space with empty interior but bounded and enclosed by a number of 2-dimensional faces, and so on.

In the previous section we mentioned that we can construct the topology of point cloud data shape at different thresholds t, by constructing the neighbourhood graph G_t and then for each n-clique we can add an n-dimensional simplex. This approach is the basis of the following Vietoris-Rips construction. The following illustrate the resulting SCs for the same relatively small set of cloud point for a pair of different thresholds.
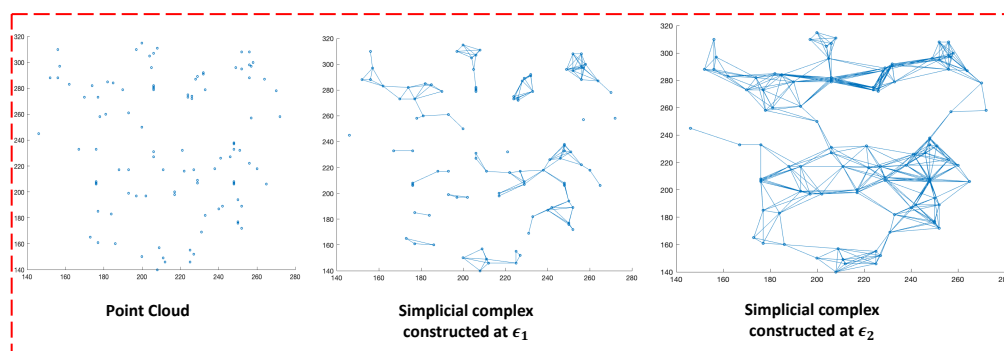
Figure 2-8: Different topologies constructed from the same point cloud set.

When two simplicial complexes are small, one can manually compute all the various topological parameters and not only check if they are topologically equivalent or not but also determine the pattern of changes in these values as t increased. But how to compute the number of connected components and holes of Rips SC of a point cloud consisting of hundreds or thousands of nodes? Manually, this task become daunting, so we need some smart tools. The smart machinery

needed for this purpose is none other than the long-established Algebraic topology tool of *homology*, to be explained in the next section. Next, we discuss the notion of homology and the necessary background to establish the computational tool used for determining the topological parameters of SCs. For more detailed mathematical introduction about simplicial complexes and homology theory, we encourage the interested reader to see [13], [14], [23][15].

2.3 Homology

Computing topological invariants of simplicial complexes is quite complex in topology. Homology is a major algebraic topology concept introduced by mathematicians to solve problems in topology by mapping them into problems in abelian groups which can be dealt with algebraically. Homology has evolved over decades as an algebraic tool for the classification of manifolds, that generalizes Euler characteristics invariant of polyhedrons and Riemann's definition of what is known as the genus of closed connected Riemann surfaces. It relies on the concept of homotopy that formulate the equivalence relation of continuous deformability of one submanifold to another of the same dimension. It has developed into an algebraic tool to classify/analyse manifolds in terms of the number of non-contractible (not continuously deformable to a single point) closed sub-manifolds. It is formally defined as a functor from the category of topological spaces and continuous functions into the category of Abelian groups (more precisely category of sequences of Abelian groups or Modules) and homomorphisms.

<u>Definition:</u> The homology functor H_* defined on the category of topological space and continuous functions into the category of finite abelian groups, associates with every topological space X and an integer $k \geq 0$, a finitely generated abelian group $H_k(X)$. And for each continuous function $f : X \to Y$ the functor associates a group homomorphism:

$$H_k(f) : \ H_k(X) \to H_k(Y) \tag{1}$$

satisfying some conditions on homomorphism composition including associative law, identity element and preserving the inverse.

The rank of $H_k(X)$ is an invariant of the topology of X, called the k-th Betti number of X.

23

Approximating topological spaces by simplicial complexes provides efficient computation of their homologies, known as Singular Homology. Note that representing shapes using the more general concept of cell complexes provide the alternative but equivalent concept of cellular homology. However, in the rest of this chapter we confine our discussion on computing singular homology of shapes of point cloud sets modelled by a simplicial complex. We shall now describe the process of determining the Homology functor of point cloud simplicial complexes and the process of computing its Betti numbers.

2.4 Simplicial Homology of a Point Cloud Simplicial Complex

Given a simplicial complex $\mathbb{S}$, homology associates an algebraic object, denoted as $H_k(\mathbb{S})$, called homology groups where $k \geq 0$ is the dimension of the simplices in $\mathbb{S}$. The rank of $H_k(\mathbb{S})$ is called the k-th betti number of $\mathbb{S}$. The k-simplices in $\mathbb{S}$ are generating vector spaces over Boolean field $\mathbb{Z}_2$ called k-th chain complex, denoted as $\mathcal{C}_k(\mathbb{S})$. Elements of $\mathcal{C}_k(\mathbb{S})$ are called k-chains (i.e. k-dimensional chain), which are linear combinations of k-simplices as follow:

$$\sum_{i=1}^{i=m} a_i \sigma_i$$

where $a \in \mathbb{Z}_2$ and σ is a simplex in $\mathbb{S}$. The operator that maps each k- simplex into its bounding chain is known as boundary operator, denoted as ∂_k. Consider a simplex $\sigma = [v_0, \ldots, v_k]$, then the boundary operator can be defined as follows:

$$\partial_k(\sigma) = \sum_{i=0}^{i=k} (-1)^i [v_o, v_1, \ldots, \widehat{v_i}, \ldots, v_k] \tag{2}$$

where the hat $'\widehat{}'$ symbol over v_i indicates that the vertex together with all sub-simplices of σ that intersects at v_i are removed. We are free to order vertices $v_0, \ldots, v_k$ as we like, and upon reordering one may get a minus sign depending on whether or not the new ordering of a given simplex is an odd or even permutation of the old one. For each integer $k \geq 0$, the boundary operator defines a linear transformation

$$\partial_k : \mathcal{C}_k(\mathbb{S}) \to \mathcal{C}_{k-1}(\mathbb{S})$$

which can be thought of as a matrix after ordering the simplices into a basis. Furthermore, one can establish the composition relation $\partial_k \circ \partial_{k+1} = 0$. As a consequence, a sequence of homeomorphism of abelian groups (i.e. chain complex) will be obtained as follow

$$\ldots \rightarrow \mathcal{C}_{k+1}(\mathbb{S}) \xrightarrow{\partial_{k+1}} \mathcal{C}_k(\mathbb{S}) \xrightarrow{\partial_k} \mathcal{C}_{k-1}(\mathbb{S}) \xrightarrow{\partial_{k-1}} \ldots \xrightarrow{\partial_2} \mathcal{C}_1(\mathbb{S}) \xrightarrow{\partial_1} \mathcal{C}_0(\mathbb{S}) \xrightarrow{\partial_0} 0.$$

Clearly, the image of ∂_{k+1} , written as $Im(\partial_{k+1})$, is a subspace of the kernel ∂_k (ker (∂_k)) and hence we define the k-th homology group of $\mathbb{S}$ by the quotient vector space:

$$H_k(\mathbb{S}) = \text{ker}(\partial_k) \, / \, Im(\partial_{k+1}) \tag{3}$$

Elements of $\text{ker}(\partial_k)$ and $Im(\partial_{k+1})$ are called cycles and boundaries, respectively [14]. In general, we are interested in computing the number of non-contractible cycles in different dimensions. Elements of $H_k(\mathbb{S})$ are cosets of image of ∂_{k+1}, called homology classes. When two cycles are representing the same homology-class, they are said to be *homologous*. This means that their difference is a boundary of the same simplex. The dimension of $H_k(\mathbb{S})$ is called the kth-Betti number, denoted as $B_k(\mathbb{S})$. Mathematically, it can be expressed as follow:

$$B_k(\mathbb{S}) := \dim\big(H_k(\mathbb{S})\big) = \dim\big(Ker(\partial_{k+1})\big) - \dim\big(Im(\partial_{k+1})\big)$$

Elements of $H_k(\mathbb{S})$, called homology classes, are formed by the cosets of the normal subgroup $Im(\partial_{k+1})$ in the group $\text{ker}(\partial_k)$. This means that two cycles (k-chains) are *homologous* (i.e. belong to the same homology-class) if their differences consist of k-simplexes that bound $(k+1)$-simplexes.

Depending on k , betti number are equivalent to the following:

$$B_0(\mathbb{S}) = \text{the number of connected components in } \mathbb{S}.$$

$$B_1(\mathbb{S}) = \text{the number of holes in } \mathbb{S}.$$

$$B_2(\mathbb{S}) = \text{the number of cavities in } \mathbb{S}.$$

Note that a hole is bounded by a cycle of more than 3 edges that contain no other vertex inside it, while a cavity is bounded by a polytope with more than 4 faces that

has an empty interior. In this thesis, we only use the $B_0(\mathbb{S})$ and $B_1(\mathbb{S})$ because the data we investigate is 2-dimensional greyscale images.

Example 2: Considering the simplicial complex in example 1, we give details on the terminologies and operations discussed in the previous section. In other words, we have the following sequence of subcomplexes after sorting their elements alphabetically:

$$\mathbb{S}_0 = \{a, b, c, d, e\}, \ \mathbb{S}_1 = \{ab, bc, cd, db, de, ea\}, \ \mathbb{S}_2 = \{bcd\} \ \ and$$

$$\mathbb{S} = \{a, b, c, d, e, ab, bc, cd, db, de, ea, bcd\}.$$

It is obvious to see that $\mathbb{S}_0$, $\mathbb{S}_1$ and $\mathbb{S}_2$ are all subsets of $\mathbb{S}$. First, we show how the boundary operator works on simplices in different dimensions. For notation convention, we denote a vertex , such as $\{a\}$, by $[a]$ and an edge $\{ab\} = [ab]$ and a triangle $\{abc\} = [abc]$. The boundary of 0-simplex is zero as follow:

$$\partial_0[a] = \partial_0[b] = \partial_0[c] = \partial_0[d] = \partial_0[e] = 0.$$

The boundary of 1-simplex can be stated as $\partial_1[ab] = b - a$, following the definition of boundary operator in equation (2). Similarly, the boundary of a 2-simplex is

$$\partial_2[bcd] = [cd] - [bd] + [bc].$$

Note that the negative sign before $[bd]$ is indicating the rotation (direction) of the simplex. If one ignores the rotation, then we can express $\partial_2[bcd]$ as follow

$$\partial_2[bcd] = [cd] - [bd] + [bc].$$

A k-chain is a linear combination of k-simplices. For instance, $[db] + [cd]$ is a 1-chain which is a linear combination of two 1-simplices. A k-cycle is a k-chain that has a boundary of zero. Consider the following 1-chains from figure (2-9):

$$(i) \ [ab] + [bc] + [cd] + [db]$$

$$(ii) \ [ab] + [bd] + [de] + [ea]$$

Now we want to check which of the above 1-chains represent a 1-cycle? To do so, take the boundary operator, as follow:

$$(i) \ \partial([ab] + [bc] + [cd] + [db]) = \partial([ab]) + \partial([bc]) + \partial([cd]) + \partial([db])$$

$$= b - a + c - b + d - c + b - d$$

$$= -a + b$$

$$\neq 0$$

Hence, the 1-chain we considered is not representing a 1-cycle.

(*ii*) $\partial([ab] + [bd] + [de] + [ea]) = b - a + d - b + e - d + a - e = 0$

Then the 1-chain in (ii) is representing a 1-cycle. Visually, the 1-chains in (i) and (ii) are depicted below.
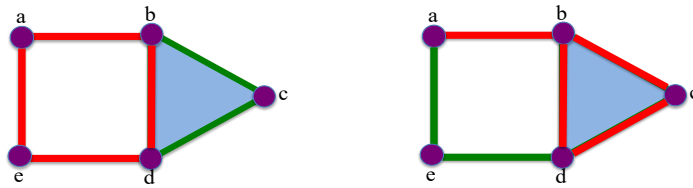
Figure 2-9: Pictorial representation of 1-chains. (Left) SC represent the 1-chain [ab]+[bd]+[de]+[ea] which is a 1-cycle whereas the (right) SC represent the 1-chain [ab]+[bc]+[cd]+[db] which is not representing a 1-cycle (loop).

When two cycles are homologous then they differ by a boundary. In other words, we want to avoid calculating the same cycle twice. For example, consider the following 1-chains:

$$\eta_1 = [ab] + [bd] + [de] + [ea]$$

$$\eta_2 = [ab] + [bc] + [cd] + [de] + [ea]$$

To check whether η_1 and η_2 are homologous? Take their difference:

$$\eta_1 - \eta_2 = [ab] + [bd] + [de] + [ea] - [ab] - [bc] - [cd] - [de] - [ea]$$

$$= [bd] - [bc] - [cd]$$

$$= [cd] - [bd] + [bc]$$

$$= \partial_2([bcd])$$

Since their difference is a boundary, which is $\partial_2([bcd])$, then η_1 and η_2 are homologous. In application, we only calculate distinct k-cycles. This calculation will

correspond to the number of connected component (i.e. $B_0(\mathbb{S})$) and the number of holes (i.e. $B_1(\mathbb{S})$) respectively. First, $\partial_0(\mathbb{S})$ is zero, and thus $\ker(\partial_0(\mathbb{S}))$ is the whole 0-chain which is

$$\mathrm{Ker}(\partial_0(\mathbb{S})) = \{\{a, b, c, d, e\}\}.$$

2.4.1 Smith Normal Forms to Compute Betti Numbers

Computing the Betti numbers of the previous, rather simple example of SC, illustrates the difficulty of manually determining the Betti numbers of a large point cloud simplicial complex. However, the work of Henry J. Smith in the mid 18th century, provides the simple matrix algebra based procedure to help solve this challenge efficiently, see [22]. In matrix algebra, the ***Smith normal form*** of any rectangular matrix A, with entries in a principle ideal domain (PID) such as the integers, is the diagonal matrix obtained from A by a sequence of row and column operations by invertible matrices over the given PID. It is very useful when dealing with finitely generated abelian groups as is the case for our homology groups. In what follows, we are closely following the methodology described in [22]–[25] to discuss the use of Smith form to calculate the betti numbers of a SC.

Definition (Smith Normal Form (SNF))[26]:

SNF of an $m \times n$ matrix $\mathcal{M}$ is the product $SNF(\mathcal{M}) = S\,\overline{\mathcal{M}}\,T$, where S and T are $m \times m$ and $n \times n$ invertible matrices, respectively. $\overline{\mathcal{M}}$ is an $m \times n$ matrix which has the following form:

$$\overline{\mathcal{M}} = \begin{bmatrix} l_1 & 0 & 0 & 0 & 0 \\ 0 & l_2 & 0 & 0 & 0 \\ \vdots & \vdots & \ddots & 0 & 0 \\ 0 & 0 & 0 & l_m & 0 \\ 0 & 0 & 0 & 0 & 0 \end{bmatrix}$$

such that each integer l_i is divisible by its successor l_{i+1}.

We shall now illustrate the process of using the Smith Normal form to compute the Betti numbers of point cloud SCs, using the example of the simplicial complex in example 1.

Since $\partial_1(\mathbb{S})$ is the map $\partial_1 \colon C_1(\mathbb{S}) \to C_0(\mathbb{S})$ and we can express ∂_1 in the form of a matrix in the chosen basis vector in $\mathbb{Z}$. Let bcd denote the basis vector for the simplex $\{bcd\}$. Similarly, use ab, bc, cd, db, de, ea to denote basis vectors that correspond to the 1-simplices and a, b, c, d, e be the basis vectors for 0-simplices. We then have the following matrices:

$$
\partial_2 = \begin{array}{c} \\ ab \\ bc \\ cd \\ bd \\ de \\ ea \end{array}
\overset{\displaystyle bcd}{\begin{bmatrix} 0 \\ 1 \\ 1 \\ -1 \\ 0 \\ 0 \end{bmatrix}}
$$

$$
\partial_1 = \begin{array}{c} \\ a \\ b \\ c \\ d \\ e \end{array}
\overset{\displaystyle ab \quad bc \quad cd \quad db \quad de \quad ea}{\begin{bmatrix} -1 & 0 & 0 & 0 & 0 & 1 \\ 1 & -1 & 0 & 1 & 0 & 0 \\ 0 & 1 & -1 & 0 & 0 & 0 \\ 0 & 0 & 1 & -1 & -1 & 0 \\ 0 & 0 & 0 & 0 & 1 & -1 \end{bmatrix}}
$$

Applying standard row and column operations, one can reduce above matrices to *smith normal form* (SNF), such that the diagonal entries are all either zero or one and the off-diagonal elements are all zero.

Applying the above definition of SNF on ∂_1 and ∂_2, we obtain the following:

$$
SNF(\partial_2) = \begin{bmatrix} 1 \\ 0 \\ 0 \\ 0 \\ 0 \\ 0 \end{bmatrix} \quad and \quad
SNF(\partial_1) = \begin{bmatrix} 1 & 0 & 0 & 0 & 0 & 0 \\ 0 & 1 & 0 & 0 & 0 & 0 \\ 0 & 0 & 1 & 0 & 0 & 0 \\ 0 & 0 & 0 & 1 & 0 & 0 \\ 0 & 0 & 0 & 0 & 0 & 0 \end{bmatrix}
$$

Then once the SNF matrix computed, the Betti numbers can be calculated as follow[25]:

$$
B_k = \sigma_k - \lambda_k - \lambda_{k+1} \tag{4}
$$

where σ_k is the k-simplices, λ_k and λ_{k+1} is the number of non-zero diagonal entries in SNF of ∂_k and ∂_{k+1}, respectively.

Hence, $B_0(\mathbb{S}) = 5 - 4 - 0 = 1$ and $B_1(\mathbb{S}) = 5 - 4 - 0 = 1$, which is the case for the simplicial complex in example 1.

Example 3: Consider the point cloud given in figure (2-10) below, which consist of 10 points.
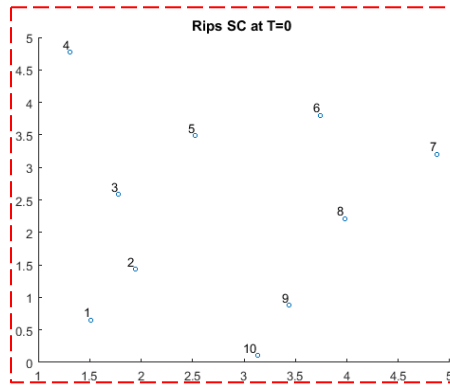
Figure 2-10:A sample of points in Euclidean Space.

Firstly, at $t = 0$, the points are 0-simplices by themselves. Then $\partial_0 = \partial_1 = 0$, since there is no edges and B_0 =No. of 0-simplices =10. Increase the distance threshold and compute SNF for the boundary matrices of different dimensions.
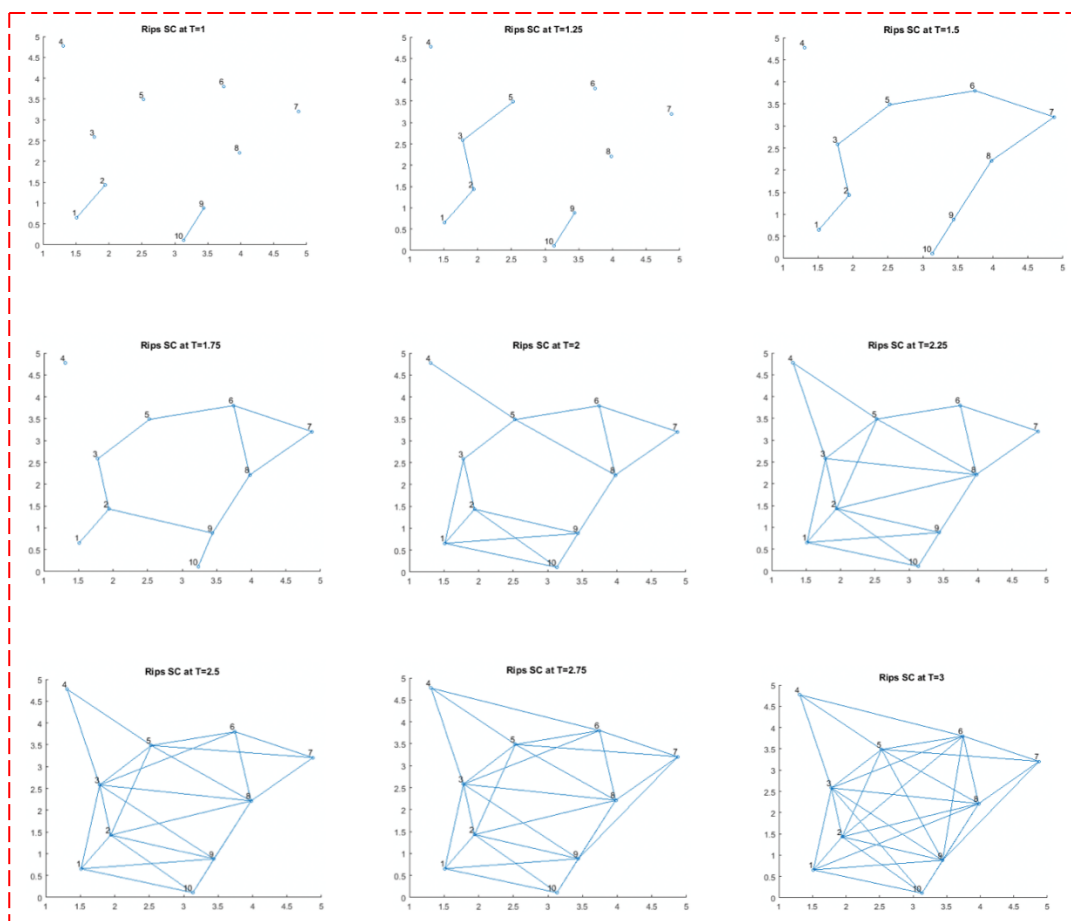
Figure 2-11: A sequence of Rips SCs build over an increasing sequence of distance thresholds.

For each of the (Rips) simplicial complexes constructed in figure (2-11),

$$\partial_1(\mathbb{S}_{t=1}) = \begin{bmatrix} -1 & 0 \\ 1 & 0 \\ 0 & 0 \\ 0 & 0 \\ 0 & 0 \\ 0 & 0 \\ 0 & 0 \\ 0 & 0 \\ 0 & -1 \\ 0 & 1 \end{bmatrix} \quad \text{and its corresponding} \quad SNF(\partial_1\mathbb{S}_{t=1}) = \begin{bmatrix} 1 & 0 \\ 0 & 1 \\ 0 & 0 \\ 0 & 0 \\ 0 & 0 \\ 0 & 0 \\ 0 & 0 \\ 0 & 0 \\ 0 & 0 \\ 0 & 0 \end{bmatrix}$$

$$\partial_1(\mathbb{S}_{t=1.25}) = \begin{bmatrix} -1 & 0 & 0 & 0 \\ 1 & 0 & -1 & 0 \\ 0 & 0 & 1 & -1 \\ 0 & 0 & 0 & 0 \\ 0 & 0 & 0 & 1 \\ 0 & 0 & 0 & 0 \\ 0 & 0 & 0 & 0 \\ 0 & 0 & 0 & 0 \\ 0 & -1 & 0 & 0 \\ 0 & 1 & 0 & 0 \end{bmatrix} \Rightarrow SNF(\partial_1(\mathbb{S}_{t=1.25})) = \begin{bmatrix} 1 & 0 & 0 & 0 \\ 0 & 1 & 0 & 0 \\ 0 & 0 & 1 & 0 \\ 0 & 0 & 0 & 1 \\ 0 & 0 & 0 & 0 \\ 0 & 0 & 0 & 0 \\ 0 & 0 & 0 & 0 \\ 0 & 0 & 0 & 0 \\ 0 & 0 & 0 & 0 \\ 0 & 0 & 0 & 0 \end{bmatrix}$$

Similarly, the SNF at $t = 1.5$, and $t = 1.75$ are as follows:

$$SNF(\partial_1(\mathbb{S}_{t=1.5})) = \begin{bmatrix} 1 & 0 & 0 & 0 & 0 & 0 & 0 & 0 \\ 0 & 1 & 0 & 0 & 0 & 0 & 0 & 0 \\ 0 & 0 & 1 & 0 & 0 & 0 & 0 & 0 \\ 0 & 0 & 0 & 1 & 0 & 0 & 0 & 0 \\ 0 & 0 & 0 & 0 & 1 & 0 & 0 & 0 \\ 0 & 0 & 0 & 0 & 0 & 1 & 0 & 0 \\ 0 & 0 & 0 & 0 & 0 & 0 & 1 & 0 \\ 0 & 0 & 0 & 0 & 0 & 0 & 0 & 1 \\ 0 & 0 & 0 & 0 & 0 & 0 & 0 & 0 \\ 0 & 0 & 0 & 0 & 0 & 0 & 0 & 0 \end{bmatrix}$$

$$SNF(\partial_1(\mathbb{S}_{t=1.75})) = \begin{bmatrix} 1 & 0 & 0 & 0 & 0 & 0 & 0 & 0 & 0 & 0 \\ 0 & 1 & 0 & 0 & 0 & 0 & 0 & 0 & 0 & 0 \\ 0 & 0 & 1 & 0 & 0 & 0 & 0 & 0 & 0 & 0 \\ 0 & 0 & 0 & 1 & 0 & 0 & 0 & 0 & 0 & 0 \\ 0 & 0 & 0 & 0 & 1 & 0 & 0 & 0 & 0 & 0 \\ 0 & 0 & 0 & 0 & 0 & 1 & 0 & 0 & 0 & 0 \\ 0 & 0 & 0 & 0 & 0 & 0 & 1 & 0 & 0 & 0 \\ 0 & 0 & 0 & 0 & 0 & 0 & 0 & 1 & 0 & 0 \\ 0 & 0 & 0 & 0 & 0 & 0 & 0 & 0 & 0 & 0 \\ 0 & 0 & 0 & 0 & 0 & 0 & 0 & 0 & 0 & 0 \end{bmatrix}$$

$$SNF\left(\partial_2\left(\mathbb{S}_{t=1.75}\right)\right) = \begin{bmatrix} 1 \\ 0 \\ 0 \\ 0 \\ 0 \\ 0 \\ 0 \\ 0 \\ 0 \end{bmatrix}$$

The process is the same for the rest of SCs in figure (2-11). Following the formula in equation (4), one can calculate the Betti numbers as follow:

$$(B_0)_{t=1} = \sigma_0 - \lambda_0 - \lambda_1 = 10 - 0 - 2 = 8.$$

$$(B_0)_{t=1.25} = \sigma_0 - \lambda_0 - \lambda_1 = 10 - 0 - 4 = 6.$$

$$(B_0)_{t=1.5} = \sigma_0 - \lambda_0 - \lambda_1 = 10 - 0 - 8 = 2.$$

$$(B_0)_{t=1.75} = \sigma_0 - \lambda_0 - \lambda_1 = 10 - 0 - 8 = 2.$$

A 1-dimensional hole start building up at $t = 1.75$, and using the formula in equation (4) we can calculate 1-dimensional betti numbers as follow:

$$(B_1)_{t=1.75} = \sigma_1 - \lambda_1 - \lambda_2 = 10 - 8 - 1 = 1.$$

2.4.2 Persistent Homology and Filtration

Considering the original challenge of determining the shape of point cloud set, the so far described process of determining the topological parameters of a simplicial complex is applicable to the manifold learning of the dataset at each and every threshold t. By allowing t to vary, over a period, we get a nested sequence of simplicial sub-complexes of the SC obtained with last threshold. This yields a time series, parameterized by t, of Betti numbers associated with the point cloud dataset over the chosen period. Topological data analysis is based on analysing these time series in terms of patterns of changes in the k-dimensional Betti numbers such as persistent patterns.

In TDA, Persistent Homology (PH) of a simplicial complex $\mathbb{S}$ is formally defined in terms of a recursive filtration of $\mathbb{S}$ by a nested sequence of sub-complexes. For efficient computation of PH for point clouds, we shall use an iterative method to

obtain a nested sequence of simplicial complexes of a point cloud within a chosen threshold range. The PH of a point cloud is the observed pattern of persistence of various Betti numbers computed over the life span of the investigated threshold range, called filtration procedure. A trace of the persistence of each generating element of H_k ($\mathbb{S}_t$) over a sequence of t values can be represented by a half-open interval $[a, b)$, where a represent its birth and b its death.

Let $\mathbb{S}$ be a finite (Rips) simplicial complex and $\mathcal{S}_1 \subset \mathcal{S}_2 \subset \cdots \mathcal{S}_l = \mathbb{S}$ be a sequence of nested sub-complexes of $\mathbb{S}$. Then $\mathbb{S}$ is called *filtered simplicial complex* together with such a sequence of sub-complexes. Figure (2-11) is an example of a filtered simplicial complex. Experimental data can take many forms such as digital image, text, voice signal, video and tables of categorical data. The data in this thesis is mainly 2-dimensional digital images in which we analyse for the purpose of tamper detection. More specifically, we extract a point cloud $P \in \mathbb{R}^2$, a finite collection of image landmarks automatically extracted from images, using image texture descriptors discussed in next chapter. As a first step towards building filtered Rips complexes, compute the Euclidean distance between all pairs of 0-simplicies and then select an increasing sequence of Euclidean distance threshold and build the filtration. At each filtration step, we apply homology to the sub-complexes constructed, as follow:

$$H_k\big(\mathbb{S}_{t_1}\big) \xrightarrow{f_k^{t_1 \to t_2}} H_k\big(\mathbb{S}_{t_2}\big) \xrightarrow{f_k^{t_2 \to t_3}} \ldots \xrightarrow{f_k^{t(n-1) \to tn}} H_k\big(\mathbb{S}_{t_n}\big) \qquad (5)$$

where $t_1 < t_2 < \cdots < t_n$, $k = \{0,1\}$, $f : H_k(\mathbb{S}_{t_{n-1}}) \to H_k(\mathbb{S}_{t_n})$ is a linear simplicial map of homology groups induced by an inclusion chain map $\mathcal{C}_k(\mathbb{S}_t) \to \mathcal{C}_k(\mathbb{S}_{t+1})$, i.e. the chain map is induced by inclusion of simplices from each stage to the next. The structure in equation (5) is called a persistent module. If $k = 0$, then we are computing the number of connected components at each filtration step whereas for $k = 1$, we are computing the number of 1-dimensional holes (i.e. loops). For $k = 2$, computed homological parameter correspond to the number of cavities.

Definition (Persistent Homology) [27]:

Let $\mathbb{S}_{t_1} \subset \mathbb{S}_{t_2} \subset \cdots \subset \mathbb{S}_{t_n} = \mathbb{S}$ be a filtered simplicial complex. The k-th persistent homology of $\mathbb{S}$ is the pair

$$\left(\{H_k(\mathbb{S}_t)\}_{1 \le i \le n} , \{f_{i,j}\}_{1 \le i \le j \le n} \right) \tag{6}$$

for $i, j \in \{1, 2, \ldots, n\}$, $i \le j$, the linear maps $f_{i,j} \colon H_k(\mathbb{S}_{t_i}) \to H_k(\mathbb{S}_{t_j})$ are the maps induced by the inclusion maps $\mathbb{S}_{t_i} \hookrightarrow \mathbb{S}_{t_j}$.

In other words, instead of computing the homology of a single sub-complex, k-th persistent homology of a filtered simplicial complex provides a more refined information about the intermediate homological information.

Persistent homology calculation is similar to homology calculation, representing the boundary operators by a matrix and then reducing it to SNF, except that the operations performed over polynomials in one variable with coefficients in $\mathbb{R}$. There are many efficient software developed for the purpose of persistent homology calculation such as Perseus [28], Ripser [29], JavaPlex [30], DIPHA[31] , DIONYSUS [32], GHUDI [33], J-Holes [34] and others. For a comprehensive review of PH software's, interested reader is advised to see [27]. We opt to use Ripser (written in C++) as it is the best-performing library for the computation of PH of Rips complexes currently.

PH stores homological information about the underlying topological space in a form of half-open interval $[a, b)$, where a represent the birth of a homology group generator and b is the point where it vanishes. The collection of such intervals is called *persistent barcodes*. The important key observation about persistent barcodes is that they are stable under perturbations in the filtration [35]. In other words, assume two data points such as D and D', where D' is a noisy version of D obtained by perturbing each point in D with some distance $\epsilon > 0$. Then the bottleneck distance between k-dimensional persistent barcodes of D and D' is smaller than ϵ for every k. Mathematically, this can be formulated as follow. Let $X = PB_D$, $Y = PB_{D'}$ be the persistent barcodes of D and D' respectively and $\|\cdot\|_\infty$ is ∞-norm. Then the bottleneck distance between X and Y is:

$$d_\infty(X, Y) = \inf_{\eta : D \to D'} \sup_{x \in X} \|PB_D - \gamma(PB_{D'})\|_\infty \tag{7}$$

such that η ranging over all bijections. Then the stability theorem ,[35], states that when X and Y perturbed with ϵ, then $d_\infty(X, Y) \le \epsilon$.

An equivalent representation of the PH is the so-called persistent diagram which depicts generator's (birth, death) pairs as points in first quadrant of $\mathbb{R}^2$ above its diagonal. We refer the reader to [27] [1], [36]–[38] for a detailed introduction to PH and efficient algorithms for its computation. In *figure (2-12)-left*, we show an example of persistent barcodes when $k = 0,1$ for the simplicial complex given in **example 3**. *Persistent diagrams* see figure (2-12)-right, which provide similar information graphically except that a half open interval $[a, b)$ is represented by a point such as (a, b) in $\mathring{\mathbb{R}}^2$, where $\mathring{\mathbb{R}} = \mathbb{R} \cup \{\infty\}$. In other words, a persistent diagram is a graphical representation of persistent barcodes in a form of finite multiset of points in $\mathring{\mathbb{R}}^2$ which conveys exactly the same topological information except that x-axis depicts the birth of a homology group and y-axis is where it vanishes (merges with other homology groups).
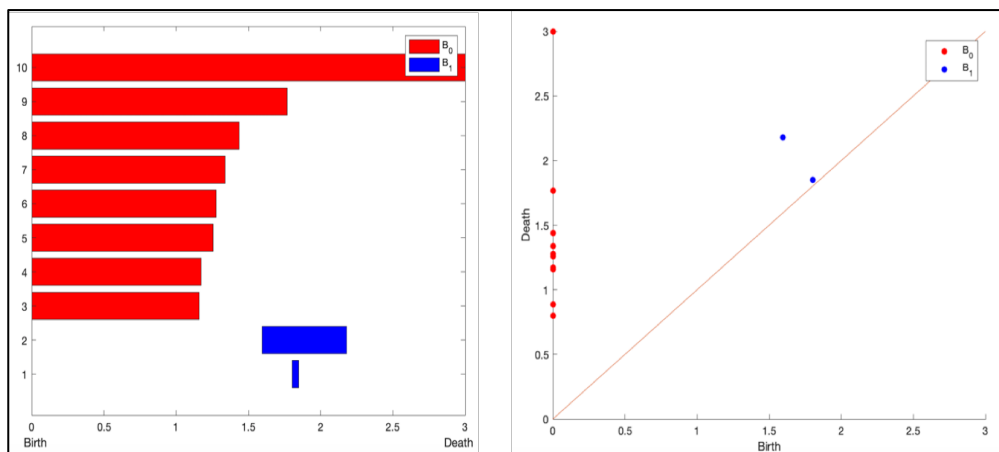
Figure 2-12: Topological Persistent visualization. (Left) Persistent Barcode (Right) Persistent Diagram.

Topological features can be quantified by their persistence in the filtration process. Persistent barcodes clearly depict that some of the topological features, in all dimensions, 'live' longer than others in the constructed Rips complexes while others 'die' quickly as one increases the distance threshold. In other words, long-lived bars directly related to large/dominant topological features in data whereas short-lived bars are sometimes neglected or regarded as noise. Hence, PH provides a novel approach of structure-related feature extraction and representation from data and found itself to be a suitable tool in many areas such as computational biology[39], quality

assessment of dimensionality reduction techniques [40], structure of sensor-network coverages [41], protein compressibility and binding [30,31], single-cell development [44], medical imaging [45], gait recognition [46]–[49], neuroscience [50]–[54] and many more. For a survey of recent applications of PH in various applications, we refer the interested reader to [27] , [54], [55].

Extracting topological features from persistent barcodes can have many forms. The simplest is extracting statistical properties of bars such as sum, average, variance, short and long bars. In this vein, Khasawneh and Munch [57][58] used long-persisting bars to investigate the stability of stochastic turning models. Giansiracusa et. al [59] used average, median and standard deviation of persistent barcodes as a feature for finger print classification. In [60], Can et al. used length (in dimension zero, one and two), average and onset value of bars for the purpose of protein classification by feeding these features into support vector machine (SVM) classifier. Sara Kalisnik in [61] proposed to coordinatize the space of persistent barcodes in terms of Tropical coordinates and showed that they are stable with respect to bottleneck distances. Recently, in February 2018, Zielinski et al [62] proposed a technique to discretize the space of persistent diagrams called *persistent codebooks*. The main idea behind persistent codebooks is to quantize the space of persistent diagrams using bag-of-features(words), vectors of locally aggregated descriptors (VLAD) and Fischer vectors (FV). In other words, they use k-means clustering to represent the space of persistent diagram as a fixed size vector which is suitable to machine learning, and they also show the stability of their approach with respect to 1-Wasserstein distance.

Albeit reported success in extracting the statistics from the persistent barcodes, previous approaches are only using partial information provided by persistent barcodes/diagrams. In chapter 4, we introduce a more systematic approach to discretize the space of persistent barcodes, called '**persistence binning'** and show its effectiveness for various image tampering detection tasks.

Another direction of generating features from persistent barcodes is the idea of building persistent functions such as persistent landscapes [63], persistent images [64] and persistent paths and signatures [65]. Persistent landscape approach maps the persistent barcodes into Banach and Hilbert space whereby the mapping is stable and

invertible. Persistent images (surfaces), on the other hand, represent the persistent diagrams as integrable function $f: \mathbb{R}^2 \to \mathbb{R}$ using a weighted sum of gaussian functions (i.e. probability density functions) centered at each point in persistent diagrams and hence obtaining a matrix/image through calculating the integral of each grid box. Finally, persistent paths and signatures, proposed by Chevyrev et al. in [65], is another approach that works by first embedding the persistent barcode information into a persistent path using persistent landscapes, and then building a feature vector using tensor algebra.

Next, we briefly introduce the concept of Mapper Algorithm as it will be used to visualize and support our understanding of topological and geometrical features extracted from digital images.

2.4.3 Mapper Tool

Visualizing shapes of high dimensional point clouds in informative formats, though useful, is almost impossible even with the use of advanced dimension reduction schemes. The TDA approach to deal with such point cloud datasets, as described in the previous sections using simplicial complex filtration and persistent homology tools, small distances (or high similarity weights) have more impact on the analysis of the data records. Consequently, a combination of clustering, appropriate filtering and existing visualization tools that model similarity levels such as the multi-dimensional scaling (MDS) can provide a useful tool. Mapper is one such tool developed by Singh et al. in [66].

Given a high dimensional point cloud $\mathcal{X}$, Mapper constructs an approximate topological representation of $\mathcal{X}$ through a simplicial complex and the output can be visualized in a 3D (or 2D) Euclidean space for further investigation and analysis. Roughly speaking, Mapper takes an input data and starts by first splitting it into many overlapping intervals (also called bins) using appropriate filters, also known as lenses, and then clustering the data within each interval. The result of each interval-based clustering will be represented by a set of node(s) and edges will be constructed when there is at least one intersection point/member between the nodes/clusters. Constructed simplicial complex conveys the main topological features of the data in the sense that mapper groups similar points into a cluster, then clusters are connected, and one obtains connected components, loops and flares. In what follows, we

describe Mapper steps more concretely where we follow closely Belchi et al. in [67] to describe details of Mapper.

Consider a metric space $(\mathcal{X}, d)$ where $\mathcal{X}$ is the point cloud and d is a metric on $\mathcal{X}$. Let

$$C = \{C_i\}_{i=1}^{n}$$

be a cover of $\mathcal{X}$ such that

$$\mathcal{X} = \cup_{i=1}^{n}(C_i).$$

The set of C_i are called bins and are obtained by (1) the following real-valued function

$$f: \mathcal{X} \rightarrow \mathbb{R}$$

which is known as a lens or filter-function, (2) fixing overlapping intervals to cover $f(\mathcal{X})$ such as I_i and

$$C_i := f^{-1}(I_i).$$

In this thesis, we consider a discrete and finite sample such as X drawn from $\mathcal{X}$. Clustering each bin will result in obtaining

$$C_i = V_1^i \cup V_2^i \cup ... \cup V_l^i$$

where V_l is the number of vertices in each bin. The Mapper output is a simplicial complex in which n-simplex are represented by $(n + 1)$-tuple of clusters as follows:

$$\sigma = \left(V_{j_1}^{i_1}, ..., V_{j_{n+1}}^{i_{n+1}} \right)$$

with a nonempty intersection. Figure (2-13) depicts an example of Mapper algorithm applied to a point cloud.

It is worth noting that, there is no restriction on the type of clustering techniques one might choose, or the type of filter functions applied to obtain the compressed topological representation of the data by Mapper. Different filter functions and clustering techniques result in a different topological shape which allows the user to

analysis and explore the data from different perspectives [21]. Nonetheless, some filter functions and clustering techniques may not produce any interesting topological
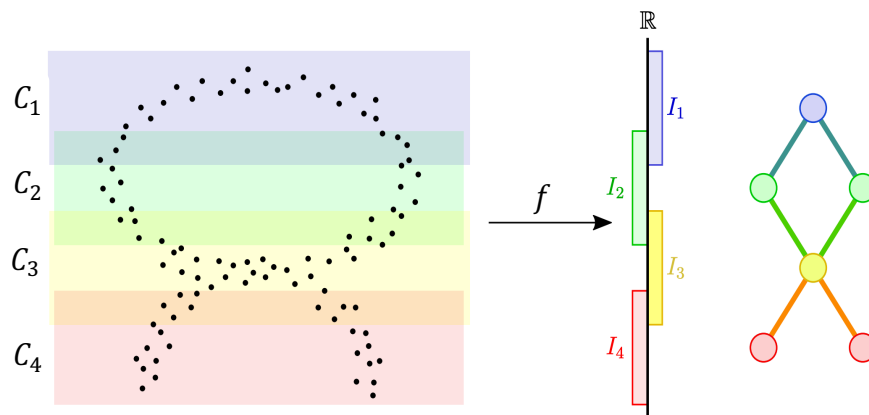
Figure 2-13: Illustration of Mapper Algorithm pipeline [67]. Mapper algorithm produces a simplicial complex (right) by clustering each interval of the data points (left) where it depicts a hole and two flares which is a simplified topological version of the data pints on the right.

object such as a straight line. Therefore, one needs to experimentally figure out the topological shape of interest, through different filter functions and clustering techniques, in which it allows the identification of flares or clusters of interest.

Mapper has been applied successfully in many applications in a variety of disciplines such as breakthrough results in identifying a subgroup of breast cancer patients with a unique mutational profile and excellent survival [68]. Other medical application include; cancer analysis [69][70], asthma [71][72][73], spinal cord injury [74], genomics[39][75][76] and diabetes[77][78]. Other applications include: chemistry [79][80][81], agriculture [82] and many more [21] [83][84][11]. Finally, we direct the reader to [67] and [85] for detailed discussions about the instability of Mapper-type algorithms. There is a couple of publicly available software for mapper computation and a commercial one by Ayasdi, a company which is based on Mapper algorithm. Kepler Mapper and python mapper are publicly available software which enable users to implement Mapper on their data, both written in python language. In this thesis, we use Kepler-Mapper in scikit-tda using Jupyter notebook platform.

In summary, the mathematical framework necessary for building simplicial complexes and computing persistent homological invariants introduced, and it will be used in the rest of this thesis. Also, the concept of Mapper algorithm has been discussed which will be used in some of our analysis in the next chapters. Next

chapter will contain morphing problem statement and different types of face morphing creation. This is together with the motivation behind using TDA to design morph detection tools. In addition, the threats of face morphing into face biometrics and beyond will be illustrated in detail.

Chapter 3
Topological Image Analysis

Over the last few years, since undertaking this research project, the use of TDA for image analysis and computer vision applications have grown steadily. Undoubtedly, this growth greatly benefitted from the emergence of computationally efficient tools for computing PH and Mapper. In each of the so far developed TDA schemes, the Persistent Homology of a specific application-relevant image feature parameter is selected and used to compute the topological signature. However, it is somewhat difficult to identify a clear strategy for selecting TDA-sensitive image features when considering a wider range of image analysis tasks without prior knowledge. This chapter is devoted to developing a strategy for automatic selection of image features whose spatial distribution is appropriate for designing topological signatures in a wide range of different applications. We present argument in support of complementing traditional image analysis with a special TDA strategy to construct topologies with a variety of image feature subsets and analyse their persistence parameters. We shall demonstrate the viability of this strategy in dealing with some easy to describe tasks.

3.1 Introduction

Image/video processing/analysis applications and algorithms deal with a growing list of challenges in different areas of modern technology including Computer vision, pattern recognition, biometrics-based identifications, biomedical image classifications/diagnostics, etc. Regardless of the source/domain of the relevant image datasets, to be analysed, a digital image is a rectangular matrix whose entries are elements of Z_n^r, where r is fixed to be 1 or 3 depending on the number of colour channels used and $n = 2^k$ where k is the intensity resolution of the images. This description is often referred to as the image spatial domain but is also applicable to other image domains such as the frequency/transformed domains (obtained by discrete Fourier or wavelet transforms). The rest of the thesis is only concerned with

spatial domain images, but many results are susceptible to be generalised to other image domains.

Generally, the term image analysis aims to discover patterns/patches of intensity values (or parameters defined in terms of these values) that convey some meaning/information about image content useful for identifying visually distinguished objects or could be used to group images into separate classes. Discovering application-relevant patterns of pixels, referred to as image features, mostly involve extensive and advanced searching and mining techniques. Over the years a variety of models for pattern discovery and classification have been developed in many different types of image-based applications. In most applications, patterns of interest relate to image patches where there are measurable variations in its pixel values, i.e. where some form of texture are detectable. Image regions that involve little or no pixel value variations indicate smoothness and absence of texture, but nevertheless such patterns could also provide information useful for discriminating different classes of images. Image segmentation is a common example of analysis tasks that aims to detect regions of interest (ROI) relevant to some applications and relies on detecting variation in the distribution of pixel values (singularly or within local neighbourhood) between inside and outside ROI. In many image analysis applications, image segmentation is used as a pre-processing task. Face recognition is another typical application that relies on analysing face digital images in search of patterns of features that discriminate face images of different persons. In digital forensics and multimedia security applications, tamper detection relies on extracting tiny changes to certain groups of image features that result in violating some known statistical properties of these features. Furthermore, texture-base image analysis is recognised as an essential tool in the fast-growing research area of using Artificial Intelligence in medical diagnoses of disease-related abnormalities in a variety of tissues/organs [9].

Regardless of the complexity/modality of the image datasets, analysis tasks rely on some means of measuring similarity/distances between pairs of extracted feature records that are meant to discover hidden informative patterns of similarity/dissimilarity. Focusing on pairwise relations/similarities was one of the fundamental building blocks of mining bigdata that have been extensively investigated in the past. Discovered image patterns/patches, are often aggregated into

feature records, to be subjected to some distance-based and/or statistical distribution-based analysis. In the former case, extracted feature records in many applications are modelled as vectors in Euclidean spaces and linked discovery of hidden data patterns to clustering the data in terms of linear distance functions. However, and as discussed in chapter 2, these linear models were found to have many shortcomings and Manifold learning algorithms where developed to have a more realistic understanding of shape of data. Indeed, one can observe that the emergence of TDA naturally complements the objectives of Manifold learning and clustering approaches to data/image analysis, by providing efficient algebraic topology tools not only to extract topological parameters of data shapes but to discover patterns in terms of persistence of these parameters at scales.

In traditional image analysis, no consideration is given to the spatial distributions of the discovered patterns/features within the individual images. The main incentive for this thesis is that in many applications the spatial distribution of relevant image patterns provide the main ingredients for adopting TDA. At the outset of this research project, the use of TDA for image analysis applications were not clearly distinguished from analysis of other types of complex or high-dimensional data. Interestingly, the inspiring work of Mumford et al. [8] and Carlson et al. [86], that established a mapping of the space of normalised high-contrast 3x3 patches of natural images onto a Klein-Bottle, treated these image patches as a large point cloud of individual data records in $\mathbb{R}^9$, collected from millions of natural images. There is no hint on how do such patches within single images spread/cluster within the Klein-bottle, and hence it is not clear how this can be exploited for image analysis.

In general, the possibility of associating topologies (SC shapes) with different special subsets of image pixels/features and analysing/distinguishing images according to the topological invariants of these constructed shapes was overlooked. However, during the years of this research project, there has been a steady growth in the list of research publications that share our approach in investigating topologies with image features for distinguishing between different classes of images or for segmenting regions/objects of interest. Here we shall review a sample of such publications.

Vitaliy Kurlin in [87] developed an algorithm to automatically segment a 2-dimensional cloud of points into regions, that on the input of a dotted image, such as

an image with detected edge points constructs a hierarchy of segmentations into regions whose boundary contours with long enough life span (persistence) in a sequence of nested neighbourhoods of the input points.

Having noted that quantitative features obtained from chest CT scan of the lung (e.g. attenuation area, mean density, airway wall area percentage, etc.) do not sufficiently characterise Chronic Obstructive Pulmonary Disease (COPD). Recently Belchi et al. [11], applied the technique of persistent homology on 3 carefully selected radiomic features that are not visible by the human eye. These features are extracted from inspiratory CT scan reflecting the upwards complexity of the lung consisting of a measure of the upward stretch of branches, the visible length of the bronchial tree, and the number of bifurcations in the tree. They show that each of these features can stratify the inspiratory CT scans of the relatively small experimental cohort into groups in accordance to the guidelines of COPD.

Qaisera et al. [88], designed a persistent homology based automated tumour segmentation in H&E stained histology images. The algorithm work constructs PH profiles of exemplar patches, selected from a CNN training dataset, and uses a variant of k-NN classifier to complete the segmentation. In the adopted k-NN classifier the Euclidean distance metric is replaced with the symmetrised Kullback-Leibler Divergence measure. The PH profile of a patch models the connectivity between cell nuclei. Unlike the case for normal regions, nuclei in tumour areas are closer to each other and difficult to identify individually. Peter Lawson et al. in [89] have recently presented similar work for using PH to evaluate the architectural features in prostate Cancer Histology images.

Giansiracusa et al. in [59] used PH for fingerprint classification. In their approach, they extracted many statistical features from persistent barcode spaces such as average, median and standard deviation of birth and death of bars, polynomial features and regression coefficients. They used fingerprint minutiae points and their orientation as input point cloud to build PH and they report 91% accuracy when tested their approach on NIST fingerprint dataset.

The approach to study topologies of image features or objects, has been recognised over the last few years and as a result many research initiatives have been launched as a result of active work within newly established TDA research networks. In particular

persistent homology provides a topological summary of the shape of the data (e.g., features such as holes) at multiple scales. A key success of persistent homology is the ability to provide robust results, even if the data are noisy.

The common approach of the previous sample of recent research publications is that the PH tools of TDA is applied to specific sets of image features that are identified according to existing knowledge of the application. This thesis follows the same approach but focus on defining a variety of automatically extractable feature sets usable for different applications even without prior knowledge of the images.

Furthermore, the research, in this thesis, was initiated to investigate the development of computational topology inspired algorithms to assess the quality of face images suitable for biometric authentication and detecting potential attacks on face biometrics. The results of these initial investigations revealed great relevance to other image analysis applications. In the rest of this chapter, we present the results of the initial investigations that provide the proof of concept needed to further our research.

3.1.1 Image Quality VS Spatial Distribution of Texture Features

The LBP is an image encoding scheme that re-encodes each pixel value in terms of its order relation to its neighbors. It was originally proposed by Ojala et al.,[90], to characterize texture in images specifically for face recognition. In general, each pixel in the input image will be relabeled by a decimal number that encapsulates the local texture information in its immediate neighborhood. The encoding, is meant to reflect the order relation between a pixel intensity value and those of its surrounding pixels starting from a certain position and in a clockwise direction, resulting in a circular binary string. There are many different LBP encoding schemes depending on the size of the neighborhood, but here we select the 8 immediate surrounding pixels so that each pixel value is encoded as an 8-bits byte.

The LBP encoding process start by subtracting center pixel from its 8-neighbor pixel surrounding it. Starting from top-left corner, each position will be assigned by 1 or 0 depending on the subtraction result based on the following condition:

$$LBP(x_c, y_c) = \sum_{n=0}^{n=7} s(i_n - i_c)2^n \qquad (1)$$

Where n scans neighbors of the central pixel, i_c and i_n are grayscale values of the central pixel and its surrounding pixels, and the function s(x) is defined as:

$$s(x) = \begin{cases} 1 & if \ x \geq 0 \\ 0 & if \ x < 0 \end{cases} \qquad (2)$$

Each pixel in the resulting LBP image is encoded as a byte determined by the 8 s-bits in a counterclockwise order starting from the top-left corner.
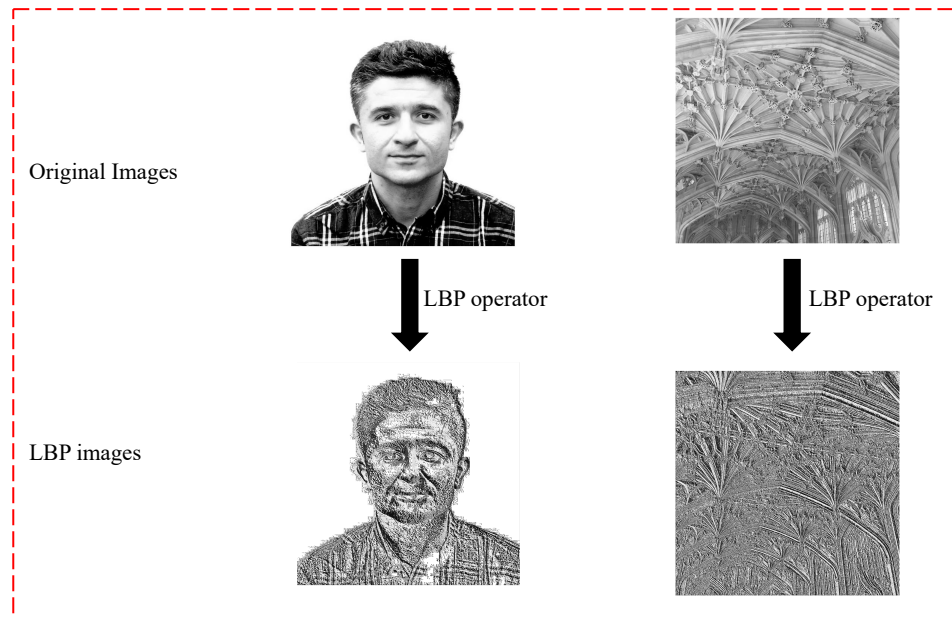
Figure 3-1:An example of LBP operator effect on images.

A uniform LBP (ULBP) is an LBP code that has 0 or 2 bitwise transitions between 0 and 1. It has been shown that in face images ULBP codes constitute 90% of the LBP codes [91]. Applying above procedure on the block matrix will result in getting the binary string 11110000, see figure (3-2).
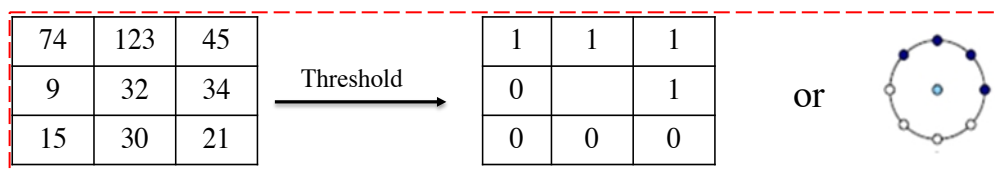
Figure 3-2: Local Binary Pattern descriptor.

Apart from [00000000] and [11111111], there are 56 different ULBP codes forming 7 groups identified by the number of it 1's, and each group consists of 8 different rotated codes. Below is a diagram of all ULBP organised in groups that we call ULBP geometries.

46
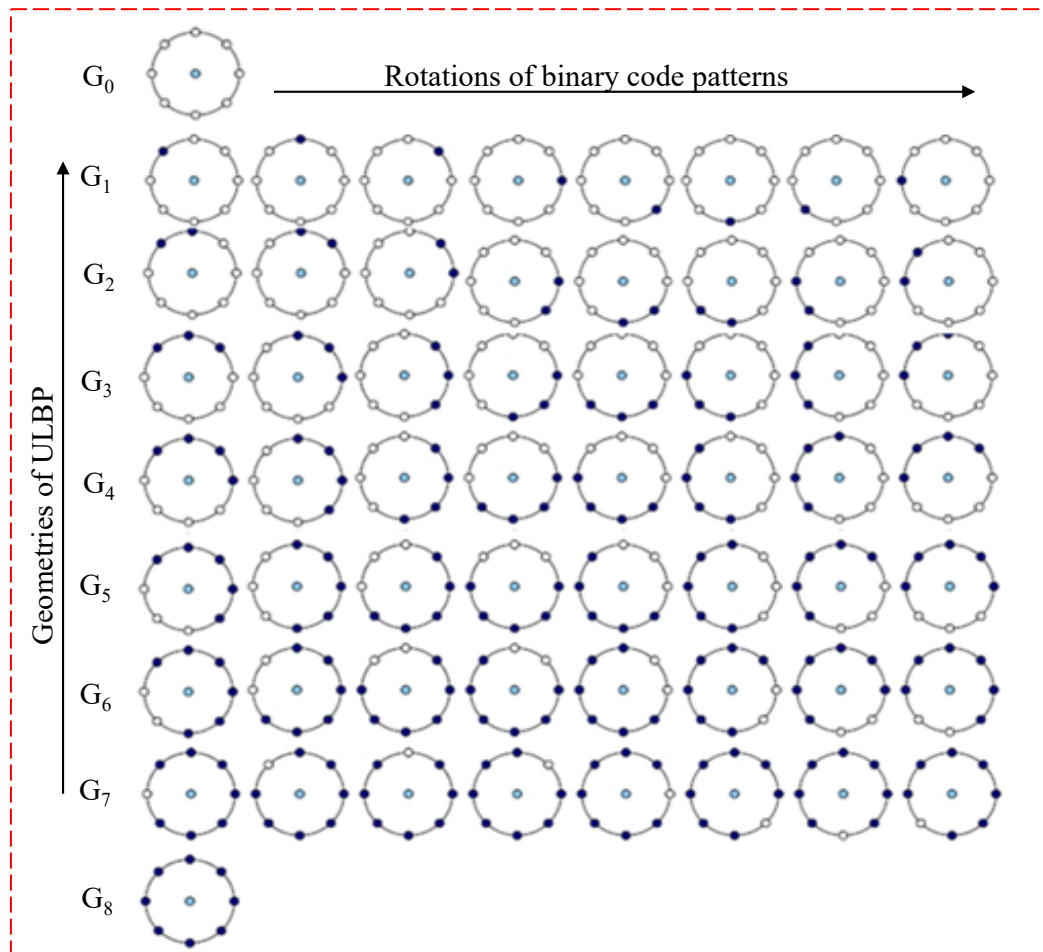
Figure 3-3:Geometric representation of ULBP codes.

Each of these groups is associated with a specific type of image texture. Different ULBP geometries correspond to different types of texture. Based on the analysis conducted by Ojala et al. [92], in natural images some of the ULBP geometries can be classified as follows: G_0 G_1 G_2 G_3 G_4 G_5 G_6 G_7 G_8

- G_0 and G_8 describe flat and spot regions.
- G_2 and G_4 describe edges in the images.
- G_3 and G_5 describe corners in the images.
- G_6 represent line ends in natural images.

This classification is slightly different for face images and the ULBP groups in face image represent textures as follows:

- G_0 and G_8 describe flat and spot regions, similar to natural images.
- G_5 correspond to edges in the face images.

47

- G_1 and G_7 represent End of lines in face images.
- G_2, G_3, G_4 and G_6 represent corners in face images.

We shall now determine the effect of various image degradation on the spatial distribution of some of the groups of uniform LBP points modelled by the Rips SCs at some distance threshold. Note that the elements of these groups are determined automatically.

3.1.2 Image Quality: Effect on Topologies of ULBP groups

Digital images are subject to many distortions while processing, transmission, storing and compressing resulting in a variety of image quality degradation. Digital image processing, in general, can change the appearance of images in a way that human visual system will judge the change either beneficial or injuriously. Widespread social media and photo sharing platforms, such as Facebook, Instagram, Snapchat, twitter and others, made it easy for users to apply beautification filters such as noise removal, skin smoothing, inserting objects and removal of unwanted object. Malicious image manipulations, on the other hand, can have many forms including copy-move and fake images/videos intended to conceal the true message the image conveys or to create false evidences. In the last scenarios, image inpainting algorithms (image enhancement) often are applied to hide the manipulation artefacts and maintain a visually acceptable quality of the resulting image. However, it is known that such procedures inevitably result in tiny and localised changes to the images in different places that can only be detected by sophisticated forensic-based techniques.

Furthermore, degradations may occur naturally as a result of biological and genetic changes such as cancerous cells that changes the texture of scanned tissues. Environmental factors such as radiation can also change the texture of scanned tissues in human body. Therefore, image quality assessment plays an important role for a variety of computer vision applications including forensics and diagnostics.

In [93], we developed a TDA-based image quality assessment method for the evaluation of shadow and blurring effects on face images. We constructed Rips complexes from digital images based on certain image landmark pixels that convey textural information from images, namely subsets of ULBP codes. We constructed

the corresponding Rips complexes over a range of distance thresholds, and at each threshold we computed the Betti numbers B_0 and B_1. We noted that these values are sensitive to image quality. In particular, we demonstrated that the topology of the digital images will be changed as a result of image degradation, and hence topology can be used as a new sophisticated tool to quantify the quality of digital images.

In figure (3-4), we illustrate the effect of appearance of different level of shadow in face images on the constructed Rips complexes from the corresponding faces using R_2-G_7 of ULBP at a given threshold.
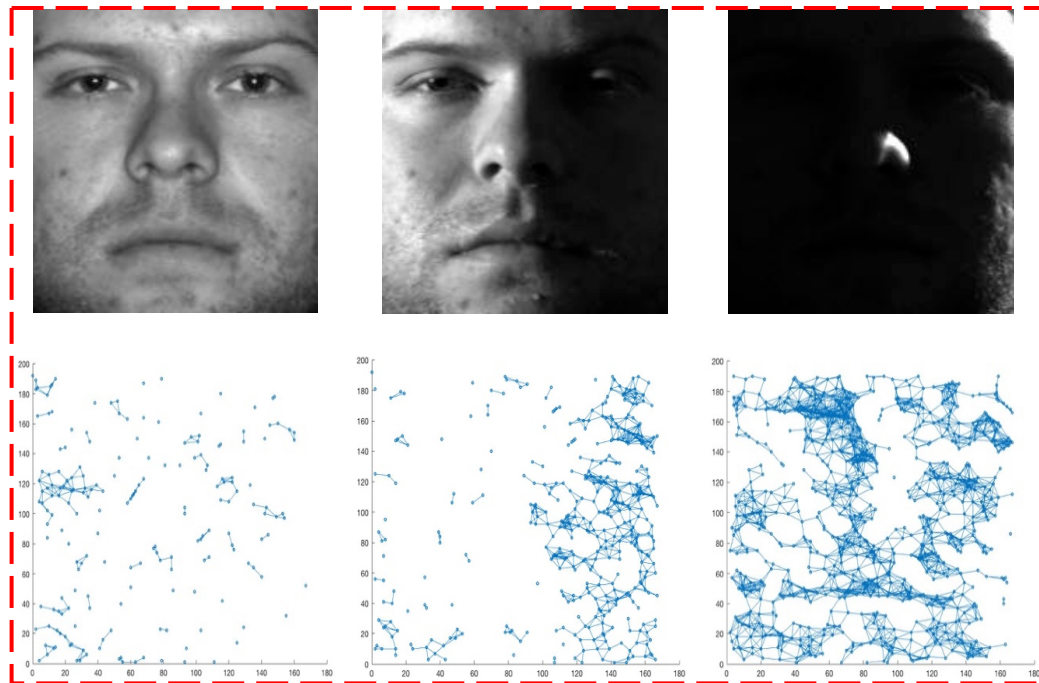
Figure 3-4: Example of Rips complexes built based on 2nd rotation of $\boldsymbol{G_7}$ of ULBP from face images that have different shadowing effects.

The above figure clearly illustrates that when half of the face has shadow effect on it, the corresponding Rips complex clearly depicts that effect. For both landmarks, the Betti number B_0 is reduced noticeably because the pixels in that shadow region are much closer to each other than those in the non-shadow regions. This effect is more apparent when the shadow is on the entire face, the B_0 decreases drastically.

The appearance of shadow in images are not restricted to natural images. In ultrasound scan images of tumor tissue, shadowy regions indicate the presence of solid tissue/organs in the path of the emitted sound waves. Such features are

indicative of the medical abnormalities [9]. The following example illustrate the effect of such features on the topological parameters of a ULBP group 7.

Benign	Malignant
Rips SC for 2nd rotation of G7 of ULBP at $t = 20$.	Rips SC for 2nd rotation of G7 of ULBP at $t = 20$.
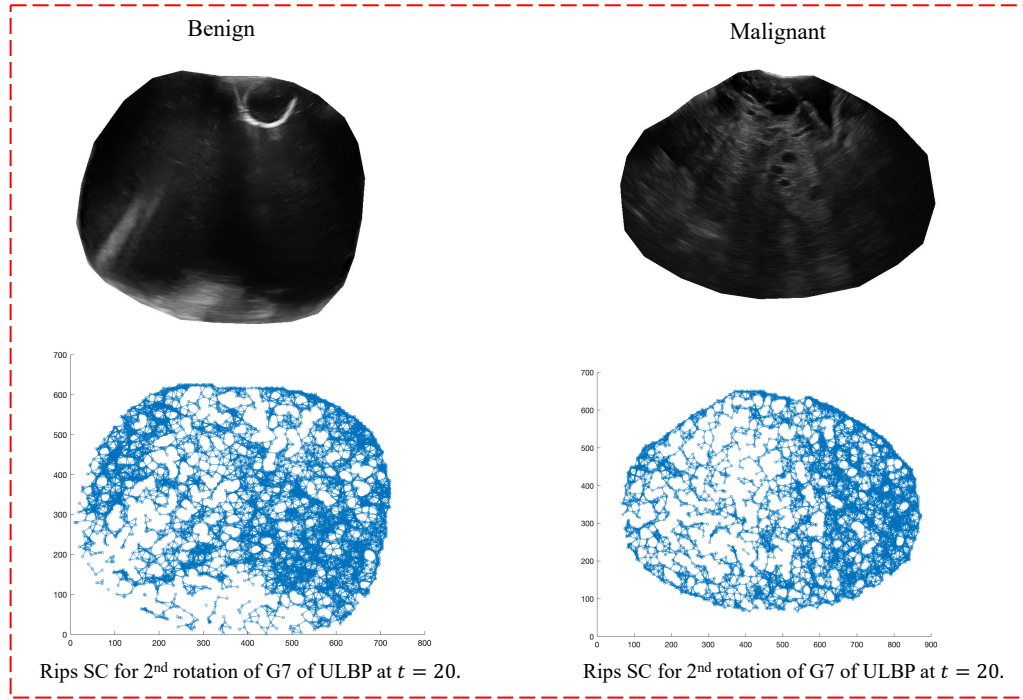
Figure 3-5: Effect of shadow in produced Rips complex of Ultrasound ovarian tumours.

Image blurring can happen for a variety of reasons. For example, applying Gaussian filters to get rid of grainy effects of the presences of noise results in blurring the image. High ratio compression, capturing images at a distance, or out of focus recording. In satellite imagery, turbulence blurring is a common problem modelled by the following exponential formula [94]:

$$H(u, v) = e^{-\mathcal{K}(u^2+v^2)^{5/6}}$$

where $\mathcal{K}$ is a constant represent the blurring level and u, v is the pixel indices.

In the following, we illustrate the effects of different type of blurring on the topological parameters of the Rips complexes associated with an example of ULBP group landmarks. Figure (3-6) illustrate the effect of blurring (turbulence blurring with blurring level of 0.01) on the simplicial complexes constructed using ULBP codes (Geometry 4, Rotation 1). The number of Landmarks of normal face is 1269 whereas the blurred images have 2316 and 1883 landmarks for Turbulence-Blurring at 0.01 and 0.03 respectively.
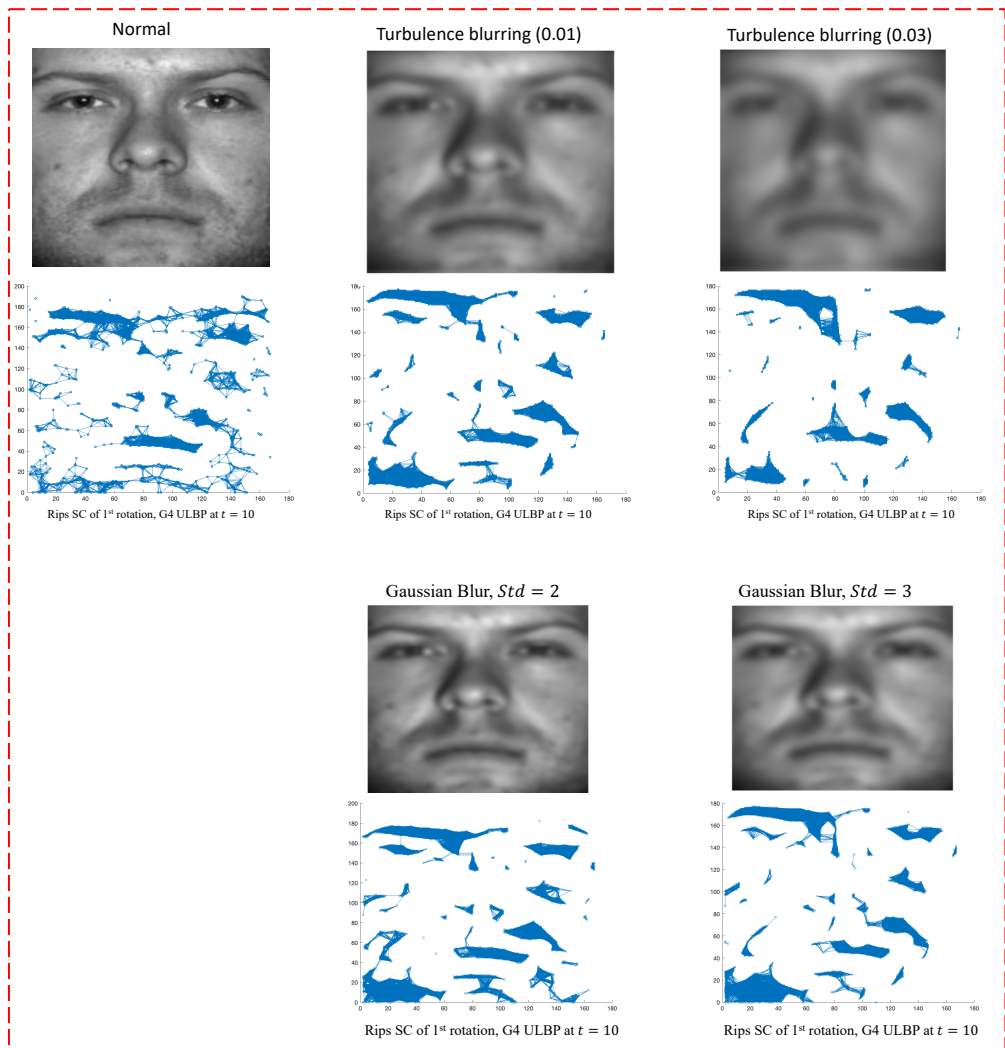
Figure 3-6: Effect of different types of blurring on Rips complexes and topological invariants.

Image noise is another feature of quality degradation that occur for a variety of reasons mostly related to the image recording devices. There are different types of image noise including Salt and Pepper, Gaussian and exponential types as well as non-periodic noise. In medical images a special type of noise, known as *Speckle* noise, to infect to a different level of ultrasound images have an impact on manual as well as automatic diagnostics. Each of these different types of noise require different de-noising algorithms (e.g. see [94]). Below, we illustrate the effects of different type of noise on the topological parameters of the Rips complexes associated with an example of ULBP group landmarks.
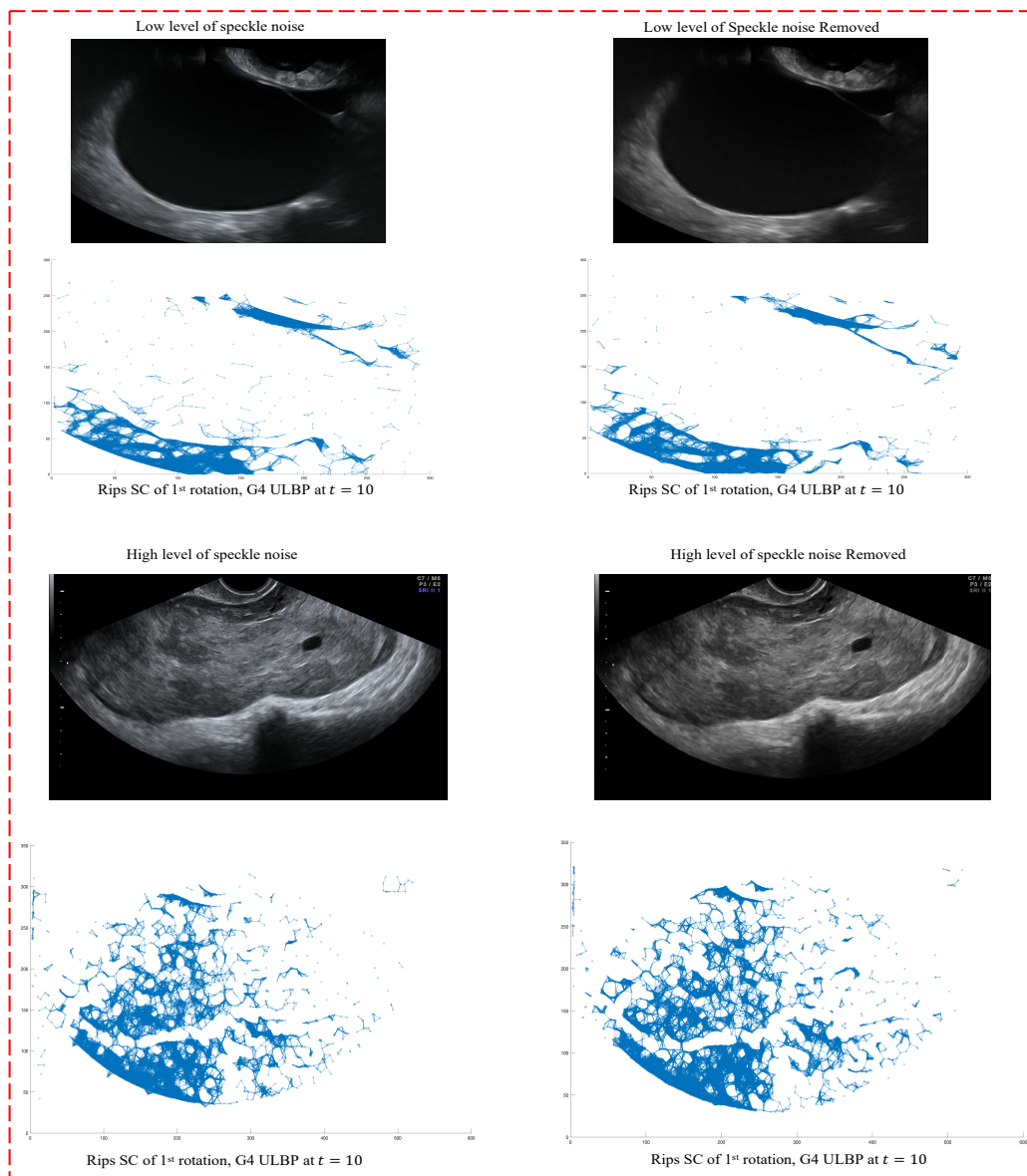
Figure 3-7:Example of noise in medical images and the effect before and after noise removal on Rips complexes.
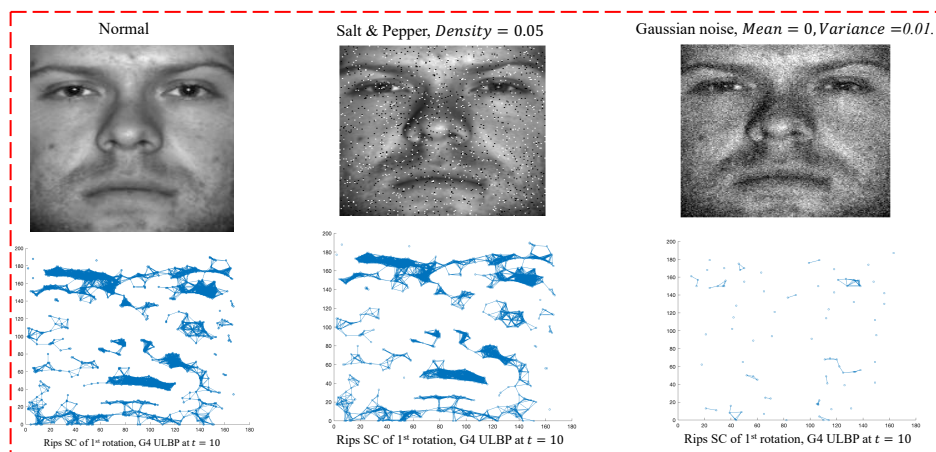
Figure 3-8: Effect of Gaussian and Salt & Pepper noise on Rips complexes.

Previous figures demonstrate that Rips complexes constructed on images (face image or biomedical images) react differently on different types of noise. In the case of ultrasound ovarian images, whether it is high or low level of speckle noise, removing noise will result in increasing the number of topological invariants in both dimensions relative to the level of noise exist. Low level speckle noise removal increases topological invariants by a small fraction, for example the number of 1-dimensional holes increased from 581 to 613 whereas in the case of high-level speckle noise removal, the computed number of 1-dimensional holes increased from 904 to 1177. Adding Gaussian noise or Salt & pepper noise to face images reduces its topological parameters. Gaussian noise reduces the topological parameters drastically, for example the number of 1-dimensional loops reduces from over 280 to below 20 loops, see figure (3-8)-right. In the same vein, Salt & pepper is also reducing face image topological parameters but not as drastic as gaussian, for example the number of 1-dimensional holes reduced from 285 to 217 loops only. The number of 0-dimensional holes, i.e. connected components, follow the same behaviour as 1-dimensional holes except in low-level ovarian ultrasound speckle noise removal. Ovarian ultrasound images' connected components increased from 4094 to 4970 after high-level speckle noise removal whereas low-level noise removal reduced connected components from 2176 to 2159. The number of topological parameters reported here is based on topological parameters calculated from the persistent barcodes constructed from the distance matrix among image pixel landmarks.

In summary, it can be seen that the natural pattern of topological parameter of images are distorted when we add noise to images. Interestingly, the change of topological parameters is not random, rather it follows a pattern which can be used to model different type of noise.

3.2 Face Image Morphing

Having demonstrated the link between different forms of image quality degradation and TDA based topological parameters of Rips SC's associated with certain ULBP landmarks, we shall now initiate our investigation into the use of TDA to deal with the recently emerging challenge of detecting malicious generation of fake images that

has serious security implications. In particular, we focus on the so-called face image morphing. We shall first describe the morphing attack, highlighting some known techniques of creating morphed face images/photographs, and finally explaining the link to TDA use for the appropriate image analysis task of automatically distinguishing morphed and genuine face images.

In general, image morphing is the process of transforming one image into another through a seamless transition. Morphing requires a set of corresponding landmark points from the input images. The two input images are 'source' and 'target' images from which intermediate frames will be generated using blending procedure. Image blending is a linear combination of the source and target image pixel values using the following formula:

$$I_b(i,j) = \alpha \times I_s(i,j) + (1 - \alpha) \times I_t(i,j)$$

where I_b is the blended image, $i \, and \, j$ are image pixel values, I_s and I_t are source and target images respectively and α is the blending factor specified by user. Furthermore, the blending factor α is the proportion of the pixel intensity values used from the source and target image in the resulting (morphed) pixel intensity value. It has been reported in [95] that $\alpha = 0.5$ is producing a realistic morph and hence in that case blending process is similar to averaging pixel intensity values. To obtain visually faultless morphs, one needs to align the source and target images in advance such as eyes, nose, mouth and face contours, known as Facial landmarks (keypoints). Finally, warping functions will be applied which are triangles built from triplets of facial landmark points. There are several techniques of image warping reported in the literature [96], but the Delaunay triangulation yields convincing results [95]. The two sets of face Landmark pixels (from both source and target images) represented as a topologically equivalent triangular meshes where folding and discontinuities are not allowed [97]. Using standard affine transform, each warped triangle is mapped to its triangle in the original image.

In general, one can warp images using 'forward' or 'reverse' mapping procedure. Forward mapping process maps a pixel in the source image to its corresponding location in the destination image whereas reverse mapping takes a pixel in the original images and searches for its colour in the destination image. Forward mapping results in producing unpainted pixels in the destination images whereas reverse

mapping guarantee that each pixel in the destination image obtained a value[95][97]. See figure (3-9) for a pictorial representation of morphing process pipeline.
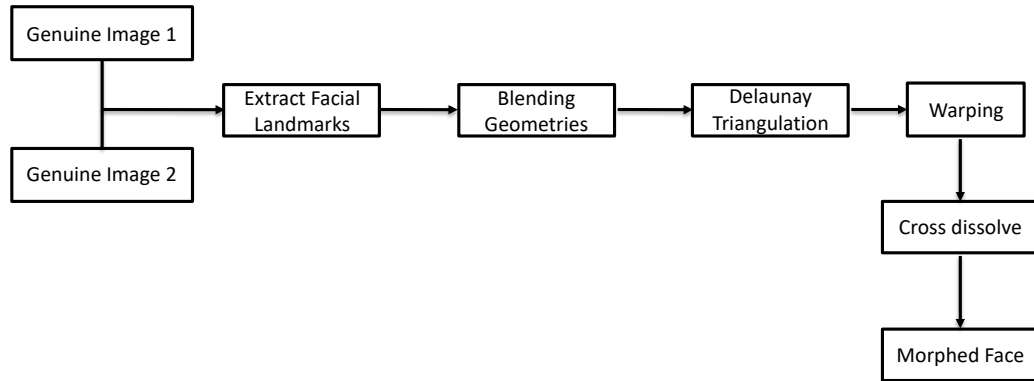
Figure 3-9:General pipeline of morph creation.

  Next, we describe the three morphing techniques used for investigation in this thesis such that any morphing approach will fall under one the three techniques we will be discussing. Facial landmarks used are 97 points as follow: 68 landmark points selected using *shape-predictor* function from *dlib* (http://dlib.net/), 2 landmarks from pupil of the eyes and finally 7 landmark points on the forehead. Alpha blending factor is 0.5, which means both source and target images are contributing equally to produce morphs. Hence, the blending process becomes similar to averaging the pixel values.

3.3 Techniques of Face Morphing

The quality of the produced morphed facial images needs to satisfy two conditions; (i) morphed face images need to be visually faultless to layman eyes (i.e. no visible artefacts) and (ii) produced fake faces should be successfully verified against both source and target images by automatic face recognition systems. The three types of morphing techniques are complete, splicing and combine morph. **Complete morph** process starts by adding another 20 landmark points on the border of the two input images (i.e. source and target) then average of these landmarks used in Delaunay triangulation. Then the resulting triangles from both source and target images are warped into an average position before averaging the two warped images which in fact is the morphed image. This way resulting morphed facial images have mutual texture and geometry taken from both images. produced morph suffers from spurious

shadows and clear visual artefacts which is one of the disadvantages of complete morphing process. **Splicing Morph** process, on the other hand, proposed to overcome the issues occurred in complete morph technique. After extracting the 77 landmark points, a convex hull will be cut from both source and target images and average landmark-point coordinates used in Delaunay triangulation. Triangles from both source and target images are then warped into an average position before taking the average of the two, frontal face, images. Produced (frontal) morphed face is then warped back to the face positions of both source and target images. As a result, this technique can be used to morph more than one face images. Shortcoming of splicing morph technique is that, the geometry of the produced morph is taken from one of the faces, either source or target face image. Therefore, splicing morphs are matching well with one of the input images, and matching with the second input image require similar geometry from both input face images. Finally, splicing morphs also producing minor ghosting artefacts due to inaccurate facial landmark point localizations[98]. Splicing and complete morph technique proposed by [95].

Apart from the factors discussed above, other factors such as variation in skin color and face obstruction by hair are prohibiting morphs from appearing realistic. In the case of splicing morph, when source and target face images have different skin color, then produced morph does not look realistic. **Combined morph** technique proposed in [99] to overcome the limitations in the previous two techniques. Combined morph technique starts by first warping the images into an average position first, then cut the facial regions, blending and then stitching it back on the warped images. To obtain seamless transition between the frontal face region and the forehead region, Poisson image editing applied to this region and the rest of the image. Produced morph using combined technique has an average texture and geometry from both input images, has no major ghosting artefacts and skin colour has no influence. See Figure 3-10 for an illustration of the three algorithms of morphing generation. The face images used to create morphing are from Utrecht-face dataset [100], using complete, splicing and combined technique. Utrecht dataset is containing 75 genuine faces which we will use in our experiments in chapter 4 and chapter 5. From the 75 Utrecht genuine faces, 1298 complete, 2612 splicing and 2650 combined morphed face images generated. Beside the 'digital' face images, we will also investigate the print-scanned face images, using a small dataset of face images provided by our collaborators at the uni-

Genuine Faces	Complete Morph	Splicing Morph	Combined Morph

Ghosting artefacts

Transition between forehead and frontal face is noticeable .
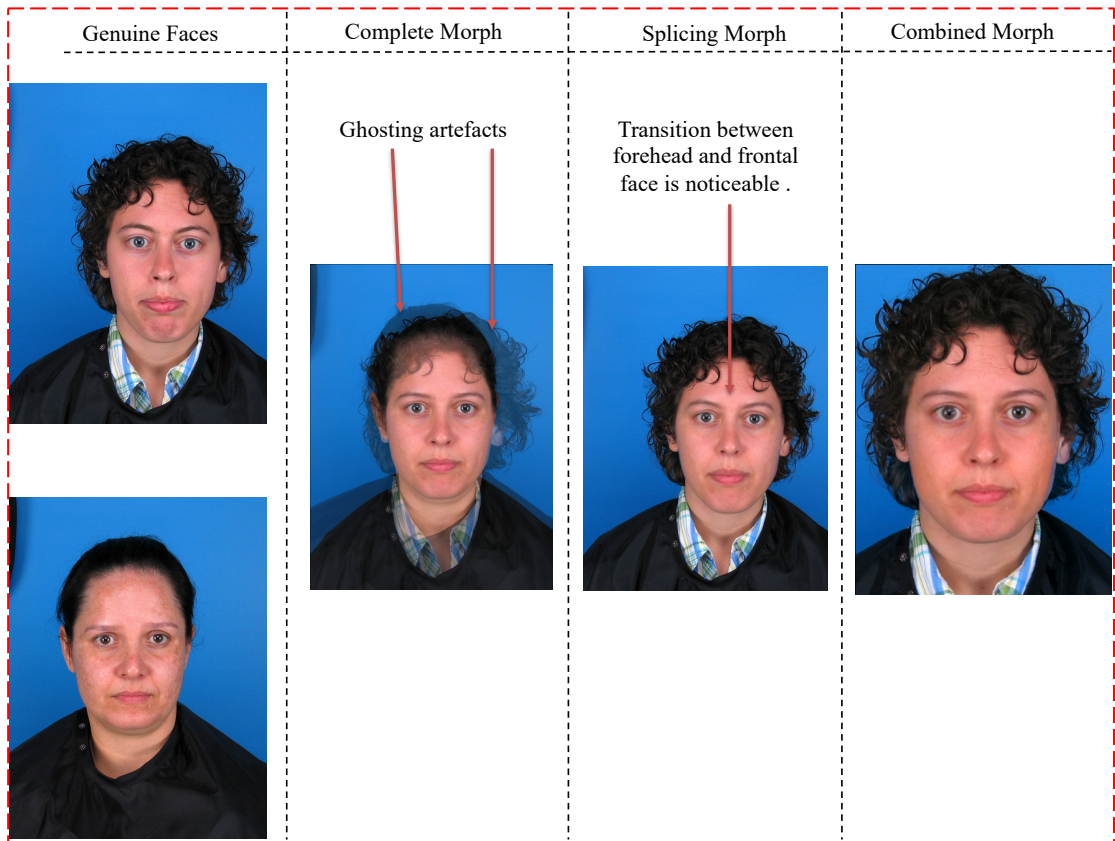
Figure 3-10: Illustration of different types of morphing techniques**.**

versity of Magdeburg, Germany. The dataset consists of 142 images, 71 genuine faces from Utrecht dataset and 71 morphed (splicing) faces. More specifically, the images scanned using CanoScan model 9000F MarkII by our collaborators from Advanced Multimedia and Security Lab (AMSL) at Otto-von-Guericke-University of Magdeburg, in Germany. Print-scanned (P&S) images were in different resolution ranging from 121x136 to 2017x2517, and hence we rescaled them into 220x270. All of the morph images in this thesis have been produced by AMSL at Otto-von-Guericke-University of Magdeburg, in Germany.

Digital face image	597x797 P&S with 200dpi	1149x1558 P&S with 200dpi.
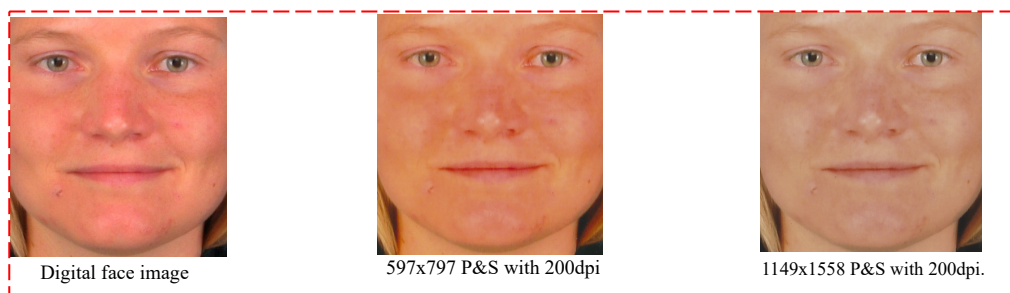
Figure 3-11: Illustration of Print-scanned process on the quality of face images.

3.4 Threat of Morphing on Face Biometrics

Face biometrics is a natural tool for recognition and identification tasks such as in border controls, surveillance, law enforcement, eCommerce, eGovernment applications and user identification and verification in mobiles and tablets. Automatic recognition of persons' face biometrics, with high accuracy in controlled environments, promoted face biometric to have a strong and eminent role in Automatic border controls (ABC) systems. Among the reasons face biometric chosen for ABC systems is the fact that when face recognition systems alarming false negatives, border control officers can conduct a visual inspection [101]. This is one of the unique advantages of using face biometrics over other biometric forms such as fingerprint recognition and iris recognition. ABC systems incorporate electronic machine-readable travel documents (eMRTD) such as e-passport[102]. E-passports incorporate a face image (digital or print-scanned version) of the holder in order to be used by ABC systems together with a live digital face image as the only biometric reference for verification. Furthermore, face image is the primary identifier required by international civil aviation organization (ICAO) for eMRTDs. Vulnerability of face recognition algorithms to different types of attacks in ABC systems gained more attention when ABC systems widely deployed in airports at beginning of this century. In general, there are two types of attacks on ABC systems; (i) presentation attack (or face spoofing) which is an attack on ABC system and (2) morphing attack, which is an attack on eMRTD biometric reference. Presentation attacks on ABC systems are normally targeting the camera devices deployed in ABC gates by presenting a face artefact. This attack requires access to (lost or stolen) passports (or IDs) so that the criminal prepares the face artefact(s) necessary to resemble the (innocent) face photo incorporated on the e-passport.

On the other hand, morphing is an attack on eMRTD to tamper the biometric information stored on e-passports. Morphing attack on eMRTD is simpler to conduct in comparison with an attack on ABC systems. Since most of the countries worldwide accept (printed) face images in passport issuing applications, this is an adequate opportunity for a criminal to submit a morphed (manipulated) face image and in return receive an authentic e-passport. An e-passport obtained this way will eventually contain all physical and electronic security features deployed by the passport issuance body but with a morphed image on it. As a consequence, the

morphed facial photo on produced e-passport constitute from facial features of multiple persons faces contributed to the morphed face. Hence, the passport can be used by multiple persons because recent researches demonstrated that this kind of e-passports can bypass both face recognitions systems in ABC gates as well as border control officers [103]–[106].

Although, manual examination of morphed images do not succeed in distinguishing fake (i.e. morphed) face images from genuine face images, in the following illustration we should see that TDA, in the form of topological parameters of Rips complexes of certain automatically (non-random) ULBP, seems to encapsulate evidences of foul play that could be developed into effective morphing detection tool.
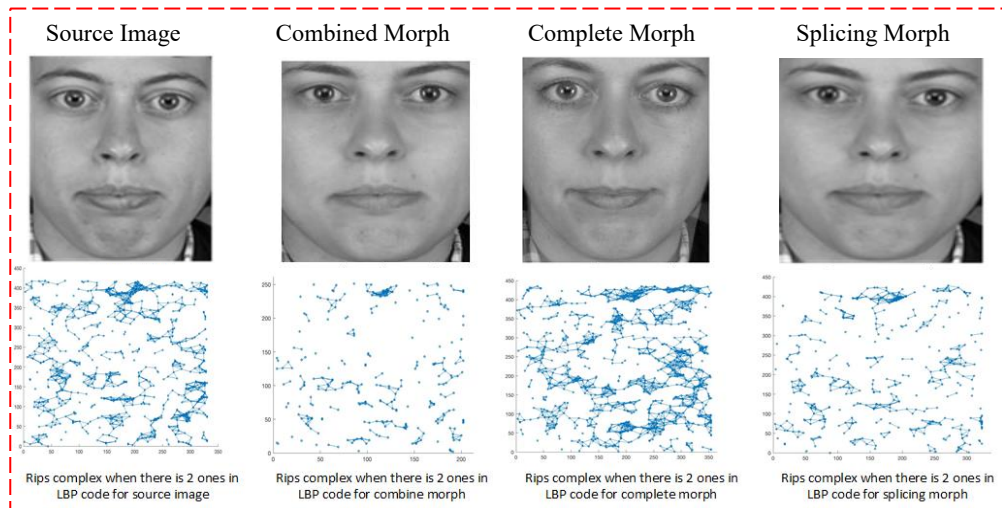
Figure 3-12: Rips complexes constructed from genuine and fake faces.

In summary, designing sophisticated forensic tools to combat morphing attacks on ABC systems and helping officers in border controls is an immediate need. Inspired, by the above observations, the next two chapters are aimed to reporting on the research conducted in this project to the design, development, and performance evaluation of our PH based face image morph detection tool.

Chapter 4

Image Tamper Detection- A Homological Approach

Having introduced in chapter 2 the mathematical background for TDA, and its main tool of PH, for image analysis, chapter 3 focused on arguing for adopting a specific TDA approach to image analysis that exploit the spatial distribution of texture features within each image, and demonstrated that subsets of LBP texture features extracted from some images exhibit sensitivity to image quality and to face morphing attacks. In this chapter, we shall build on the observations made in chapter 3, to conduct pilot study with a sufficiently large mix of genuine and morphed face images in order to formulate a hypothesis about the separation of the distribution of their homology parameters at chosen thresholds. This chapter is devoted to the development of a PH-based scheme suitable for detecting tiny invisible changes to face images as a result of morphing attack. The literature of other morph detection techniques proposed by other researchers, together with introducing the building blocks that eventually contribute to PH-based morph detectors. Vietoris-Rips (Rips) simplicial complex construction and a hypothesis to extract features from persistent barcodes discussed which we named *persistent-binning*. We illustrate the effectiveness of persistent-binning using different machine learning classifiers such as Bayesian and K-nearest neighbor (KNN). This first attempt in using homological approach to morph detection will be tested on a large number of face images together with a critical evaluation towards the end.

4.1 PH approach to Face Morphing detection: Introduction.

In chapter 3, we described different professionally designed techniques to launch morphing attacks on face images, which seem to be a challenge to distinguish the genuine from morphed images by human or machine [107]. We also observed some interesting impact of various image quality degradations and morphing attacks on the spatial distribution of some primitive texture landmarks. We deduced that these observations, albeit with few examples, is worth investigating the consequent

topological structure of the spatial variation of these landmarks by conducting a wider extensive research into the use of TDA tool of PH for the detection of image tampering and focusing initially on face morphing attacks as a case study.

To design a PH-based face image morphing detector, we need to represent a face image by a point cloud set that is highly sensitive to morphing, and ideally such a set consists of automatically extractable landmarks of pixels in the image. Morphing is expected to distort some texture and/or structural primitives in the face image region. Locations of many image texture primitives provide a rich source of landmarks. Fiducial face image pixel positions around the eyes, nose, mouth and chins are useful landmarks, but their detection is inefficient. Hence, one should opt to automatically extractable texture-related landmarks. Variation in intensity within 3×3 image patches convey reliable information about the spatial domain image texture primitives and have been shown to have geometric structure [7]. It is natural to consider the central pixels of such patches as source of landmarks to be tested for their sensitivity to morphing. Our investigations conducted for this thesis assures us that this is indeed a very rich source of tamper-sensitive landmarks to extract topological template representation for various image analysis tasks far beyond distinguishing morphed face images from genuine ones. In fact, it is unrealistic to consider other than few such examples of landmark sets sufficient to support our thesis that image analysis benefits greatly from adopting TDA approaches.

In order to introduce and prove the concept of TDA-based approaches to tamper detection, we shall confine the discussions in this chapter on the sets of spatial domain landmarks of uniform Local Binary Patterns (ULBP), as discussed in chapter 3 (section 3.2.1), that incentivised this research at the outset. As observed, groups of ULBPs have local geometric significance and their Rips-simplicial complexes are highly sensitive to face morphing attacks. The ULBPs consist of 7 groups of LBPs, called G_λ-geometries for $\lambda = 1, ... ,7$. Here, λ refers to the number of 1's in its binary representation. Each G_λ consists of 8 binary codes that can be obtained from each other by a circular rotation. The set of ULBP image pixel positions forms a very large source of image landmarks that are sensitive to pixel value changes. For efficiency purposes, we use each and every rotation in each G_λ group as a separate landmark set and for the intended PH morph detector, we shall build in parallel a separate nested

simplicial complex for the eight rotations in G_λ and create one feature vector representing their PH parameters.

In order to inform the objectives of this research, it would be beneficial to review existing work on morph attack detection next.

4.2 Morph Detection – A review of Existing schemes

In 2014, Ferrera et al [103], highlighted the seriousness of morphing attacks on face images for biometric passports by stressing that neither human nor machine can effectively deal with the challenge of distinguishing the genuine from morphed face images, and this was confirmed by many researchers since. Many techniques proposed to detect morphed face images after Ferrera et al. in [103] first illustrated that morphed face images can bypass all integrity and authentication (optical and electronic) checks. Later, the failure of automatic face recognition (AFR) systems as well as human ability to detect morphed faces have been confirmed in [105] and [107]. This alarming failure of AFR, motivated research into designing and testing morph detection/prevention schemes. However, recognising that any image tampering no matter how sophisticated results in some, perhaps tiny and invisible, changes manifested by quality degradation and texture distortion is an incentive for the development of forensic-type of approach to tamper detection. Over the last four years, triggered by the urgency of these attacks, many such schemes were proposed, and we shall now review few such examples.

Raghavendra et al. in [101] proposed a morph detector model based on micro-texture variation using binarized statistical image features (BSIF). The dataset used was an in-house dataset not available publicly. A subset of the same dataset was used by Scherhag et al. [104] to check the performance of the same algorithm to detect print-scanned images.

Makrushin et al. in [95] proposed a forensic-based scheme to detect morphed faces that exploit knowledge of Benford features of quantized discrete cosine transform of JPEG compressed images. Benford's law states that leading digits of naturally generated random data have a logarithmic distribution, and the authors demonstrate that digitally created morphs violate Benford's law. Hildebrandt et al. in [108] investigated the influence of different image post-processing approaches (e.g.

additive noise, scaling and rotation) on the Makrushin et al's morph detector using anti-forensic methods, such as StirTrace, and reported that StirTrace processing has a significant impact on morphing detection. In particular, they concluded that adding noise will result in morphed images to be classified as genuine ones. Tom Neubert in [109] presented a progressive image degradation effect, mainly JPEG compression, to discriminate legitimate face images from morphed ones, and concluded that JPEG compression strongly affects genuine images but not morphed images.

The Magdeburg research team extended the use of Benford's Law and StirTrace to further boost the morph detection performance in [110],[99] and [111]. Kraetzer et al in [112] , observed that the blending step in the digital morphing processes, described in chapter 2, produces artefacts and reducing face details. This led to extracting various types of features from face images such as Scale-Invariant Feature Transform (**SIFT**), Speeded Up Robust Features (**SURF**), Features from Accelerated Segment Test (**FAST**), Oriented FAST and Rotated BRIEF (**ORB**), Adaptive and Generic Accelerated Segment Test (**AGAST**) using OpenCV library together with Canny and Sobel edge detectors to improve the accuracy of their morph detection accuracy tested on an in-house database.

Beside manipulating face details (textures), morphing process changes the entire image signal. Therefore, it is natural to consider analysing the changes in Photo Response Non-Uniformity (PRNU), which is a unique noise pattern originated from each single camera and it is distinct for each model. In [113], face images been divided into 4 blocks (Cells) and PRNU extracted from each block. The authors illustrated that PRNU is robust against post-processing of morphed images such as scaling and image sharpening but fails in the case of histogram equalisation. In the same vein, Zhang et al in [114] proposed a morph detection technique based on extracting Sensor Pattern Noise (SPN) in Fourier spectrum from the entire image.

Different versions of Local Binary Patterns (LBP) used to design morph detection algorithms. Raghavendra et al [115] used LBP as a feature map to train Probabilistic Collaborative Representation classifier (PCRC) where they focused on the difference between face averaging and morphing in their evaluation. An in-house dataset of morphs from Generative Adversarial Networks (GANs) used to test the effect of LBP features for morph detection in [116]. The SVM classifier was trained on High-

dimensional LBP [116] and high morph detection performance reported in [117]. On the other hand, an extensive investigation on score-level fusion of different types of features conducted in [118] by combining LBP, SIFT, BSIF, SURF, Histogram of Oriented Gradient (HOG) and OpenFace [113] deep features. The authors conclude that while computationally this approach is costly, fusing more than one feature extractor improves the morph detection performance.

Although standard passport images need to have minimum light reflections, especially specular reflections and hot spots, in [119] the authors proposed a morphing detection algorithm that depend on the inconsistency of light source reflection between morphed and genuine images. they conclude that, direction to light source based on the reflections in eye and nose regions from genuine images have a different pattern in comparison with morphed images.

The emergence of deep neural network learning approach to Artificial Intelligence over the last few years and the success achieved in some image analysis tasks seem to have triggered the developments of deep learning based morph detection schemes. The two deep Convolutional Neural Networks (DCNN), VGG19[120] and AlexNet[121], have been deployed in a transfer-learning mode for the detection of both digital and Print-scanned morphing attacks in [122]. Another deep learning based morph detector was developed at the same time by Seibold et al [123], that added the GoogLeNet [124] architecture to the VGG19 and AlexNet, as pre-trained and non-pre-trained models. To overcome the problem of overfitting, the DCNN architectures trained on images where specific regions such as eyes, mouth and nose are covered, as an attempt to prevent the networks focusing on specific regions on the face. In [125], two more architectures used for morphing detection, VGG-Face [125] and FaceNet[126], whereby the authors reported that extracting features for face recognition purposes can also be used , at the same time, for morphing detection in ABC systems.

Most existing morph detection algorithms assume no prior or additional information about face images available in ABC systems, and hence known as no-reference morph detection. In ABC scenarios, a live photo of passengers serves as an additional source of information which can be used to further assist morphing detection. Morphing techniques designed based on the availability of a live photo as well as the

64

face photo in ABC database are known as differential morphing attack (or image pair-based morphing attack).

Despite the fact that existing morph detection algorithms can be adapted to differential morphing attack, many algorithms designed specifically for differential morphing attack scenario. In this vein, Ferrara et al. in [97] proposed a de-morphing technique that require a trusted live photograph to be aligned with a suspected morph image. Next, apply the inverse of morphing operation, by subtracting the live image from the stored image retrieved from the database, then compare the obtained image with that of the trusted-genuine live image. The hypothesis is that, if two faces contributed to produce a morphed image, and one of the faces subtracted from the morphed image, then the second face remains. In [127], the authors confirmed that the performance of de-morphing process significantly drops in the presence of face pose variations leading to a large number of false morph alarms. Another method to detect differential morphs in ABC systems is based on facial landmark positions and angles [128]. This technique is based on extracting 68 landmark pixels' position and angle from face images, yielding low performances (below 70% overall accuracy) making the proposed approach unsuitable for real-world applications.

While most of the above morph detectors depend heavily on image texture analysis and for the sake of improving detection accuracy they combine a variety of such features to detect the tiny changes in face images as a result of morphing process, none seem to pay any attention to the spatial distributions of the extracted features. The deep learning morph detectors goes to the extreme of extracting all sorts of features so much so that their decisions cannot be explained, i.e. it works as a black box.

In contrast, the main innovation of this thesis is that the spatial distribution of many single texture features provides the ingredients for TDA based effective morph and tamper detector schemes. The rest of this chapter is aimed at establishing the hypothesis using the groups of the ULBP described in last chapter. We shall also demonstrating the validity of this hypothesis throughout the following chapters with several other feature landmarks and beyond the morphing attacks.

4.3 Vietoris-Rips of Image Landmark Point Cloud

We shall now briefly, describe the process of modelling the shape of landmark point clouds, extracted from a digital image. The intention is to use ULBP groups, but it is applicable to any other extracted landmarks. Given a set of grayscale landmark pixel candidates

$$P = \{p_1(x_1, y_1), p_2(x_2, y_2), \dots, p_n(x_n, y_n)\}.$$

First, calculate the Euclidean distances between all pairs of landmark pixels, and store in a non-decreasing order. There needs to be a distance threshold parameter t, to build Vietoris-Rips simplicial complexes (or Rips Complex for short). There exists more than one approach to selecting t, for instance one can determine the minimum and maximum distance between landmark pixel values $\{T_{min}, T_{max}\}$. Then select k-equidistance thresholds $T = \{t_1 = T_{min}, t_2, \dots, t_k = T_{max}\}$. For simplicity and computational efficiency, we fix $k = 100$ but k can be changed to suit the range of distances. Next, construct a sequence of Rips complexes iteratively by joining landmark pixels in P if the distance between them satisfy the relation

$$T_{i-1} < t \leq T_i \quad for \ i = \{1,2,3, \dots, k\}.$$

At each t, calculate the number of 0-dimensioanl homology groups, i.e. 0-betti numbers are corresponding to the Rips complexes $(B_0(Rips_{t_i})$. We stop the process when $B_0 = 1$, otherwise increment i and repeat. The output of this process is the following sequence of 0-betti numbers (i.e. connected components):

$$\left(B_0(\mathbb{S}_{t_0}), B_0(\mathbb{S}_{t_1}), B_0(\mathbb{S}_{t_2}), \dots, B_0(\mathbb{S}_{t_k})\right)$$

Here, $\mathbb{S}$ is the Rips complex constructed at the terminating threshold t_j where $B_0\left(\mathbb{S}_{t_j}\right) = 1$, when all nodes get connected first time. It is worth noting that, different landmark pixels may have different threshold interval partitioning procedure as well as different length of Rips complex sequence. In figure 4-1, we give an example of Rips complex construction from the process described above.
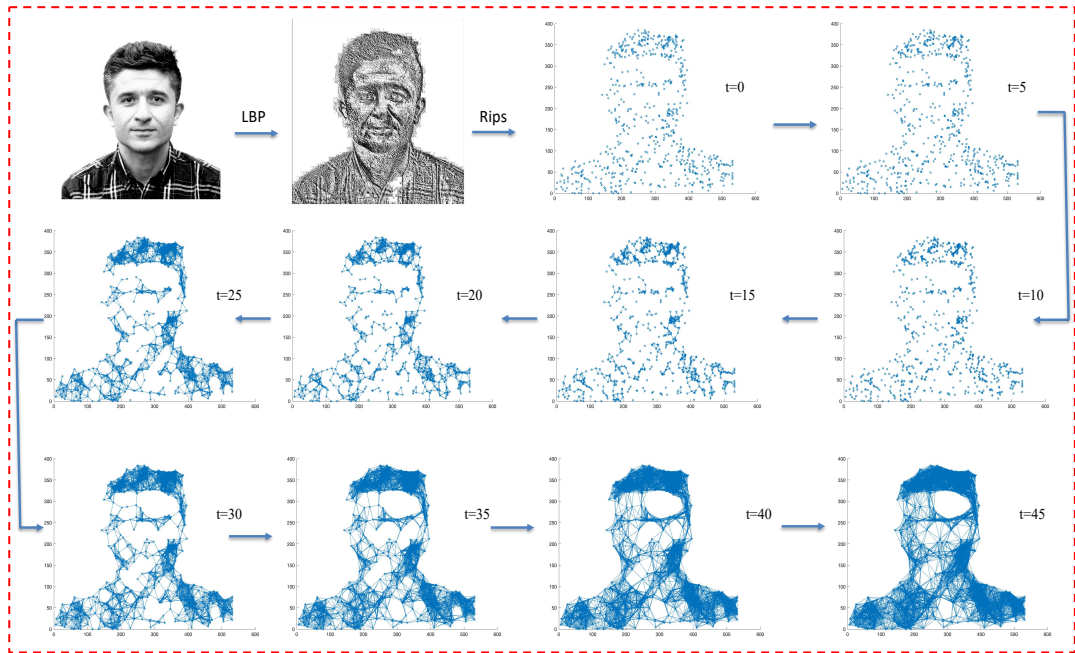
Figure 4-1: Rips complex construction procedure. We start by converting the Original Image (Top Left) into LBP domain (1st row, 2nd image).

From figure (4-1) different landmark pixel candidates from different groups of 2ULBP can be depicted in a similar approach. Depicted graphs in figure (4-1) are landmarks based on 1st rotation of 2ULBP landmarks. Increase the distance threshold t monotonically and construct Rips complexes for each t, and compute B_0 and B_1 at each t. Proceeding in this manner, not only we extract persistent topological features, we also obtain information about spatial distribution of landmark pixels that will help in providing insight into many image analysis tasks.

Topological features extracted from face images in this manner can also be extracted from persistent barcodes by discretizing the space of persistent barcodes. For each landmark selection criteria, compute the Euclidean distance matrix between the pixel landmarks and then input this matrix into any TDA software (in this thesis we used Ripser [29]) to produce persistent barcodes of dimension zero and one. Next, at each vertical line $t = 0, 1, 2, \dots, n$ compute the intersection points between the line t and the bars at dimension zero and one. This way, a topological feature vector will be obtained which has dimension of n. The value of n can be chosen according to the application domain and the type of landmarks one might select. We call this process ***persistent binning***. Figure 4-2 depicts the process of discretizing the space of persistent barcodes described above.
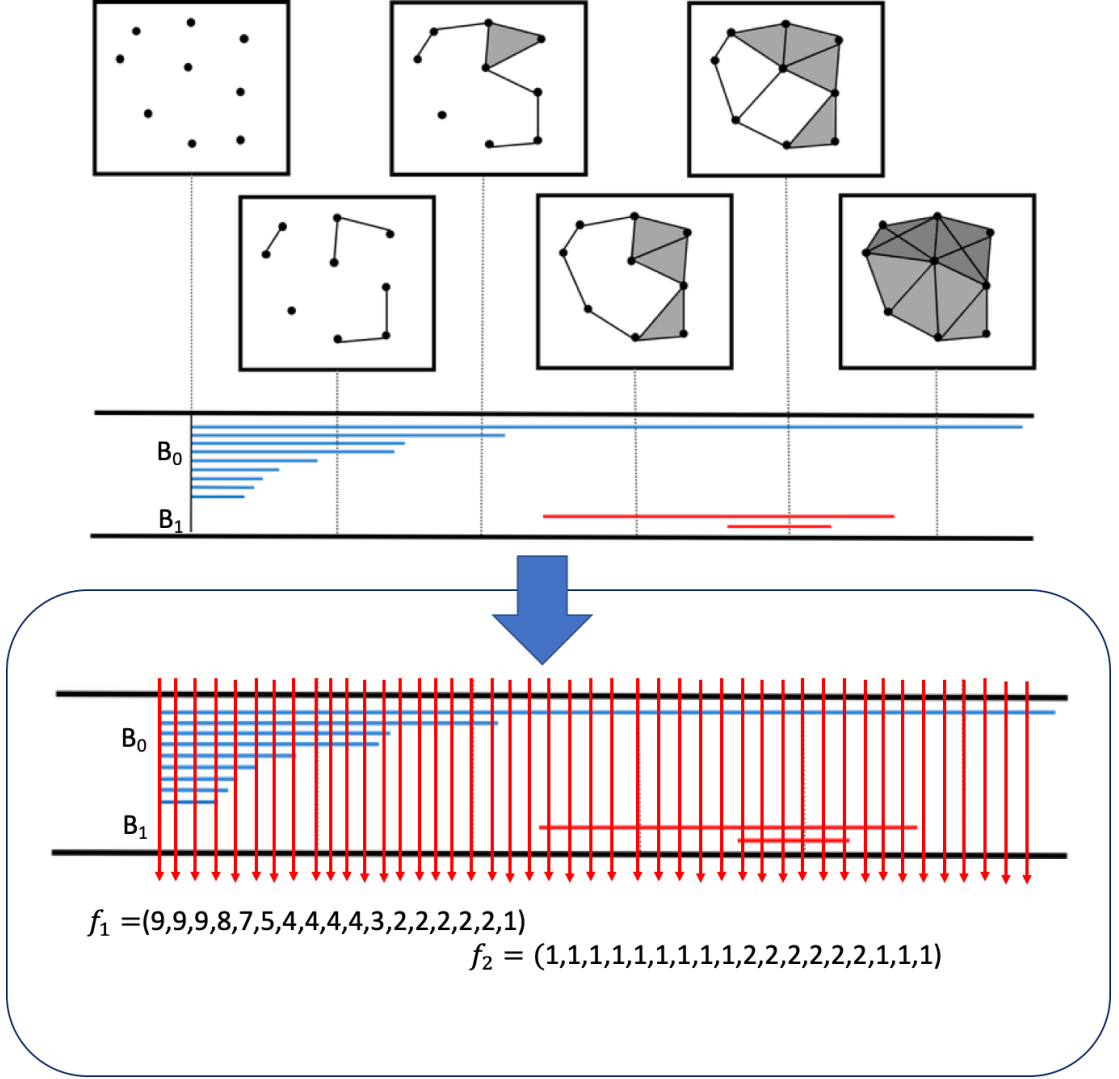
Figure 4-2: Persistent Barcode generation from a point cloud and Persistent Binning procedure. (Top) Persistent barcode constructed from a small set of point cloud [65]. (Bottom) Persistent binning in dimension zero and one

Throughout this thesis, persistent binning will be used to extract topological feature vectors from constructed persistent barcodes. This approach enables us to fuse topological features of different dimensions as well as fusing topological features extracted from different type of landmarks. There are many ways one can use the topological information obtained from persistent binning and different methods of landmark selection. **First scenario**: using the topological features at each binning step t_i, and then fusing it with topological features of different groups of the same landmarks at the same t_i. In this vein, if we consider the set G_2-ULBP for selecting landmarks from images, it has 8 rotations and hence at each t_i, we obtain an 8-dimensional topological feature vector as follow:

$$f_{(G2-ULBP)_{t_i}} = \big(B_0(R_1), B_0(R_2), \dots , B_0(R_8)\big) \tag{4.1}$$

$$f_{(G2-ULBP)_{t_i}} = \left(B_1(R_1), B_1(R_2), \dots , B_1(R_8)\right) \tag{4.2}$$

where B_0 and B_1 are betti numbers at dimension zero and one respectively, and R_j is the rotation of G_2-ULBP for $j = 1,2,\dots,8$.

The above equations can be used to train a Morphed-Vs-Genuine face images at each threshold separately. Although, it doesn't facilitate the study of persistence of homological features (i.e. Persistent homology) over a range of threshold. Instead, it facilitates the study of persistence of classification accuracy. **Second scenario**: to investigate the PH over a range of distance thresholds we need to train the classifier on the concatenation of the homological features of all binning steps of G_λ-ULBP into one feature vector as follow:

$$f_0(G_\lambda - ULBP) = \left(B_0(R_1)_{t_0,\dots,t_{100}}, B_0(R_2)_{t_0,\dots,t_{100}}, \dots , B_0(R_8)_{t_0,\dots,t_{100}}\right) \tag{4.3}$$

$$f_1(G_\lambda - ULBP) = \left(B_1(R_1)_{t_0,\dots,t_{100}}, B_1(R_2)_{t_0,\dots,t_{100}}, \dots , B_1(R_8)_{t_0,\dots,t_{100}}\right) \tag{4.4}$$

At each distance threshold, the dimension of the topological feature vectors defined by equations (4.1) & (4.2) is 8, whereas the dimension of topological feature vectors of equation (4.3) and (4.4) is 801.

In this chapter, we focus and discuss the use of the first scenario, i.e. topological features of the form of equation (4.1) and (4.2). In chapter five and the rest of the thesis, we cover the discussion about topological features of the form of equation (4.3) and equation (4.4).

To investigate the suitability of topological features extracted from face images in this manner, we start by manually cropping the frontal face of images, selecting landmarks which are pixel values that corresponds to G_2-ULBP and calculate the distance matrix between selected landmark-pixels and construct Rips complexes. An example of the resulting Rips complexes can be seen from figure (4-3). Next, we discuss the analysis of extracted connected components, which are topological invariants, for the purpose of morph detection.
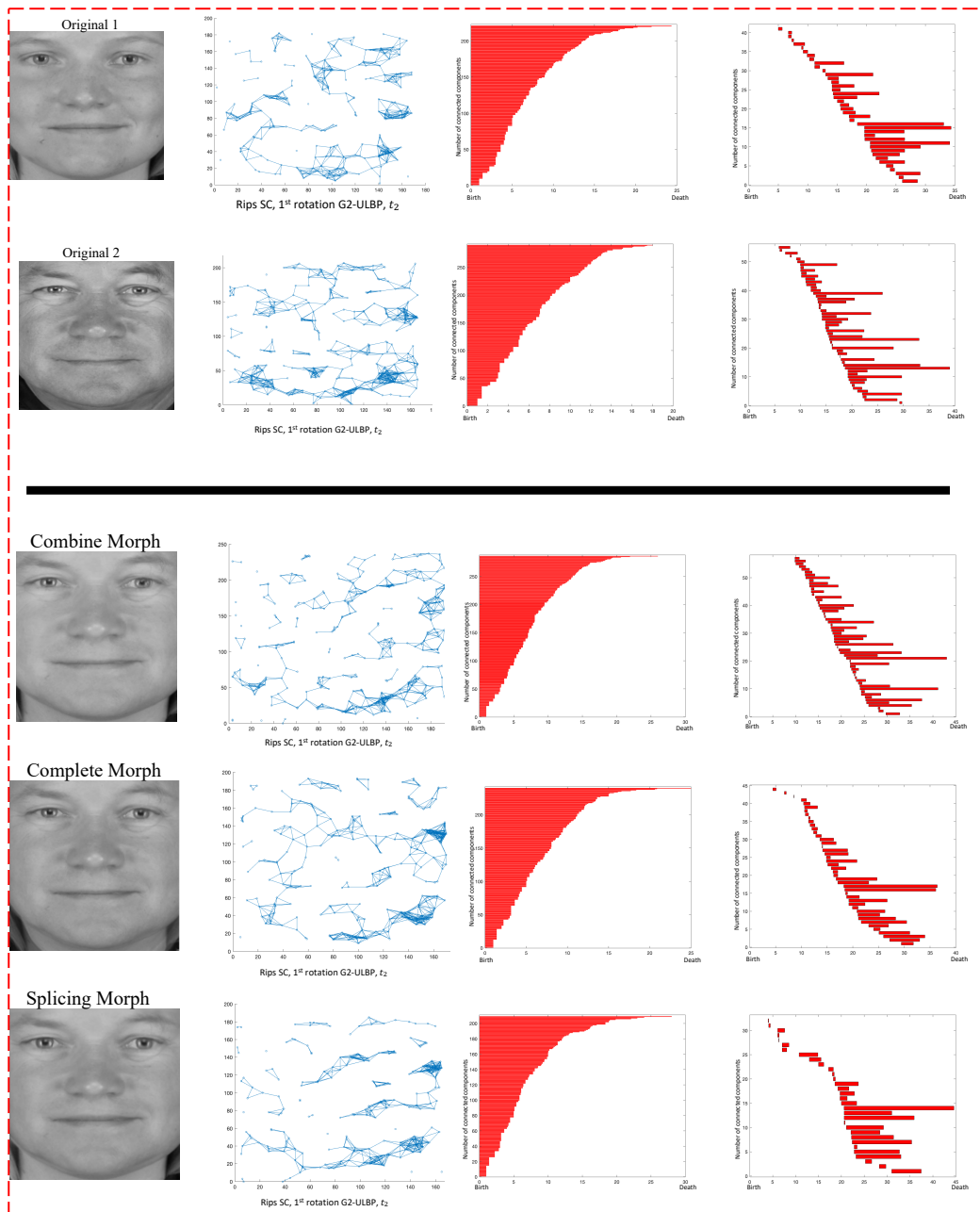
Figure 4-3: Sensitivity of Topological features to detect morphing. The Rips complex constructed from G_2-ULBP for source images and the morphed images (combined, complete and splicing) at t_2.

4.4 A Hypothesis for Homology-based Morph Detection

Ultimate face morphing detection algorithm would be based on a supervised machine learning approach which we train on topological invariants, at different dimensions and based from different landmark criteria, extracted from genuine and morphed images. It is worth to remember that for each input image, we have 8-sequences of topological invariants each representing one of the rotations of G_2-ULBP. As a proof of concept, we start by analysing the number of B_0 at t_2, i.e.

number of connected components at the second threshold, rather than looking at the entire sequence of Rips complexes. This will allow us to build a simple similarity function and a naive classifier for each of the 8 rotation and then use majority rule at the testing stage. The simple classifier is based on the distributions of the B_0 values for a training set of original and morphed images. We trained and tested performance of the classifier(s) using morphed images from the Utrecht face photo database [100]. The training was based on, 28 images (14 original and 14 morphed) for each morphing schemes, and calculated the averages and standard deviations of the B_0 values in each class for each of the 8 rotations of the uniform 2-ones LBP point set. In other words, the topological feature vector has the following form:

$$f_{(G_2-ULBP)_{t_2}} = \big(B_0(R_1), B_0(R_2), \dots, B_0(R_8)\big).$$

The statistics obtained from the 28 images, described earlier, are summarized in table (4-1).

LBP Code	Original		Splicing Morphed		Combined Morph		Complete Morph	
	Mean	Std	Mean	Std	Mean	Std	Mean	Std
00000011	16.23	14.19	60.13	13.33	66.83	5.91	31.58	8.94
00000110	20.31	14.62	57.73	14.47	61.83	6.48	36.83	10.58
00001100	21.92	16.63	64.27	13.07	68	4.67	38.75	8.87
00011000	22.31	13.18	65.87	12.68	69	7.32	41.08	8.66
00110000	24	15.80	60.4	10.50	69.58	4.50	37.92	11.60
01100000	22.86	17.90	60.6	11.91	73.58	7.43	37.08	9.01
11000000	18.66	13.97	61.8	10.77	64.42	6.84	35.58	5.93
10000001	22.46	16.87	62.67	11.62	69.42	6.39	38.08	10

Table 4-1: Topological (connected components) feature statistics of 28 images (14 original and 14 morphed) for G_2-ULBP codes at t_2. Std refers to standard deviation.

Results summarized in table (4-1) show that across all rotations of G_2-ULBP, the average number of B_0 values for the genuine images are well below those calculated for the morphed images. Taking into account the corresponding standard deviations, we see that the best separation gap is achieved by the combined morphing scheme followed by those achieved by the splicing morphing, and the complete morphing resulted in significantly lower gaps. The positions of the considered texture features of G_2-ULBP pixels in human face images do not vary significantly, for a proof of concept it is reasonable to suppose that the $f_{(G_2-ULBP)_{t_2}}$ values have a gaussian distributed. Next chapter will include more sophisticated statistical measures and machine learning approaches together with a larger number of images to investigate the problem of morph detection.

The above assumption, although not completely necessary, allows us to use known facts about gaussian distribution statistics to determine with good accuracy the probability that an input image belongs to either class (genuine or morphed). In fact, for each rotation to classify an input image we simply need to find the position of its B_0 value in relation to the overlap regions between the two distributions as depicted in figure (4-4). In this vein, to classify a test image, all eight rotations of G_2-ULBP will be used where we use a majority voting to make final decision about the class of the input image. If the result of rotation voting about the class of the image is draw of 4, then it is an undecided case.

Above hypothesis tested on 338 images from Utrecht face database, 38 genuine face images, 100 splicing morph, 100 complete morph and 100 combined morphed images. Face morphed images in this thesis have been generated by AMSL group at Magdeburg university [95]. The features extracted from testing images followed the same process of that of training images.
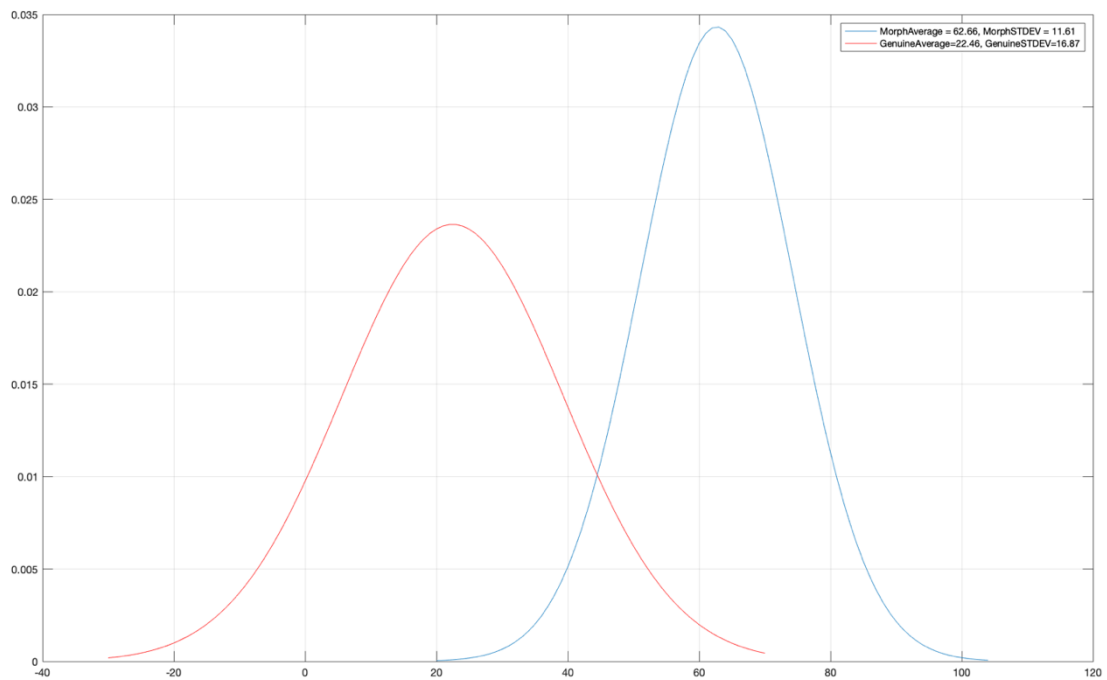
Figure 4-4: Gaussian Distribution of B_0 values of training face (genuine (Red) and morphed(Blue)) images at 8th rotation of G_2-ULBP.

In other words, for each rotation of G_2-ULBP, we calculate the number of B_0 at the second threshold. The results for the testing images were as follows:

- In the case of combined morphed approach, proposed scheme obtained 99% accuracy and the misclassified images were morphed images.

- For splicing morphed images, we obtained 98% accuracy and the misclassified images were original images.

- Finally, in the case of complete morphed approach, 60% accuracy achieved whereby most of the misclassified images were morphed images. The main reason behind this is the fact that complete morph faces are inheriting geometry from both source images and that seems to have an effect on the topological features used here for the classification.

As a first experiment towards building a sophisticated morph detection algorithm based on TDA, these testing results demonstrated the viability of using persistent homology approach to automatically detect morphing attacks.

Next section will include the first attempt in using a machine learning classifier where the input is a topological feature vector which is in the form of equation (4.1) and (4.2).

4.5 Classification of Morphed Face Images

In this section, we present the experimental results obtained using the K-nearest neighbour classifier [129], with k=1. The KNN is a non-parametric, instance based, simple yet robust supervised classifier that uses proximity to template feature vectors (our PH-based vectors) of class labelled set of training stage.

4.5.1 Experimental Setup

The experiments, conducted in this section, use on a sufficiently large set of face genuine and morphed images selected from the Utrecht face database, using 75 genuine non-smiling faces, we created 6560 morphed faces using the three morphing schemes discussed in chapter 3, known as Complete, Splicing and Combined Morphing. In particular, we generated and used 1298 complete, 2612 splicing and 2650 combined morphed face images to test our proposed morph detection technique. Unlike section 4.2, instead of manually cropping out the frontal face region from the face images, we use *dlib* library version 19.2 (http://dlib.net/) to segment the frontal face regions. Similar to the Bayesian approach discussed in the previous section, this experiment is restricted to G_2-ULBP codes only. The choice of subsequent thresholds

to construct Rips complexes can be determined by dividing the range of D-values, but we used a fixed resolution of thresholds ($t_1 = 0, t_2 = 3, t_3 = 5, t_4 = 7, t_5 = 10, t_6 = 15$). This choice is not completely random, we observed the change in the number of B_0 (e.g. there is no big change in the number of B_0 from $t = 0$ to $t = 1$, $t = 3$ to $t = 5$ and so on), thus we opted to select this pattern of thresholds. Nonetheless, the choice of threshold selection is application dependent and can be tuned/selected accordingly. Beyond certain thresholds, constructed Rips complex gets closer to become a complete graph which means the topological invariant like the one we use here become less discriminative to distinguish morphed face images from their genuine counter-parts.

The training/testing pipeline of our morph detection scheme is depicted in figure (4-5). For evaluation, we use the four different classification protocols, below:

- P1: Leave-one-out, where one image is used for testing the rest for training.
- P2: 30% of the images used for training, and the rest of the 70% for testing.
- P3: 50% of the images used for training and the rest of the 50% for testing.
- P4: 70% of the images selected for training and other 30% for testing.
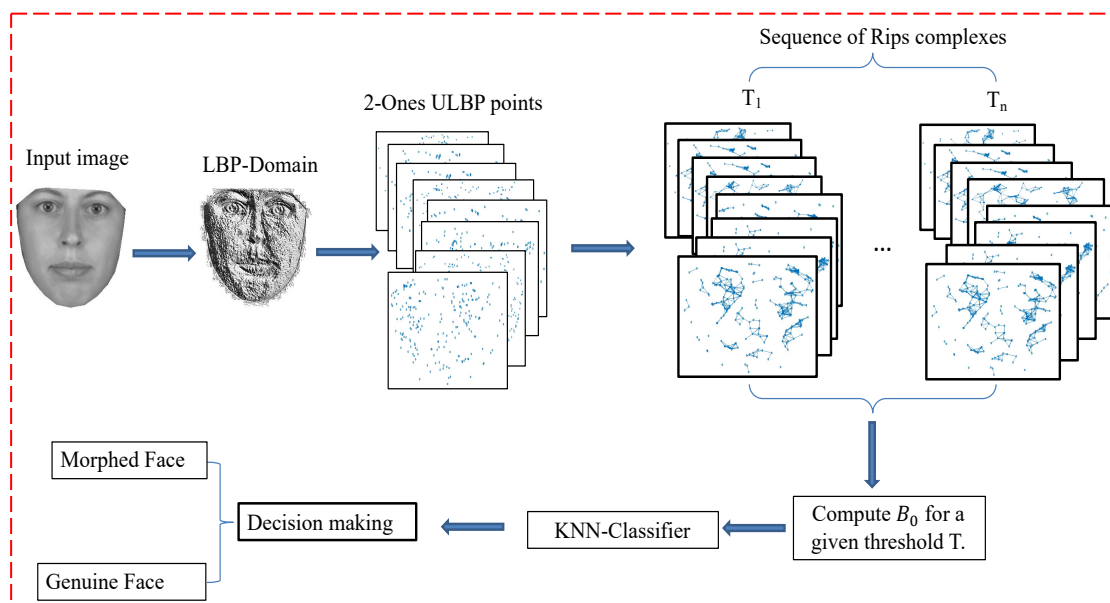
Figure 4-5: Topological Morph detector pipeline.

To avoid biasness, each performance evaluation experiment is repeated 100 times by select random disjoint set of images for training and testing and calculating the average accuracy over the 100 experiments.

4.5.2 Experimental Results

In this section we report the classification accuracy of experiments conducted for the purpose of morphed face detection, following the detailed setup in the previous section. Below in table (4-2), we summarize the average classification accuracy for each protocol and for each topological threshold. The table clearly demonstrates significant sensitivity of topological features, namely B_0, to detect morphed face images created by the three morphing schemes discussed in chapter 3, section (3.4), over a range of thresholds. It is obvious from the table that the accuracy of the classification is independent of training protocols. The ratio of false negative rates, i.e. morphed faces misclassified as genuine images, is 0.25% across distance thresholds while false positive rates, i.e. genuine faces misclassified as morphed, are quite high ($\approx$17%). This could be partially due to the imbalanced training of the classifier which include a larger number of morphed faces than genuine face images.

We also conducted an experiment to test the performance of proposed technique to detect P&S morphed face images. The P&S test included 140 images, 70 genuine faces and 70 P&S splicing-morphed faces. The images scanned using CanoScan model 9000F MarkII by our collaborators from Advanced Multimedia and Security Lab (AMSL) at Otto-von-Guericke-University of Magdeburg, in Germany.

Morphing Schemes	Protocols	Topological Distance Thresholds					
		$t=0$	$t=3$	$t=5$	$t=7$	$t=10$	$t=15$
Combine Morph	P1	99	99	97	95	98	99
	P2	99	98	97	95	98	99
	P3	99	98	97	95	98	99
	P4	99	98	97	95	98	99
Splicing Morph	P1	97	97	96	100	94	97
	P2	99	97	96	99	94	97
	P3	97	97	96	99	94	97
	P4	97	97	96	99	94	97
Complete Morph	P1	96	96	95	95	92	93
	P2	96	96	95	94	92	93
	P3	96	96	95	94	92	93
	P4	96	96	95	94	92	93

Table 4-2: KNN classification accuracy of PH-threshold based Morph Detection.

Images were in different resolution ranging from 121x136 to 2017x2517, and hence we rescaled them into 220x270 and then extracted G_2-ULBP landmarks. The rest of the experiment followed the setup in section (4.5.1).

The results in table (4-2) might raise doubts about achieving such results for larger datasets or on a different dataset. We addressed both of these concerns by first extending our experiment in the next chapter to include another dataset. Secondly, to show that the results obtained here is not a case chance, we conducted a test on 10,000 natural images from BOSSBase database (http://dde.binghamton.edu/download/) to test the sensitivity of ULBP landmarks to small changes as a result of tampering. For each image, we calculated the number of pixels that are different from its immediate surrounding pixels by a factor of ±1. This is done to estimate the chance of ULBP landmarks changing their structures into non-ULBP landmarks. The result of the experiment revealed that, on average more than 78% of the pixel values in those 10,000 natural images have a ±1 differences from their immediate neighbours and hence one expect that to obtain a reasonable number of changes to the number of ULBP landmarks as a result of tampering/morphing.

	t=0	t=3	t=5	t=7	t=10	t=15
P1	78.87	77.46	73.94	77.46	82.39	72.53
P2	75.64	74.72	74.77	77.1	79.33	70.13
P3	77.97	76.14	74.81	78.28	80.11	72.65
P4	78.57	77	74.76	78.59	81.40	72.38

Table 4-3: Classification accuracy of P&S morphed face detection

Results in table (4-3) indicate that the performance of the PH-based scheme with the P&S morph attack is well below that achieved with the digital morphing attacks. Nevertheless, it is still encouraging and sufficient to demonstrate the success of TDA approach to designing morph detection algorithms. In [122], the authors proposed a P&S morph detection technique based on two Deep-CNN architectures, AlexNet and VGG19, where they concatenated the features from both architectures before classification stage and the best classification accuracy they obtained is 82.36% accuracy when they used HP scanner and 87% accuracy for RICOH scanner. At this stage a direct comparison with the approach proposed in [122] is not possible because they used different in-house databases.

The main differences between images obtained with P&S attack and those produced by the digital attacks is the significant variation in image resolution within the generated images, and when rescaling process is applied there would be some loss of information influencing the spatial distribution of the landmarks in the resulting images. A potential approach to improve these detection results could benefit from using fixed size images or applying some form of super-resolution algorithms instead of rescaling.

In summary, main advantages of the proposed approach are (1) no prior information about the image nor the morphing technique is needed, (2) the landmarks are automatically selected to build topology of face images and (3) the classification performance is almost topological-threshold independent, especially in the case of digital images. Perhaps the only drawback of the proposed morph detection technique is that one cannot rely/determine a unique threshold to obtain high classification accuracy for different morphing schemes or a threshold where we get high accuracy for digital and P&S images.

Having demonstrated the success of homology-based analysis of the spatial distribution of image texture landmarks for face morph attack detection, the rest of the thesis will be concerned with persistent homology approach over a range of distance thresholds. Next chapter will include an extension of the algorithm of this chapter by removing reliance on any specific threshold, i.e. the classification will not depend of the number of connected components (and 1-dimensioanl holes/loops) extracted at each distance threshold. Instead, topological features over a sequence of distance thresholds will be stored to feed into KNN and hence overcome the drawback of the proposed technique discussed in this chapter.

Chapter 5

PH-Based Image Analysis for Face Morph Detection

In the last chapter, we established that the homology parameters of Rips SCs constructed for sets of image texture landmarks are effective in distinguishing morphed face images from genuine ones with considerably high accuracy at different distance thresholds. Instead of aiming to establish the best application-based threshold, the well-established TDA strategy of investigating the persistence of the homology parameters across increasing sequences of thresholds is most promising. Accordingly, this chapter is devoted to continuing the journey and develop a PH-based image analysis technique, and demonstrate its success for face morph detection. In the next chapter we shall further demonstrate that this approach works well for many other types of image analysis tasks. We shall also demonstrate, that the success of this approach is not confined to the LBP based landmarks but there are ample groups of automatically extractible image landmarks that could be used for PH-based image analysis

5.1 PH of Image Texture Landmark Clouds

In chapter 4, the main ingredient of this scheme was introduced in (equations 4.3 and 4.4). In order to make this chapter self-content, we shall briefly describe the construction of the application-dependent discriminating PH-based feature vectors that will be used to model the intended classification scheme. In what follows, we shall only consider grayscale automatically cropped frontal face images, where dlib library used and called from MATLAB. We assume that an application-dependent set $P = \{p_1(x_1, y_1), p_2(x_2, y_2), \dots, p_n(x_n, y_n)\}$, of specific texture-based landmark pixels (to be referred to as a Landmark Cloud) are extracted automatically. This could be any of the Landmark Clouds introduced in the next section, including the various ULBP geometry groups. As explained earlier, the Rips complexes, associated with P, will be constructed by first computing the nxn symmetric matrix $D = (d_{i,j})$, of

pairwise distances between points in P. Computing the ith-dimensional PH record of P Betti-numbers B_i requires the selection an appropriate sequence of distance thresholds: $T = \{t_0 = 0, t_1, t_2, \ldots, t_k\}$. In chapter 4, we subdivided the interval $[T_{min}, T_{max}]$ using equidistant thresholds to determine the Betti numbers at each threshold and classify accordingly. Recognising that computing PH record is based on a filtration of an "ultimate" simplicial complex of P which may not be determined by T_{max}. For example, in many cases the Rips complex may be fully connected well before reaching the T_{max} threshold. Moreover, even if two image landmark clouds have the same, or nearly the same, cardinality, they may become fully connected at different thresholds or have different number of topological invariants at different constructed SCs based on the increased sequence of distance thresholds (e.g. $t_1 < t_2 < t_3 < t_4$), this is illustrated by the following figure.
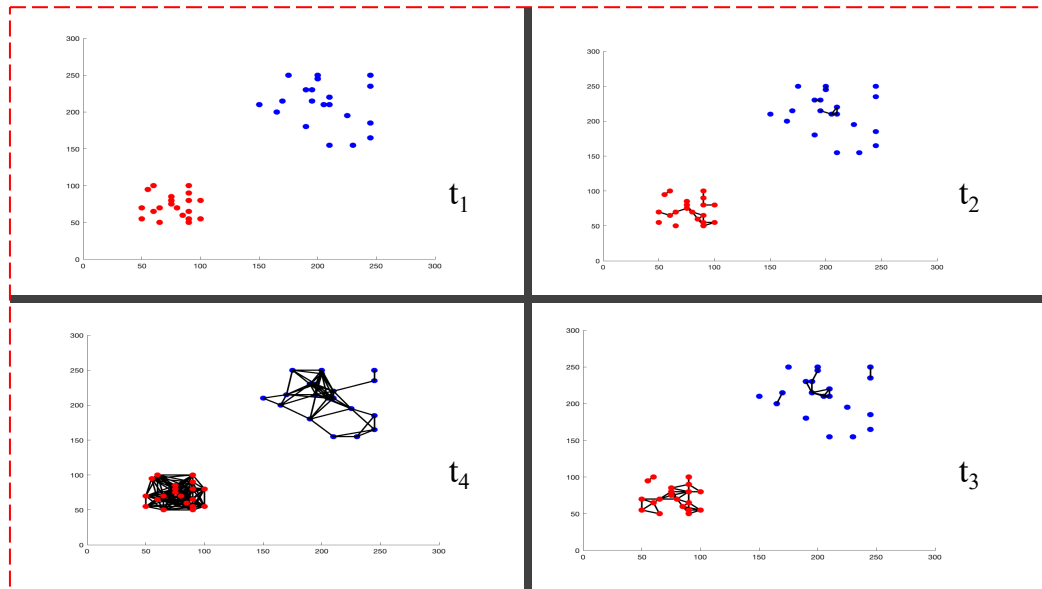
Figure 5-1: Two cluster points (Red and Blue) with similar cardinality, but different in spatial distribution.

These considerations imply that the appropriate threshold sequence selection yields a time-series representation of the PH record of different lengths whose entries are not necessarily measured at equidistance thresholds. Comparing such time series adds the complexity of the corresponding image analysis task. Using Dynamic Time Warping, in this case, become unavoidable necessity. What complicates the situation further, is that threshold sequence selection depends on the dimension of the Betti numbers. Stopping at the threshold that results in one connected component does not means that the number of holes stops changing thereafter.

For simplicity and computational efficiency, we fix $k = 100,$ and select an increasing sequence of 100-equidistance thresholds $T = \{t_1, t_2, \dots, t_k\}$. Iteratively, we construct a sequence $\{\mathbb{S}_{t_i} : i = 1, 2, \dots, 100\}$ of Rips complexes by joining pairs of landmarks p and q iff:

$$T_{i-1} < d(p, q) \leq T_i \quad for \ i = \{2, 3, \dots, 100\}.$$

This results in a *filtration* of the final simplicial complex $\mathbb{S}_{t_{100}}$ with $\mathbb{S}_{t_1} = P$. Finally, compute the 0-Betti (and 1-Betti) numbers of the sequence $\{\mathbb{S}_{t_i} : i = 1, 2, \dots, 100\}$ of Rips complexes using the Smith normal form procedure described in chapter 2. The output of this process is the sequence of 0-betti numbers (i.e. connected components):

$$\left(B_0(\mathbb{S}_{t_1}), B_0(\mathbb{S}_{t_1}), B_0(\mathbb{S}_{t_2}), \dots, B_0(\mathbb{S}_{t_{100}}) \right) \tag{5.1}$$

and the sequence of 1-Betti numbers (i.e. holes)

$$\left(B_1(\mathbb{S}_{t_1}), B_1(\mathbb{S}_{t_2}), B_1(\mathbb{S}_{t_3}), \dots, B_1(\mathbb{S}_{t_{100}}) \right) \tag{5.2}.$$

These equations represent 100-dimensional PH feature vectors for a single landmark set, such as any one of the 8 single rotational subsets of a G_λ-ULBP, $\lambda = 1, 2, \dots, 7$.

5.2 Landmark Selection Methods

In the last two chapters, we investigated topological approaches to the detection of tinny and invisible image distortions caused by malicious face image morphing attacks by analysing the simplicial complexes of the shape formed by clouds of ULBP landmarks. However, one expects that face image morphing attacks distort a variety of other types of textural and/or structural primitives in the face image region. In this section, we introduce few other meaningful, and easy to extract automatically, landmarks of image texture primitives. In fact, this section illustrates that all types of images contain a rich source of landmarks whose spatial distribution can provide a meaningful topological representation of images.

5.2.1 Local Binary Patterns - Revisited

More than two decades ago, the LBP transform was used as a texture descriptor for images that can be used to distinguish images for classification application such as face recognition. It re-encodes an image by an 8-bit Byte whose bit cells are

determined by the order relationship between the pixel value and that of each of its 8-neighbouring pixels starting from top left corner in a clockwise manner. The output can be displayed as a grayscale image called the *LBP transformed image* whose histogram have been used in many image analysis/classification applications. In figure (5-4), we illustrate a local binary pattern of an image, and 3 other approaches of landmark selection methods which will be discussed hereafter.

Uniform LBP (ULBP) codes are LBP codes that have either 0 or 2 circular bitwise transition from 0 to 1. In [130], the authors shown that in face images 90% of LBP codes are uniform. This is a strong justification that we select subsets of ULBPs for our choice of TDA construction landmarks. In total, there are 58 ULBP codes two of which have 0 transition namely 00000000 and 11111111. The remaining 56 ULBPs have 2 transitions and we refer to this set as the 2ULBP. The 2ULBPs consist of 7 groups of LBPs, called G_λ-geometries for $\lambda=1,\ldots,7$. Here, λ refers to the number of 1's in its binary representation. Each G_λ consists of 8 LBP codes that can be obtained from each other by a circular rotation. The set of 2ULBP image pixel positions forms a very large source of image landmarks that are sensitive to pixel value changes. For efficiency purposes, we use each and every rotation in each G_λ group as a separate landmark set and for the intended PH morph detector, we shall build in parallel a separate nested simplicial complex for the eight rotations in G_λ and create one feature vector representing their PH parameters.

Instead of designing a decision-based fusion of these 8-rotational detectors, our intended PH-based face morphing detector will be based on feature level fusion. Accordingly, we construct the simplicial complexes of 8 rotations of the G_λ-ULBP cloud over a fixed 100 distance thresholds, and train the classifier on the concatenation of the homological features of all binning steps as the single feature vectors defined by the following 2 expressions:

$$f_0(G_\lambda - ULBP) = \left(B_0(R_1)_{t_1,\ldots,t_{100}}, B_0(R_2)_{t_1,\ldots,t_{100}}, \ldots, B_0(R_8)_{t_1,\ldots,t_{100}}\right) \qquad (5.3)$$

$$f_1(G_\lambda - ULBP) = \left(B_1(R_1)_{t_1,\ldots,t_{100}}, B_1(R_2)_{t_1,\ldots,t_{100}}, \ldots, B_1(R_8)_{t_1,\ldots,t_{100}}\right) \qquad (5.4)$$

According to equations (5.3) and (5.4), the shapes of the different 8 rotational Landmarks in the G_λ-ULBP are represented in the morph detector by 800-dimensional PH feature vectors.

5.2.2 8-Neighbour Superpixels (8NSP)

In the image analysis literature, a super-pixel in an image is a connected set of pixels that have the same grayscale intensity value [131], and are used for local image over-segmentation and later used in object detection and image reconstruction [132]. We slightly modify this concept to introduce an alternative set of image pixel landmarks that disregards the order relationship between a pixel and its neighbouring pixels and instead focus on the relationship between the intensity values in the boundary pixels. The easiest relationship between the neighbouring pixel is that of "=". When all these pixels have equal values, then the central pixel has an 8-neighbour super-pixel (8-NSP). It is easy to see that the set of all 8-NSP pixels is a proper subset of the set of 0-transition ULBPs. The 8-SNP pixels are LBP encoded to 00000000, if the central pixel value < that of the neighbours, else are LBP encoded to 11111111.

One can split the set of 8-NSP pixels naturally into different sets of landmarks by subdividing either the range of their central pixel values, or the range of neighbouring values. However, we shall treat this set as a single landmark, and accordingly their PH feature vectors are of the forms defined by equation (5.1) and (5.2).

5.2.3 Centre-Symmetric Local Binary Patterns (CS-LBP)

A modified version of LBP operator is the centre-symmetric LBP (CS-LBP) proposed in [133] to capture regions of interest in digital images. Unlike LBP, neighbouring pixels are not compared with that of the central pixel, instead, we compare the neighbouring pixels in a centre-symmetric manner, as depicted in figure (5-3). In other words, in CS-LBP and for a 3-by-3 image patch, we compare the pixel in top-left corner with bottom right, top-middle with bottom-middle, top-right with bottom-left pixels and middle-right with middle-left. In LBP, one obtains 256 distinct binary patterns, 58 of which are uniform, whereas CS-LBP produces 16 unique binary patterns only which can be described through the following equation:

$$CS - LBP(x, y) = \sum_{i=0}^{\left(\frac{N}{2}\right)-1} s\left(p_i - p_{i+\left(\frac{N}{2}\right)}\right) 2^i, \qquad s(x) = \begin{cases} 1 & if\ x \geq 0 \\ 0 & otherwise \end{cases} \qquad (5.5)$$

where p_i and $p_{i+\left(\frac{N}{2}\right)}$ are pixel intensity values of center-symmetric pairs of pixels of N equally spaced pixels. The 16 distinct binary patterns of CS-LBP operator can be grouped according to the number of ones in their binary codes (similar to ULBP) and

the circular transitions between zeros and ones, as depicted in figure (5-2). Although, to the best of our knowledge, no explicit grouping introduced in the literature to identify uniform and non-uniform groups of CS-LBP codes. Hence, we follow the same procedure of original LBP to group uniform binary codes according to the transitions between zeros and ones in the binary codes. In other words, when there is either zero or two circular transitions between zeros and ones in the CS-LBP codes, we label this binary code as uniform, otherwise it is a non-uniform code. Therefore, we end up with 14 uniform CS-LBP codes, and only 2 non-uniform codes where we group the uniform codes into 3 groups (each with 4 rotations) G_1, G_2 and G_3 such that 1,2 and 3 refer the number of ones in the binary codes. Generated topological features from CS-LBP is concatenated similar to the approach introduced in equation (5.3) and (5.4), except that here we have 4 rotations instead of 8. In other words, the topological feature vectors in CS-LBP have the following form:

$$f_0(G_\lambda - CSLBP) = \left(B_0(R_1)_{t_1,\dots,t_{100}}, \dots, B_0(R_4)_{t_1,\dots,t_{100}}\right) \tag{5.6}$$

$$f_1(G_\lambda - CSLBP) = \left(B_1(R_1)_{t_1,\dots,t_{100}}, \dots, B_1(R_4)_{t_1,\dots,t_{100}}\right) \tag{5.7}$$

Where f_0 and f_1 represent topological features in dimension zero and one, respectively. B_0 and B_1 are betti numbers of dimension zero and one, respectively, which correspond to the number of connected components and loops, respectively. Finally, R_i is rotations of binary codes of the same group where $i = 1,2,3,4$.

5.2.4 Radial Local Binary Patterns (R-LBP)

We propose another extension to original LBP which we called radial LBP. Like LBP and CS-LBP, R-LBP starts by selecting 3x3 patches in an image and then comparing the central pixel to that of the 8-neighbouring pixels in a radial manner. Instead of 256 distinct binary patterns, in R-LBP we obtain 16 unique binary patterns. The process starts by selecting 3x3 patches from the image of interest, and then comparing the central pixel with its 8 neighbours by the following equation:

$$R - LBP(x,y) = \sum_{i=0}^{\left(\frac{N}{2}\right)-1} \left(s_1(p_i - p_c) \times s_2\left(p_{i+\left(\frac{N}{2}\right)} - p_c\right)\right) 2^i \tag{5.8}$$
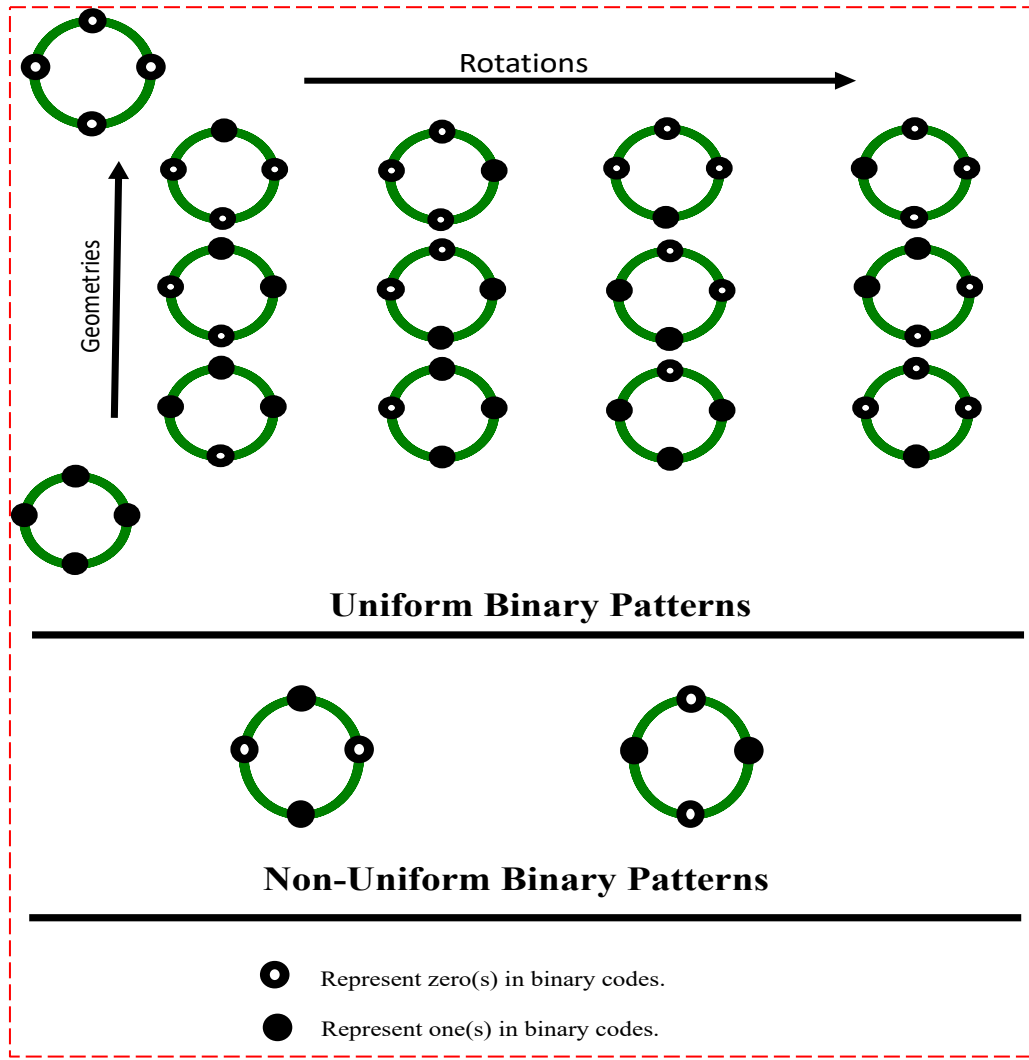
Figure 5-2: Geometry of uniform CS-LBP & R-LBP codes arranged according to the number of 1's in their binary representation.

where p_c is the central pixel, p_i is neighbouring pixel(s) and the function s_l is defined as follow:

$$s_l(x) = \begin{cases} 1 & if\ x \geq 0 \\ 0 & otherwise \end{cases} \quad for\ l = 1,2 \tag{5.9}$$

Each pixel in the resulting R-LBP image is encoded as a byte determined by the 4 s-bits in a counterclockwise order starting from the top-left corner. We group the binary codes of R-LBP according to the number of 1's and 0's in the binary representation and we focus on the groups where there is either 0 or 2 circular transitions, which we call uniform R-LBP. Topological feature generation using R-LBP follows the same approach as discussed in CS-LBP because in both of them we have the same number of binary codes and uniform/non-uniform codes, i.e. it has the same form as equation (5.6) and (5.7) for dimension zero and one of topological invariants. Note that,

84

computing this landmark is fast and automatic which makes it suitable to be considered for building topology of a digital image. Similar to other landmark selection techniques, R-LBP will be used to select image landmark pixels in order to construct Rips complexes and consequently computing persistent barcodes in different dimensions to design forensic tools for morphing/tampering detection purposes. The Figure below, illustrate, the way we can compute the decimal representation of the central pixel for LBP, CS-LBP and the R-LBP landmarks.
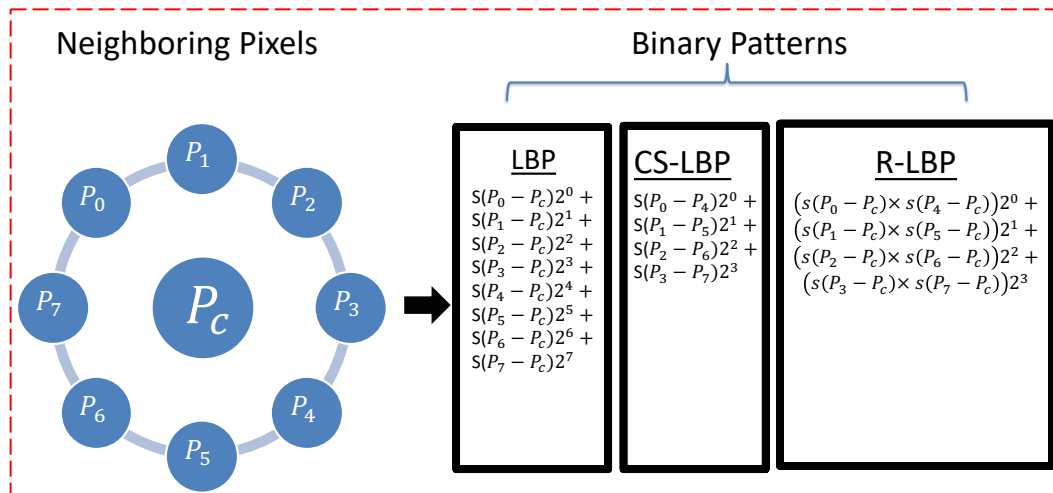
Figure 5-3: LBP, CS-LBP and R-LBP landmark selection methods for 8-neighbouring pixel values. P_c is the central pixel and $P_{0, 1, \ldots, 7}$ represent 8 neighboring pixels.
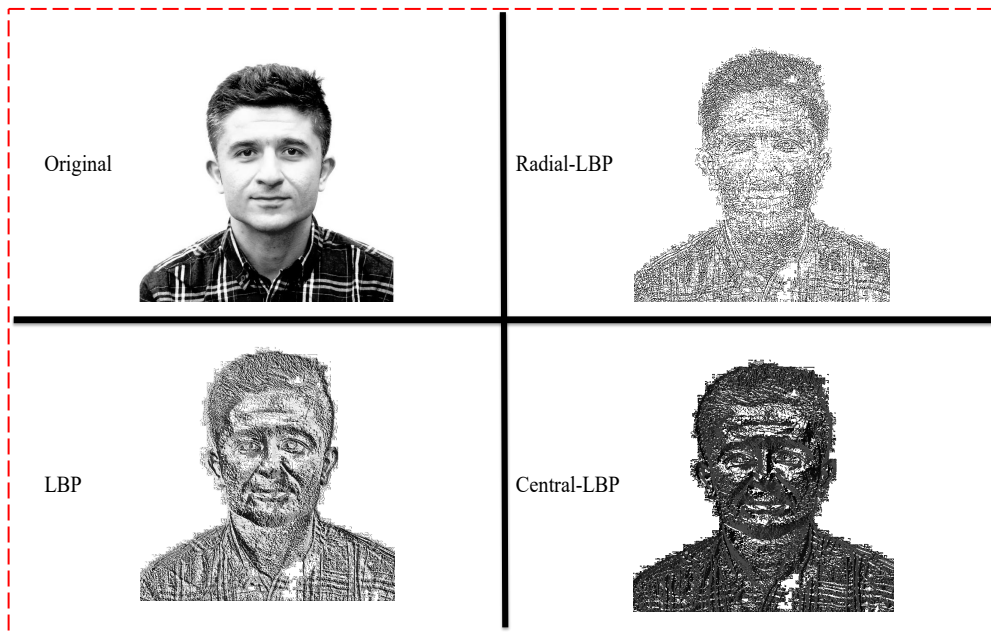
Figure 5-4: Landmark Selection methods and their corresponding facial effect visualization.

5.3 Experimental Setup

In order to evaluate the performance of the above PH-based morph detector, we extract the PH-feature vectors from the cropped face images in a set of sufficiently large balanced mix of genuine and morphed images and feed into an appropriate classifier, in a supervised mode. As in chapter 4, the evaluation is conducted separately for each of the 3 morphing algorithms, described in chapter 3, section 3.4.1: Combined morph (CombineM), Complete morph (CompleteM) and Splicing morph (SplicingM). The various experiments test the performance of the PH-based morph detector on two large datasets of hundreds of genuine and thousands of morphed faces formed by the 3 morphing techniques, described in Chapter 3. We also conducted similar experiments with a dataset of Print and Scan (P&S) faces photos.

5.3.1 Face Image Databases

The First dataset is Utrecht DB that contain 75 genuine images whereby 2652 CombineM, 1112 CompleteM and 1000 SplicingM faces created using pairs of the genuine images. Second dataset is the London DB [134] which contain 102 genuine (non-smiling) faces and 1500 CombineM, 1000 CompleteM and 1000 SplicingM morphed images created form pairs of genuine images.

The P&S face image dataset, a dataset of 142 print-scanned (P&S) images used for testing the discriminating power of the proposed PH-based morph detector where 71 face images are genuine and the other 71 were splicing morphed images printed and then scanned with CanoScan model 9000F MarkII. All face images are segmented, such that only the frontal face region used to extract the landmarks, using dlib library version 19.2 (http://dlib.net/). PH calculation conducted using Ripser software package, publicly available in (https://github.com/Ripser/ripser).

In what follows: UcombineM, UcompleteM, and UsplicingM, refers to Utrecht combined, Utrecht complete, and Utrecht splicing morphed images, respectively. Similarly: LcombineM, LcompleteM, and LsplicingM refers to London combine, London complete, and London splicing morphed images, respectively.

Finally, for each of the databases, we adopt the three different training-testing scenarios (DTS) (30%, 50% and 70%) of the images in the dataset will be used, separately, for training the NN classifier, and the remaining images in the database

are used for testing the performance of PH-detector for all landmarks. These experiments are repeated 100 times and average performance rates, computed according to next section criteria, will be reported.

5.3.2 Performance Measurements

The classification performance of the various schemes will be determined in terms of the false negative rate (FNR), false positive rate (FPR), and the accuracy (Acc) rate. Here, 'positive' refers to the morph class and 'negative' refers to genuine class, i.e. FNR represents the rate of morphed face images classified as genuine and FPR represent the rate of genuine face images classified as morphed. The Acc is the average of true positive rate (TPR) and true negative rate (TNR). The classification experiments are conducted in such a way that a balanced set of images from genuine and morphed images used for training and testing. Because the number of genuine images is much less than morphed ones, repeatedly different sets of images selected from morphed images to be evaluated with genuine ones and then calculate the average classification performance.

5.4 Results and Evaluations for ULBP and 8NSP Landmarks.

We start by reporting the performance of the number of connected components, i.e. B_0, computed from Rips complexes of different landmarks. The **first** set of experiments was aimed to determine the performance of PH-based detector build on 8-NSP landmark and 2ULBP. The results are shown in Table (5-1), Table (5-2), Table (5-3) and Table (5-4), respectively. The results in Table (5-1), show that the 8-NSP based detector performs significantly high when tested on the Utrecht DB and the P&S image dataset, but not so well when tested on the London DB where at best, the accuracy of around 85% is achieved when 70% training/testing protocol is adopted. Except for the London DB, there is little or no effect of changing the training protocols. For the London DB, notable increases in accuracy is achieved when the percentage of training increased for all the three morphing attacks. The FNR and FPR rates for LcombineM and LcompleteM are somewhat disappointing but are comparable. In Table (5-2), the performance of the proposed morph detector is summarized when a single group (with all its 8-rotations) of 2ULBP used as landmarks. Displayed results, correspond only to the best performing groups namely G_5 , G_7 or G_4.

Datasets	DTS	FNR	FPR	Acc
LcombineM	70%	4.6	22.9	86.2
	50%	6.6	33.9	79.8
	30%	8	49.6	71.2
LcompleteM	70%	7	20.5	86.2
	50%	7.5	32.4	80
	30%	9.3	48	71.4
LsplicingM	70%	6	16.4	84.2
	50%	6.4	17	79.4
	30%	6.6	18.2	71
UcombineM	70%	4.2	2.2	96.8
	50%	4.4	2.6	96.5
	30%	5.6	4.8	94.8
UcompleteM	70%	0.8	0.6	99.3
	50%	1.1	0.8	99
	30%	3.8	1.7	97
UsplicingM	70%	0	0	100
	50%	0	0	100
	30%	0	0	100
P&S	70%	2.3	0.1	98
	50%	1.7	0	99
	30%	2.3	0.1	98.8

Table 5-1: Performance of 8NSP landmark of PH-based morph detector using B_0.

Datasets	DTS	FNR	FPR	Acc
LcombineM (G_5)	70%	12.9	20.9	83.1
	50%	13.5	21.3	82.6
	30%	14.8	23.2	81
LcompleteM (G_5)	70%	16.5	26.4	78.5
	50%	17.9	27.3	77.4
	30%	19.1	30	75.5
LsplicingM (G_4)	70%	6	16.4	94
	50%	6.4	17	93.9
	30%	6.6	18.2	93.4
UcombineM (G_5)	70%	0	0	100
	50%	0	0	100
	30%	0	0	100
UcompleteM (G_7)	70%	0	1.3	99.3
	50%	0.1	1.2	99.2
	30%	0.1	1.4	99.1
UsplicingM (G_4)	70%	2.6	6.5	95.4
	50%	3.6	7.4	94.5
	30%	5.5	9.4	92.6
PS (G_5)	70%	7.2	10.2	91.3
	50%	8.6	11.2	90.1
	30%	13.8	13.3	86.4

Table 5-2: Performance of 2ULBP landmark of PH-based morph detector using B_0

The 100% accuracy result for UsplicingM is due to the obvious artefacts one gets from the morph generation process and the fact that we have a small dataset of genuine images may also result in some overfitting and hence we obtain 100% in UcombineM, too. Furthermore, frontal faces in face images in Utrecht dataset have bigger area which is due to the fact that the camera used to take images are closer than that of London DB. Finally, it also indicates that combine and splicing morphing technique destroy the topological features constructed from these specific landmarks. However, the full results for all groups of landmarks show in most cases a relatively small reduction in accuracy. To some extent, the patterns of accuracy achieved by these 2ULBP landmark groups are similar to those achieved by the 8-NSP landmarks with two exceptions. The accuracy of detection of LsplicingM morphing increased significantly to about 93.5%, for all protocols, in comparison to those achieved by the 8-NSP landmark as shown in Table (5-1). This may be explained by the known weakness of the splice morphing which produces visible artefacts. The other exception is the notable decline in detecting PS attacks by about 9% indicating higher sensitivity of the 8-NSP landmarks to PS morphing. Moreover, the effect of selected training/testing (DTS) protocol is somewhat marginal when using the 2ULBP landmarks with all databases including the London DB. In 2ULBP, FNR and FPR are much higher than that of 8-NSP in UcompleteM, UsplicingM and P&S. Comparing the results in the two tables, reveal differences in the performance of both 2ULBP and 8-NSP detectors over the different datasets. In particular, both types of landmark selection schemes perform better on Utrecht DB than on London DB. This could be attributed to a number of factors including the differences in the 2 DBs in terms of gender, ethnic and skin-color diversity of the participants as well as differences in face images resolution in the two databases.

Unfortunately, it is difficult to conduct a full like-with-like comparisons of the performance of our PH-based detectors with the state of the art morph detectors (e.g. [99],[95]). The authors in [99], proposed a generalized Benford's Law based detector (referred to as simple) and a linear SVM based detector. Besides testing their algorithm with the Utrecht and London database, they train and test their performance on their own acquired large database, not available publicly, of images (3186 Genuine and 8269 morphed images captured with a number of different quality cameras). There is no indication on the adopted training-testing protocols or how

many times the experiment is repeated. Notwithstanding these factors, their "simple" scheme performs better than our schemes for the London DB, whereas at least one of our schemes outperform their simple scheme on the Utrecht DB. Our schemes have much lower FPR than their Linear SVM scheme.

The **second** set of experimental tests were designed to investigate the effect of cross datasets training and testing on the performance of various detectors. So, instead of training NN on Utrecht DB only and testing images from Utrecht DB, we trained the classifier on the union of the Utrecht DB and the London DB while testing with the remaining images in either Utrecht or London. The results are displayed in Table (5-3) for the 8-NSP landmark and Table (5-4) for the 2ULBP landmarks.

Evidently, for the performance of the 8-NSP tested detector, shown in Table (5-3), very little or no change in accuracy was achieved when training with the images selected from U+L DBs (see Table (5-1)). The cross-DB performance for the 2ULBP based morph detectors on both datasets are shown in Table (5-4). While cross-DB training experiments helped increase the performance of the 2-ULBP detector on the London DB by about 3% across the different training-testing protocols. No improvement was detected when testing with images in the Utrecht DB.

Training	Testing	DTS	FNR	FPR	Acc
(U+L) combineM	LcombineM	70%	4.6	22.9	86.2
		50%	6.6	33.9	79.7
		30%	8	49.6	71.2
(U+L) completeM	LcompleteM	70%	7	21.5	85.7
		50%	7.5	33.3	79.6
		30%	9.3	49	70.9
(U+L) splicingM	LsplicingM	70%	6	16.4	84.2
		50%	6.4	17	79.4
		30%	6.6	18.2	71
(U+L) combineM	UcombineM	70%	0	1.4	99.3
		50%	0.1	3.9	98
		30%	0.1	9.5	95.2
(U+L) completeM	UcompleteM	70%	0.3	0.4	99.7
		50%	0.2	2.9	98.4
		30%	0.2	6.8	96.5
(U+L) splicingM	UsplicingM	70%	0	0.3	99.8
		50%	0	0.8	99.6
		30%	0.03	1.4	99.3

Table 5-3: Cross Database performance of 8NSP landmark PH-based morph detector using B_0.

Beside the differences mentioned earlier between the participants in the two databases, there are other factors that may explain the fluctuation of performance of the PH-based morph detector, shown in Tables (5-3) and (5-4), when testing images from Utrecht DB and from London DB been used respectively. First, the resolution of the two datasets used for testing are not consistent, Utrecht DB images have resolution of 900 by 1200 whereas London DB images are of 1350 by 1350. Secondly, the London DB is more diverse than Utrecht DB. More than 30% of images in London DB are (non-white) Asian and dark-skin participants whereas this ratio is below 10% in Utrecht DB.

Training	Testing	DTS	FNR	FPR	Acc
(U+L) combineM	LcombineM	70%	0.5	21.3	89.1
		50%	1.1	32.8	83
		30%	17	48.5	74.9
(U+L) completeM	LcompleteM	70%	1	21.1	88.9
		50%	1.5	32.9	82.8
		30%	2.3	49.1	74.3
(U+L) splicingM	LsplicingM	70%	6	16.4	94
		50%	6.4	17	93.9
		30%	6.6	18.2	93.4
(U+L) combineM	UcombineM	70%	0	0	100
		50%	0	0	100
		30%	0	0	100
(U+L) completeM	UcompleteM	70%	0	1.3	99.3
		50%	0.1	1.2	99.2
		30%	0.1	1.4	99.1
(U+L) splicingM	UsplicingM	70%	0.3	2.1	98.8
		50%	0.2	10.2	94.8
		30%	0.5	16.5	91.5

Table 5-4: Cross Database performance of 2ULBP landmark of PH-based morph detector using B_0.

So far, we illustrated the results of computed number of persistent B_0 from automatically extracted image landmarks. Next, we show the results of calculated number of persistent B_1 from using 2ULBP and 8NSP landmarks and the two databases mentioned earlier, i.e. Utrecht DB and London DB. Table (5-5) shows that except for LcombineM, the number of 1-dimensional holes, i.e. B_1, is performing as

close as (sometime the same) the number of connected components calculated from Rips SC built on 2ULBP landmarks to distinguish morphed faces from genuine ones.

Datasets	DTS	FNR	FPR	Acc
LcombineM (G_5)	30%	19.6	25.2	77.5
	50%	19.5	25.3	77.6
	70%	18.4	26.1	77.7
LcompleteM (G_5)	30%	23.3	31.7	74.7
	50%	20.6	31.4	75.6
	70%	19	31.4	76.3
LsplicingM (G_4)	30%	14.1	19	91.6
	50%	12.7	18.5	92.5
	70%	10.9	17.8	92.8
UcombineM (G_5)	30%	0	0	100
	50%	0	0	100
	70%	0	0	100
UcompleteM (G_5)	30%	0.2	10.2	94.8
	50%	0.02	6.8	96.6
	70%	0	4.7	97.6
UsplicingM (G_5)	30%	5.2	7.1	93.8
	50%	4.8	6.8	94.2
	70%	4.7	6.9	94.6
PS (G_3)	30%	9.12	7.74	90.9
	50%	5.6	6.6	93.3
	70%	5	13.6	94.1

Table 5-5: Performance of the number of 1-dimensional homology features of 2ULBP landmarks.

In general, similar to B_0, computed number of B_1 is performing better on Utrecht database than London DB due to the reasons we discussed earlier in this section. 8NSP landmark selection method, on the other hand, performed poorly when the number of B_1 computed for the Rips SCs constructed by this landmark selection method. In Table (5-6), we summarize the results we obtained for calculating the number of B_1 when 8NSP used as a landmark selection criterion. The only positive point about using B_1 together with 8-NSP landmark selection method is that the number of FPR, i.e. number of genuine images classified as morphed image, is lower than that of 2ULBP method. Again, Utrecht database is slightly better than London DB when using 8-NSP and B_1, which confirms that our algorithms for landmark selection and PH feature generation works better on Utrecht DB than London DB.

Dataset	DTS	FNR	FPR	Acc
LcombineM	30%	53	17.7	49
	50%	53.8	16.2	48.5
	70%	53.7	15.2	48.6
LcompleteM	30%	66.2	15.8	38.1
	50%	67.4	13.9	37.1
	70%	67.4	12.8	37.4
LsplicingM	30%	68.07	16.4	36.7
	50%	69.5	14.9	35.5
	70%	69.7	14.1	35.4
UcombineM	30%	42.7	33.04	62.1
	50%	41.6	29.7	64.4
	70%	39.7	28.9	65.7
UcompleteM	30%	47.8	38.3	56.9
	50%	47.6	36.8	57.8
	70%	47.2	37.2	57.8
UsplicingM	30%	45.7	33.4	60.5
	50%	43.4	30.7	62.9
	70%	42.4	30.07	63.7
PS	30%	44.5	35.1	53.9
	50%	41.4	32.5	57.3
	70%	39.2	30.7	58.5

Table 5-6: Performance of the number of 1-dimensional homology features of 8NSP landmarks.

To further understand and analysis the features we extracted from the two databases, we use Mapper algorithm, explained in section (5-6), as an attempt to get more insight into the nature of the homological features we used to discriminate genuine faces from their morphed counterparts.

5.5 Classification Performance of R-LBP and CS-LBP

In this section we illustrate the performance of two more image landmark selection criteria which we discussed in section (5.1.3) and section (5.1.4), namely R-LBP and CS-LBP. Radial Local Binary Patterns (R-LBP) is a novel approach we proposed for the purpose of landmark selection in this thesis, together with the rest of the 3 landmark selection methods to construct Rips complexes on digital images for the purpose of image tampering detection. The experiments conducted on using one morph creation method and the two datasets of Utrecht and London, i.e. LcombineM and UcombineM. There are two reasons behind this, first is if our algorithm can

detect morphs created using Combined approach, then most certainly it will detect splicing and complete morph face images. Because in practice, morphs created by splicing and complete methods will have visible artifacts and is easier to detect than combined morph. The advantages of combined morph as well as the limitation of splicing and complete morph have been discussed in detail in chapter 3, section (2.3.1). Secondly, to save computational time because the PH calculation takes longer in R-LBP and CS-LBP in comparison with 2ULBP and 8NSP landmark methods. This is mainly because the number of selected pixel landmarks is increasing when we use 16 bins to group images of size 413x531 instead of 256 bins which was the case in 2ULBP. Typically for 2ULBP and 8NSP landmark selection criteria, PH calculation for an image in London DB takes (1-15) seconds to finish for each rotation whereas in Utrecht DB it takes between (1-40) seconds to finish depending on the structure of the face and consequently the number of points feed into Ripser software for calculation. These numbers are increased to (1-120) seconds for London DB and 1-200 seconds for Utrecht DB when R-LBP used as a landmark selection criterion. In the same vein, images in London DB took 10-300 seconds to compute their PH features for one rotation whereas face images in Utrecht DB takes about 500-1000 seconds to calculate their PH features in both dimensions when we use CS-LBP as landmark selection approach. The experiments were conducted using a macOS laptop with 2.7 GHz Intel Core i5 and 8GB of RAM. Parallel computing is one of the solutions which can be used to tackle the issue of computational time, but we leave this issue as a future work as it is not the main focus of this thesis.

We use KNN (with k=1) classifier to measure the performance of the R-LBP and we selected 70% of the images for training purposes and the rest for testing. Each experiment repeated 100 times and we report the average accuracy together with false positive rate and false negative rates. We remind the reader that false positive rate is the percentage of genuine face images misclassified as morphed faces while false negative rate is the percentage/rate of morphed face images incorrectly classified as genuine faces. Unlike the case of 2ULBP codes, here we only have 3 uniform R-LBP groups which have binary patterns with more than one rotation, see figure (5-1) in section (5.1.3). Also, instead of having 8-rotationsas which was the case with 2ULBP codes, here we only have 4-rotations. Therefore, we opt to use different approaches to

concatenate the topological features of different groups of R-LBP to boost the morph detection performance which can be seen in the tables below.

Dataset	R-LBP geometry	FNR	FPR	Acc
LcombineM	G_1	26.4	38.6	67.9
	G_2	16.4	18.4	82.7
	G_3	30.8	30.9	69.1
	G_1 & G_2	23.2	27.1	75
	G_1 & G_3	23.8	29.8	73.4
	G_2 & G_3	17.2	17.1	82.8
	G_1 & G_2 & G_3	16.9	14.83	84
UcombineM	G_1	7.2	7.3	92.8
	G_2	4.4	4.5	95.5
	G_3	9.4	19.6	86.7
	G_1 & G_2	3.6	6.8	95.2
	G_1 & G_3	5.8	9.1	92.9
	G_2 & G_3	2.5	5.5	96.4
	G_1 & G_2 & G_3	3.1	5.5	96

Table 5-7: Performance of R-LBP using B_0 as topological feature to detect morphs

Result in Table (5-7) indicates that the best performance one can obtain for LcombineM is 82% with G_2 when only one geometry of R-LBP used to construct Rips SC and then calculated number of persistent B_0 used as a feature vector. The overall accuracy of morph detection improved together with FPR and FNR when we concatenate topological features extracted from G_1, G_2 and G_3. On the other hand, consistent with the result of other landmarks and different topological features, the performance of morph detection in Utrecht DB is better than London DB in general. Single geometries of R-LBP codes are performing almost as good as concatenating all of the geometries together. For example, G_2 of R-LBP is achieving accuracy of 95.5% with $FNR = 4.4$ and $FPR = 4.5$, whereas combining $G_1 + G_3$ or $G_1 + G_2 + G_3$ improves the overall accuracy by only 0.5% but higher FPR. Lastly, comparing the results of 2ULBP and R-LBP for London DB, 2ULBP's performance is better in overall accuracy and FNR while R-LBP's FPR is better by 8%.

Dataset	R-LBP geometry	FNR	FPR	Acc
LcombineM	G_1	24.9	32.7	71.5
	G_2	17.2	16.8	82.9
	G_3	30.9	34.2	67.5
	G_1 & G_2	14.4	14.2	85.8
	G_1 & G_3	24.3	32	72
	G_2 & G_3	12.8	12.2	87.4
	G_1 & G_2 & G_3	14.1	11.9	86.8
UcombineM	G_1	5.5	6.4	94.1
	G_2	9.7	6.8	91.4
	G_3	7.2	8.2	92.4
	G_1 & G_2	4.7	7.7	94.1
	G_1 & G_3	5.5	7.3	93.8
	G_2 & G_3	3.3	10.5	93.96
	G_1 & G_2 & G_3	3.1	5.9	95.9

Table 5-8: Performance of R-LBP using B_1 as topological feature to detect morphs.

Using the persistent B_1 computed on the R-LBP landmarks, the overall performance of London DB improved in terms of FNR, FPR and accuracy. Comparing this result of London DB with the results obtained when 2ULBP method used as a landmark selection, R-LBP is better in terms of overall accuracy by 9% while FNR and FPR improved by 4% and 10% respectively. When it comes to Utrecht DB, 2ULBP performed perfectly using persistent B_1 whereas the best performance we obtained using R-LBP is when we concatenated B_1 features calculated from all geometries of R-LBP. The next question arising from this analysis is that: Does the concatenation of B_0 and B_1 help to improve the performance of morph detection? in a single geometry of R-LBP or more. The results in the next table, Table (5-9), answers the question raised earlier. It can be seen from Table (5-9), that concatenating persistent topological features of B_1 and B_0 is not improving the morph detection performance significantly in either of the datasets nor in any specific geometry (or a fusion of geometries) of R-LBP.

Next, we demonstrate the results obtained from CS-LBP landmark selection method for the purpose of morph detection on both Utrecht and London databases. We follow the same experimental setting we setup for R-LBP in terms of morph creating method selection, classifier and feature concatenation.

Dataset	R-LBP geometry	FNR	FPR	Acc
LcombineM	G_1	24.4	36.9	69.9
	G_2	16.7	16.5	83.4
	G_3	29	33.7	68.8
	G_1 & G_2	16.9	17.4	82.8
	G_1 & G_3	24.4	29.8	73.1
	G_2 & G_3	16.9	17	82.9
	G_1 & G_2 & G_3	16.7	15.5	83.9
UcombineM	G_1	7.5	7.7	92.4
	G_2	7.2	10.5	91.5
	G_3	6.9	10.9	91.6
	G_1 & G_2	3.6	7.3	95
	G_1 & G_3	2.5	8.2	95.3
	G_2 & G_3	2.8	6.8	95.7
	G_1 & G_2 & G_3	2.5	6.4	96

Table 5-9: Performance of R-LBP concatenating B_0 and B_1 of topological feature to detect morphs.

We show the results we obtained for CS-LBP through tables (5-10) -(5-12). We took similar approach as R-LBP to analyse the performance of CS-LBP landmark selection criterion which is based on topological features in different dimensions.

Dataset	CS-LBP codes	FNR	FPR	Acc
LcombineM	G_1	24.6	32.5	71.4
	G_2	21.4	30.0	74.3
	G_3	22.69	32.7	72.3
	G_1 & G_2	18.3	30.6	75.6
	G_1 & G_3	17.4	30.3	76.2
	G_2 & G_3	16.7	30.4	76.5
	G_1 & G_2 & G_3	13.8	30.0	78.1
UcombineM	G_1	6.8	11.6	91.2
	G_2	5.6	10	92.7
	G_3	7.3	13.2	89.8
	G_1 & G_2	5.1	9.5	92.7
	G_1 & G_3	7.7	10.5	90.1
	G_2 & G_3	3.2	11.8	92.5
	G_1 & G_2 & G_3	6.4	10.9	91.4

Table 5-10: Performance of CS-LBP using B_0 as a topological feature to detect morphs.

As it was the case with previous landmark selection criteria, CS-LBP performs better on Utrecht DB in comparison with London DB. The overall conclusion one can make for both topological features, i.e. B_0 and B_1, extracted based on CS-LBP is that it is not performing as good as R-LBP, 2ULBP and 8NSP landmark selection methods to

Dataset	CS-LBP geometries	FNR	FPR	Acc
LcombineM	G_1	20.8	30.3	74.5
	G_2	23.4	28.6	73.9
	G_3	23.4	27.0	74.8
	G_1 & G_2	17.7	24.2	79.1
	G_1 & G_3	19.8	32.0	74.1
	G_2 & G_3	19.9	25.1	77.5
	G_1 & G_2 & G_3	16.7	26.9	78.2
UcombineM	G_1	6.2	15.4	89.9
	G_2	7.6	12.4	90.4
	G_3	9.5	14.1	88.2
	G_1 & G_2	4.9	11.9	91.6
	G_1 & G_3	6.8	11.4	90.9
	G_2 & G_3	8.2	15.9	87.9
	G_1 & G_2 & G_3	2.7	11.8	92.7

Table 5-11: Performance of CS-LBP using B_1 as a topological feature to detect morphs.

Dataset	CS-LBP geometry	FNR	FPR	Acc
LcombineM	G_1	21.9	30.3	73.8
	G_2	18.4	25.1	78.2
	G_3	19.4	28.5	76.0
	G_1 & G_2	14.4	27.1	79.3
	G_1 & G_3	15.8	27.6	78.3
	G_2 & G_3	16.5	27.2	78.2
	G_1 & G_2 & G_3	12.9	27.5	79.8
UcombineM	G_1	5.9	8.8	92.6
	G_2	4.9	7.5	93.8
	G_3	5.9	10.5	91.8
	G_1 & G_2	4.2	9.2	93.3
	G_1 & G_3	6.8	9.1	92.0
	G_2 & G_3	3.182	9.5	93.6
	G_1 & G_2 & G_3	4.091	10.9	92.5

Table 5-12: Performance of CS-LBP using B_0 and B_1 as a topological feature to detect morphs.

differentiate morphed faces from genuine ones. This conclusion is true for different approaches of topological feature concatenations as well as feature concatenation between different groups of CS-LBP.

Beside the poor performance of CS-LBP in differentiating morphed faces from genuine face images, the computational time needs to extract topological features for

one rotation (any geometry) can go to beyond 1000 seconds which makes this approach impractical in real life.

5.6 Insight into Morphing Problem

The clear variations in the performance of the above PH-based morph detectors when tested with the two main datasets, may not be fully explained by the variations between the participant groups. In order to have a better insight into this problem, we conducted two basic comparative studies of the genuine and morphed images in the two databases: a statistical analysis of the landmarks and a Mapper-based clustering.

5.6.1 Landmark Statistics

Ahonen et al. in [130], reported that around 90% of face image pixel values have one of the ULBP codes and Ojala et al. [92] noticed that just under 90% of texture images pixel values are of type uniform LBP codes. We conducted some statistical analysis of the distribution of image pixel codes within each of the landmark sets (ULBP, R-LBP, CS-LBP) that have been used in the various experiments conducted in this chapter. In the table below, we only present the outcome for the ULBP, because no prior information is available in the literature on the distributions of the R-LBP or the CS-LBP for large datasets of face images. Our current analysis was carried out on samples of genuine and morphed images from the two databases separately.

London DB	Morphed	Genuine	Utrecht DB	Morphed	Genuine
G_1	0.339682	0.415242	G_1	1.309142	0.815923
G_2	1.345604	1.311656	G_2	3.194411	3.19743
G_3	1.522883	1.424035	G_3	2.795207	2.885472
G_4	1.266359	1.244549	G_4	3.524773	3.390719
G_5	1.732496	1.634599	G_5	3.510042	3.826637
G_6	2.146982	1.999673	G_6	4.07204	4.38027
G_7	1.158143	1.14897	G_7	2.925474	2.930188
G_0	87.8033	87.6744	G_0	69.35	72.96
G_8	1.284549	1.546877	G_8	4.31891	1.613361

Table 5-13: Face image pixel distribution ratio according to ULBP groups of Utrecht and London DB.

These statistics demonstrates a clear variation in the percentages of the various groups of the ULBP landmarks within each of the two databases. This seems to

provide some partial explanations as to why the various PH-detectors performance for the London database is different than that of utrecht dataset. This can be seen by noting that (1) for each landmark the gap between their % in the genuine and morphed images in the London database are much smaller than the corresponding gaps in the Utrecht database. On the other hand, when the classifier is trained and tested cross-databases we expect that the average % gaps between genuine and morphed images are reduced when compared to the corresponding gaps for the Utrecht database but slightly larger than those for the London database. This may provide some explanations as to why combining images from two databases do not lead to better performance. These are only partial explanations because similar numbers of landmarks do not necessarily yield topologically similar shapes and homology invariants at distance thresholds. Therefore, in the next section we should use mapper as a clustering analysis to complement the statistical analysis conducted in this section

5.6.2 Mapper-Based clustering

Mapper is another TDA tool, beside Persistent Homology, that can be used to get more (topological/homological) insight into high dimensional datasets. We introduced the basics of mapper algorithm in chapter two, and here we discuss its use settings for our objective of understanding the differences in the clustering of the PH-feature vectors for morphed as well genuine face images selected randomly from the two databases we used for the purpose of morph detection as well as the power of the topological features used to design PH-based morph detection tool. We used Keppler mapper in Jupyter notebook (ipython version 7.6.1 using anaconda3) with two lenses and k-means as our clustering step with $k = 2$. The two lenses used are Isolation Forest and l_2-norm, and the binning overlap of two consecutive bins is 0.5.

Isolation Forest is an efficient popular algorithm proposed for the purpose of anomaly detection. It is easy to extend for parallel computing and it has been proved to perform very well in anomaly detection in comparison with other anomaly detection algorithms. The hypothesis under which isolation forest works is that 'few and different' data are suspected to be anomalies, whereas other anomaly detection techniques rely on a constructed profile for the input data and samples that do not conform to this profile will be treated as anomalies. Furthermore, isolation forest approach sub-samples and processes input data in a tree structure manner and

randomly prunes values of the selected features of the input data. Samples that travel deep through the tree branches are treated as normal samples whereas samples with short aggregated lengths to the tree branch are treated as anomalies. In other words, each sample is attached an anomaly score reflecting the aggregated length of the sample along the constructed binary trees. We direct interested reader to see [135][136] for details on how isolation forest works and further technicalities.

Isolation forest is used here as one of the lenses to highlight special homological features that contribute to morph detection and the l_2-norm quantify the data spread to gain more local information. These two lenses combined and used as a 2-dimensional lens. The output from mapper algorithm is a simplicial complex where each node represents a cluster of images with similar feature characteristics. The bigger the size of the node in the mapper output, the bigger the number of images it represents.
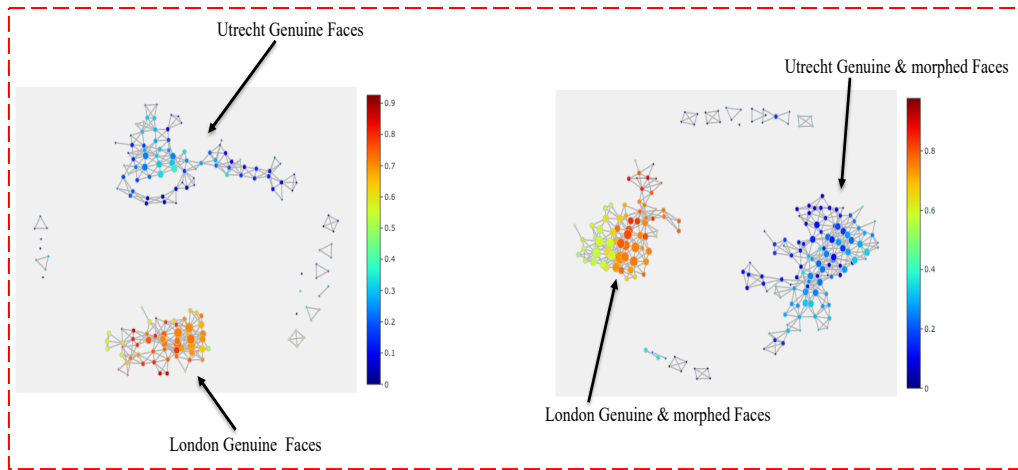
Figure 5-5: Mapper Algorithm output of G_4-ULBP landmark of (left)Genuine faces of Utrecht and London DB and (b) genuine &morphed faces of Utrecht DB and London DB.

It can be seen from figure (5-5) that the two datasets, Utrecht DB and London DB, are clustered quite apart and hence different in terms of the topological features computed from them. To some extent, this diagram together with the above statistical analysis justifies the results obtained from Table (5-3) and Table (5-4). In fact, we can see that combining the two datasets at training phase is highly unlikely to improve the performance of morphing detection. It is worth to mention that the position of the nodes in figure (5-5) is not important, it is the neighborhood connectivity of the nodes that is important, i.e. proximity of the neighboring clusters. The class label of images that fall within a cluster node is dependent of the class of

the images in the cluster as well as that of images in neighboring clusters. Note that in the left of figure (5-5) the genuine images in the two databases are clustered in different regions, and when we added the morphed images together with genuine face images, clusters of the images from the two databases remained far away from each other. This explain that the differences in gender ratio, ethnicity, resolution and color that the two datasets have are reflected in the mapper results. This confirms that one needs different datasets, maybe many different datasets, to build strong morph detection tools which are not biased towards a particular ethnicity or skin-color. We also anticipate the need or fusing more landmark-based schemes and/or other types of landmarks.

We complemented this experiment by using the same approach to get more insights within each individual dataset with respect to topological features of 0 and 1dimension for some geometries of 2ULBP landmark. The input to mapper is PH features extracted from 2ULBP landmark which are B_0 and B_1, i.e. the number of connected components and 1-dimensional holes/loops. The dimension of the feature vectors is 800, as we have 8 rotations in each G_λ of 2ULBP and using persistent binning, we bin each constructed persistent barcode 100 times. This approach is different from the usual approach of using the raw data as an input of mapper algorithm and opens the door to use mapper as a tool to measure the quality of extracted features.
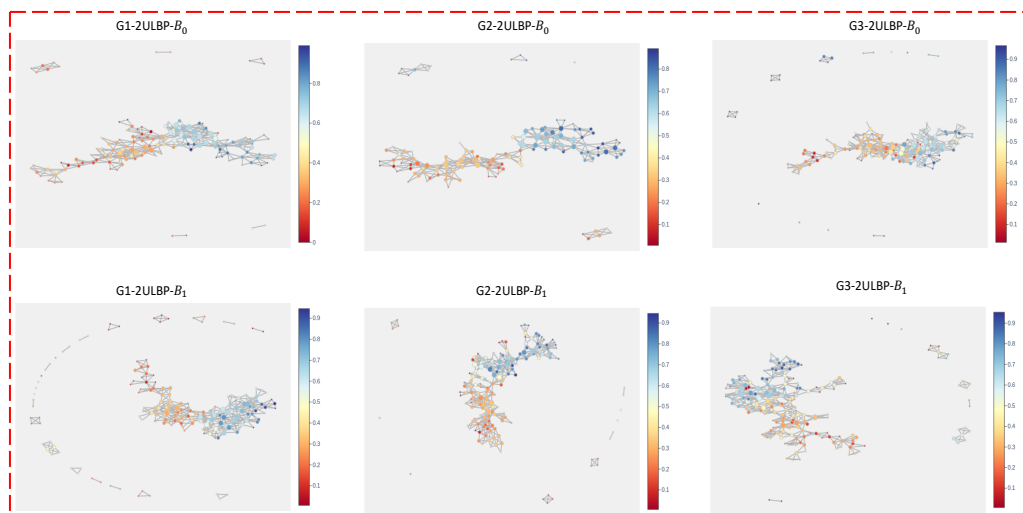
Figure 5-6: Mapper projection/output of PH features extracted from Genuine and combined morph faces of Utrecht DB for G_1-to-G_3 of 2ULBP landmark of B_0 and B_1.

Figures (5-6)-to-(5-8), illustrate that topological features of both dimensions successfully distinguish genuine face images from (combined) morphed face images. The red nodes represent genuine face images and the blue-colored nodes are morphed images. Each node contains a label (or labels) of the images we insert to mapper such that labels from 1-75 are for genuine faces and 76-150 is for morphed faces. The color-bar on the left of each graph depicts this information. A bold red node(s)/region indicates that labels clustered by these nodes are strongly indicating to be genuine faces and vice versa for the blue/morphed faces.
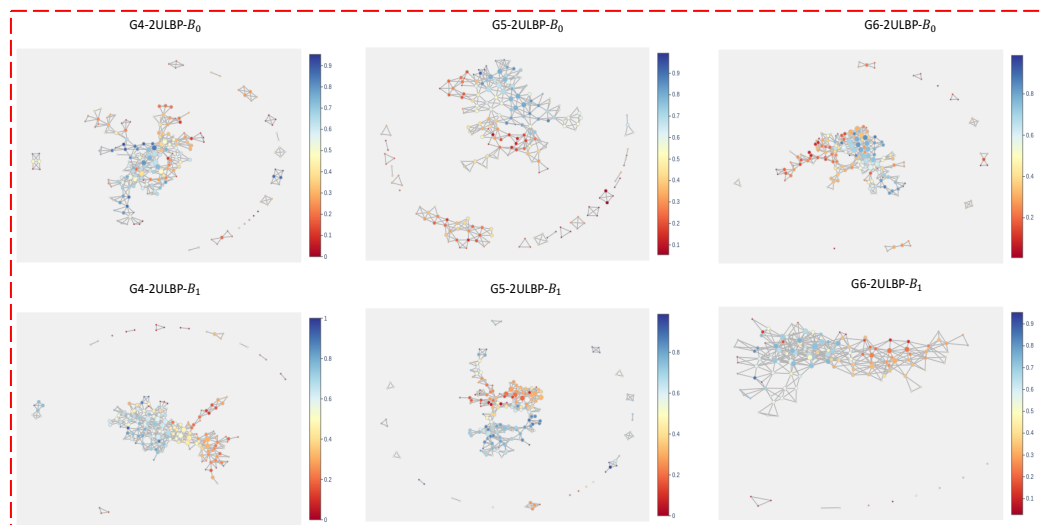
Figure 5-7: Mapper output of PH features extracted from Genuine and combined morph faces of Utrecht DB for G_4-to-G_6 of 2ULBP landmark of B_0 and B_1.
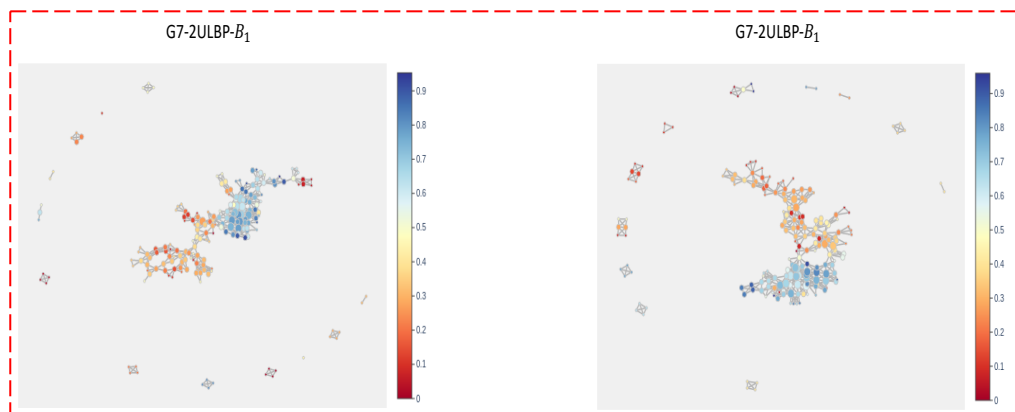
Figure 5-8: Mapper projection of PH features extracted from Genuine and combined morph faces of Utrecht DB for G_7 of 2ULBP landmark for B_0 and B_1.

We follow the same approach to analyse London DB where we used 102 genuine faces together with 102 combined morphed face images. Figures (5-9)-to-(5-11), shows the mapper algorithm output when we input the PH features extracted from genuine and morphed faces based on 2ULBP landmarks. Again, red nodes represent

103

genuine faces and blue nodes/regions represent morphed faces. It is somehow straightforward to see that the distribution of the nodes according to the two colors (red and blue) is not similar as that of the Utrecht DB, and hence the classification performance is not as good as the Utrecht DB, see Table (5-2) and Table (5-5). Nonetheless, there are still some separations but the orange nodes/region in the mapper output of London DB is higher than that of Utrecht DB which means more uncertainty. For example, in the mapper output SC in Figure (5-8) we can see many red/orange nodes which represent genuine face images being clustered very close to/with the blue nodes region which contain morphed face images.
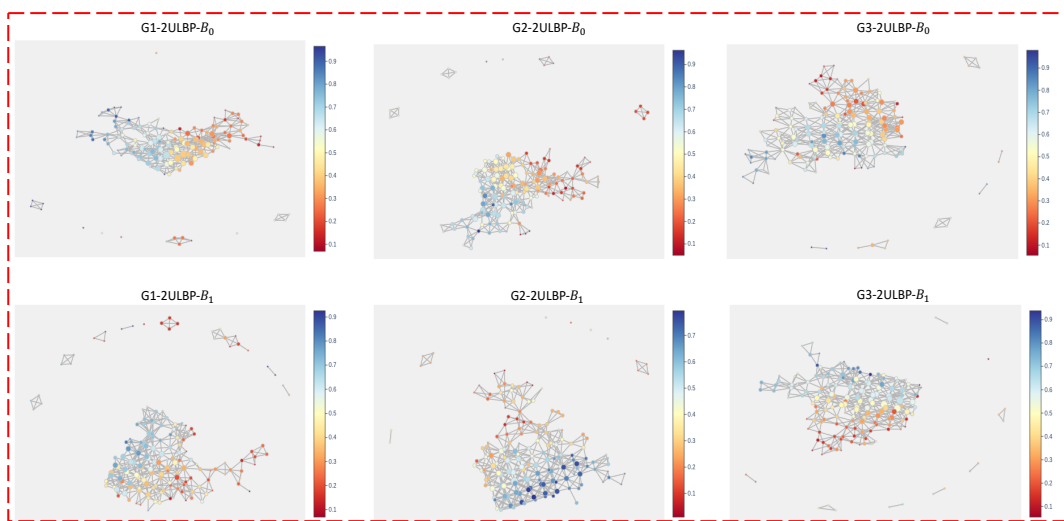
Figure 5-9: Mapper output of PH features extracted from Genuine and combined morph faces of London DB for G_1-to-G_3 of 2ULBP landmark of B_0 and B_1.
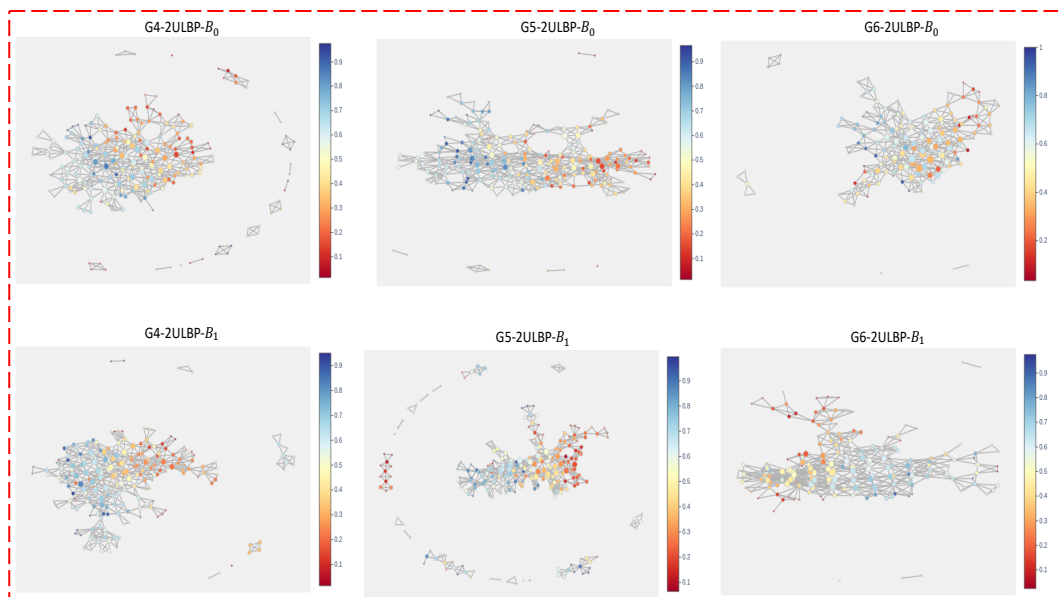

Figure 5-10: Mapper output of PH features extracted from Genuine and combined morph faces of London DB for G_4-to-G_6 of 2ULBP landmark of B_0 and B_1.
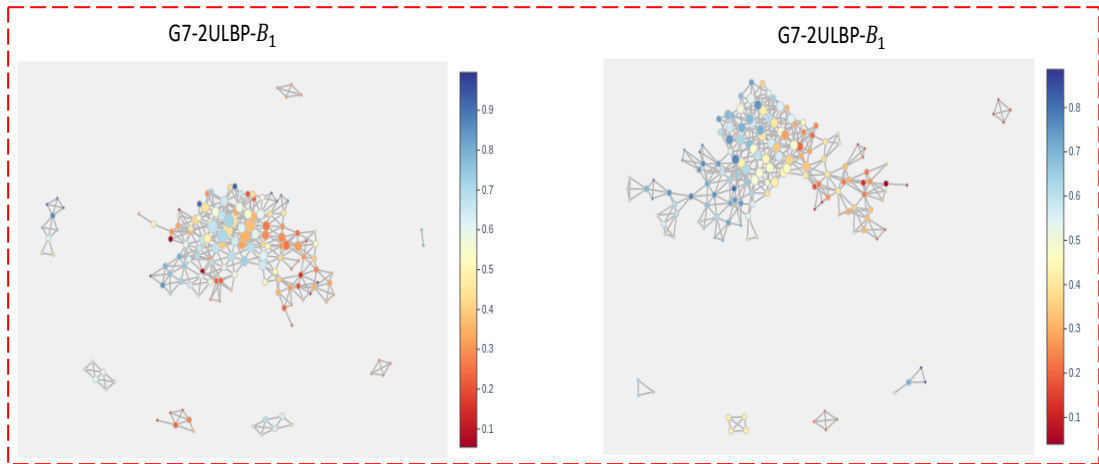
Figure 5-11: Mapper projection of PH features extracted from Genuine and combined morph faces of London DB for G_7 of 2ULBP landmark for B_0 and B_1.

5.7 Chapter Summary

In this chapter, we described the design of our proposed PH-based face morph attack detector using not only the ULBP landmarks but for several newly introduced types of image texture landmarks. We also presented a detailed analysis of the performance of the PH-based morph detectors using these various landmark selection methods. Two different databases of face images, together with a dataset of P&S images, were used to test the performance of PH-based morph detection approaches as well as different training and testing schemes. In addition the issues raised in chapter 4 have been addressed whereby the morph detection algorithm proposed in this chapter is topological construction threshold independent, exploiting Persistent Homology. Unlike chapter 4, topological feature extracted from persistent barcodes are all concatenated in one feature vector and feed into KNN classifier. The fact that out PH-based morph detection algorithms can detect morphed faces in different datasets, albeit inconsistent performance, is a sign of strength of the topological features for morph detection problem. We also illustrated the use of the mapper clustering tool and statistical analysis of the presence of the various studied landmarks to understand/justify the discrepancies in performance of PH-based detector for different databases of images.

Chapter 6

Further PH-based Image Distortion Detectors

In previous chapters, PH-based methods were developed and used to detect fake face images, constructed through morphing attacks, that blends together certain texture features from different face images for malicious purposes. The different level of success achieved by a variety of PH-based detectors rely on the level of changes to the spatial distributions of certain texture landmarks in a manner often undetectable by average human observer. Morphing is only one example of image analysis applications that cause such type of texture distortions, and these distortions could be due to a variety of not necessarily malicious acts. Such applications are expected to benefit from our PH-based approach to design detectors. Moreover, measurable distortion in the spatial distribution of certain primitive texture landmarks can be used as a measure of image quality, so any image reconstruction can benefit from TDA consideration. In this chapter, we investigate the viability of using TDA-based approach in other than the malicious morphing attacks. We only present 3 case studies of image processing/analysis applications and demonstrate strong viability for effective use of TDA approach, namely (1) steganalysis for discovery of hidden secrets in digital images, (2) digital image inpainting, and (3) medical image analysis for diagnosing breast tumours.

6.1 PH-based Approach to Digital Steganalysis

In the digital world, online transmission is the main method to exchange sensitive and private information in sectors like mobile banking/commerce, sensitive cloud transactions, and crime/terrorism fighting and many more. The important question arises when it comes to using a carrier (e.g. a digital image) to send some sensitive/secret information how one can be certain about authenticity and confidentiality of the secret? One of the mechanisms designed and developed in the last two to three decades to protect sensitive data from an unauthorized person or

misuse of the private data is known as Steganography. Roughly speaking, steganography is the science of hiding information (e.g. biometric data) into host innocuous image (cover-object, or carrier) in such a way that no suspicion could be raised by onlookers. Steganography can also be seen as a technique to protect sensitive biometric data (e.g. fingerprint, iris, face, voice, …etc.) while transmitting over open network channels. Here, the focus is on the steganography techniques where the carrier is a digital image. Main challenges in digital steganography are (i) capacity, i.e. the amount of sensitive information that could be hidden inside the carrier, (ii) invisibility of the secret, and (iii) robustness against attacks that aim to change or render the secret unreadable by the legitimate recipient. In digital steganography, the secrets are assumed to have the form of a binary string the individual bits of which are used to change the carrier pixel values, in very tiny way so that only the legitimate recipient can read. Here, we only consider grayscale image and all hiding procedures are implemented in the spatial domain.

Steganalysis, is the art of detecting carriers (images) that contain sensitive information by unauthorized persons. The main goal of steganalysis is to demonstrate enough evidence whether an image does (or does not) contain any hidden data. There are different approaches of analysing suspect digital images but mostly based on extensive statistical analysis, with different aims including mere identifying an image as a carrier or not, extracting hidden secret messages and destroying the secret data [137]. We aim to design a PH-based carrier detection without extracting the embedded secret. Our approach is based on the accepted wisdom that any attempt to hide a secret inside an image results in changes to texture, no matter how tiny.

To start investigating and exploiting the use of TDA as a steganalysis tool, we choose 100% payload capacity with 3 different commonly used steganography schemes to hide the secret inside a digital image. Here, 100% capacity means that all pixel values of the carriers are used to hide information.

This case study, was conducted in collaboration with the then fellow Buckingham PhD student Dr Rasber Rashid (currently at Koya University-Iraqi Kurdistan) whose research was focused on secretly embedding biometric data, converted into binary string as a mean of protecting their security when transmitted by law enforcing agencies over open channels. Three steganographic techniques were investigated in

that work, namely the Traditional Least Significant Bit (TLSB), the LSB-Witness [137] and the content-based Spatial Universal Wavelet Relative Distortion (S-UNIWARD) [138]. For this section to be self-content, we shall briefly describe these schemes.

6.1.1 Least Significant Bit (LSB) Steganography

There are many LSB based steganography schemes but all read the cover image pixels as an 8-bit binary strings. The LSB simply refers to the right-most bit value in the pixel binary sequence. For example, in the following binary bit strings 11001000 and 10110001, LSB is 0 and 1 consequently. LSB based secret hiding process the secret bits one by one the LSB of a single pixel in the cover image is replaced (or XORed) with current secret bit. To prevent detection of the secret, it is necessary not to embed the secret bits sequentially. In this case, one can give the secret bit string a random shuffle, agreed in advance with the recipient. The popularity of LSB-based secret hiding is that cover pixel values are either changed by 1 or remain unchanged, resulting in small invisible changes to pixel values and no artefacts could be detected by human eye, see below figure. Here we consider the following two such schemes for detection by a PH-based tool.

TLSB: traditional-LSB is simply replacing the LSB in cover image with that of the secret message bit by bit.

LSB-Witness [137]: In this technique, the 2nd LSB will act as a witness for 1st LSB in the cover image. Roughly speaking, the steganographer will change the 2nd LSB plane to 1 when the secret message bit is not equal to the 1st LSB bit of the cover image, otherwise change the 2nd LSB to 0.


| Original | TR_LSB | LSB-Witness | S-UNIWARD |
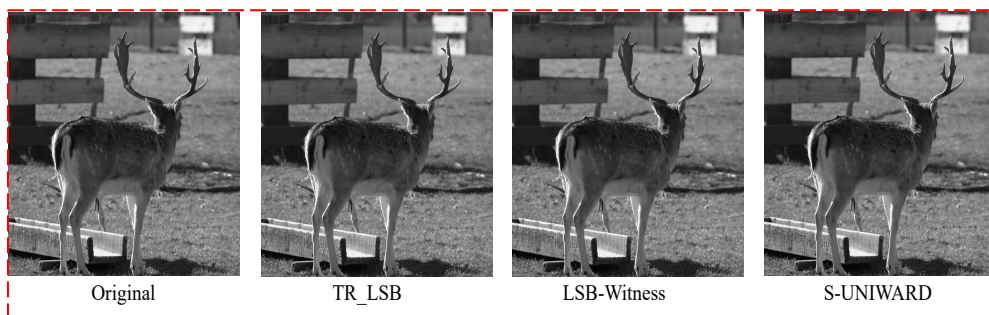
Figure 6-1: Original Cover image and the stego-image using TLSB, LSB-witness and S-UNIWARD steganography**.** Note that there are no visible artefacts that can be seen by layman eyes.

6.1.2 Content-Based Steganography

Content-based steganographic scheme refers to schemes for which the embedding benefits from the knowledge of the specific structure/nature of the content to be embedded. One of such schemes is known as the S-UNIWARD, proposed by V. Sedighi et al [138], that efficiently embed secrets into images that share similar characteristics with the secret sequence in order to minimize the necessary changes in the cover image and maintain high quality and robustness. S-UNIWARD works to minimize the overall distortion of the cover image especially for those areas of the cover image rich with textures. It is a spatial domain hiding scheme which utilizes the amount of distortion present between both original cover image and that of the secret message (stego image).The scheme utilises the distortion function in order to find the best locations for embedding and it is perceived to be robust against existing steganalysis tools.

The main question is how one can tell whether there is a secret message in the input digital image or not, in the absence of prior information about the input digital image. Most of the steganalysis techniques depend on a statistical approach to detect/measure the probability of an image being embedded with some sort of data or not. Just as in the case of face image morphing, hiding a message in a digital image results in tiny invisible distortion in the cover image. Hence, the above question is expected to benefit from applying similar topological approach to our approach to prevent morphing attacks.

In general, there are two categories of steganalysis techniques known as *specific* and *universal* steganalysis techniques. Specific steganalysis techniques are designed to target specific steganography methods to evaluate the robustness of these specific embedding techniques. These specific steganalysis methods may not detect stego-images produced by other steganographic methods [139]. For example, if a steganalysis technique developed to detect only TLSB technique, it may not detect non-LSB methods. Universal steganalysis methods, on the other hand, are general methods designed to detect stego-images without depending on any specific steganographic methods. Our method is labeled under a universal approach as it can detect LSB-based methods (e.g. TLSB and LSB-Witness) as well as content-based methods (e.g. S-UNIWARD). Next, we discuss the experimental results of using our PH-based tool for the detection of stego images.

6.1.3 PH-based Steganalysis – Experiments and Results

The various methods of hiding a secret binary string in a digital image, described above, results in relatively small changes to pixel values. Therefore, one expects some changes in the membership of the various groups of LBP landmarks, whereby some elements of a ULBP sets change to become a member of a different ULBP group or become non-uniform and vice versa [140]. This means that even if the number of landmarks in a group does not change significantly, their spatial distribution might change. Therefore, we proposed to design a PH steganalysis tool in the same was as discussed in the last two chapters and test the performance of this approach by evaluating changes in the persistent homology features (e.g. persistent Betti number B_0) as a result of secret hiding.

First step in designing our topological steganalysis is taking mod-16 for the input image. This is to decrease the range of the pixel values from 0 to 255 into 0 to 15. The reason behind this pre-processing step is due to the fact that the three techniques of steganography we investigated change the first two LSB values and thus we only need to focus on the first 4 bits. Second step is choosing the ULBP encoded pixels as our landmark selection criteria, and more importantly selecting the right group(s) for stego image detection. We build Rips complexes as mentioned in chapter 4, section 4.3.
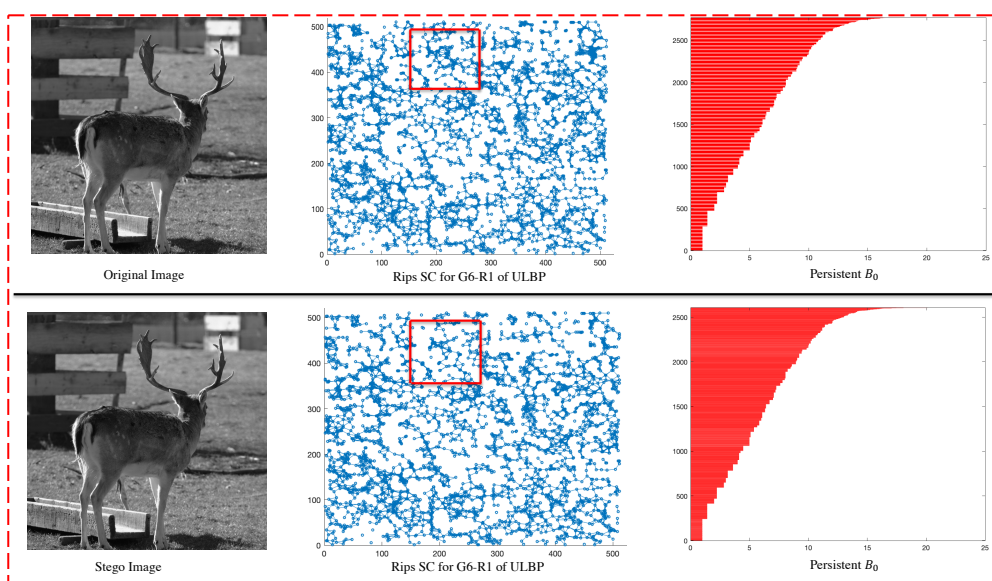

Figure 6-2: Demonstration of homological features constructed from an original image and a stego image.

Our experimental dataset consists of 1000 natural images (size 512-by-512 pixels) randomly selected from the BOSSbase database, version 1.01, which consist of 10,000 natural images [141]. Secret face biometric data are embedded inside these images to produce 1000 stego-images using the three techniques mentioned earlier which are TLSB, LSB-Witness and S-UNIWARD. The process of hiding the biometric data was done by our collaborator Dr. Rasber Rashid, at Koya University, as an expert in Biometric steganography and proposer of LSB-Witness scheme.

The classification method, adopted here, is the linear support vector machines (SVM) which works by finding optimal hyper-planes separating the input training dataset according to their classes. Approximating the optimal (if exists) separating hyper-plane is ideally the one that has a maximum distance to the nearest data samples, known as support vectors, in the training set. The goal of such optimisation method is to maximise the distance margin between the support vectors and the hyper-plane to obtain better classification accuracy.

For evaluation, we used the four different classification schemes discussed in chapter 4, i.e. Leave-one-out, 30% Training, 50% training and 70% training. In what follows, we present the classification results with these evaluation schemes.

We tested all the performance of each of the ULBP group landmark, in the same way as in chapter 4, but instead of using 100 thresholds we opted for the 5 specific thresholds $t = 4,5,7,10,15$. These were choose experimentally as the 5 best performing thresholds here. Unlike the case of morphing, here the best performing ULBP geometry is G_6 and G_3, where we demonstrate the performance of the proposed PH-based steganalysis approach for each of these ULBP geometries.

These experiments were conducted at the early stage of our research, and accordingly we are testing the performance at each single threshold rather than the full PH-based scheme. Therefore, the topological features feed into SVM is of dimension 8 each corresponds to one of the 8 rotations of G_3 or G_6 ULBP image landmarks.

Table (6-1) clearly shows that our approach is effective to detect stego-images when LSB methods, TLSB or LSB-Witness, used to hide information inside a digital image. The different training schemes increased the overall detection accuracy by

6%. For S-UNIWARD, the best detection accuracy obtained is 82% showing some robustness of this technique against our method.

Stego-image detection performance accuracy displayed in table (6-1) clearly demonstrate that, in LSB-based steganography methods, increasing the percentage of training data contributes to increased detection while this effect is less observable for the more robust hiding technique of S-UNIWARD approach. On the other hand, no one topological construction threshold is performing good across the 3 steganography techniques, see the shaded cells in table (6-1).

	DTS	T=4	T=5	T=7	T=10	T=15
TLSB (G_6-ULBP)	30% Training	86.7	84.8	78.3	74.1	67.1
	50% Training	90	87	78.7	75.1	68
	70% Training	91	87.8	78.7	75.7	68.4
	Leave-one-out	92.7	88	79.1	75.8	68.1
LSB-Witness (G_3-ULBP)	30% Training	91	86.3	90.6	84.2	90.2
	50% Training	91.8	86.8	91.1	85.7	90.5
	70% Training	92.3	87.4	91.2	86.3	90.33
	Leave-one-out	93.1	87.7	91.9	86.8	90.6
S-UNIWARD (G_6-ULBP)	30% Training	71.6	65.9	80.4	67.7	72.5
	50% Training	74	69.2	81.2	70.2	74
	70% Training	75.2	72.3	81.6	70.9	75
	Leave-one-out	76.6	73.8	82	70.8	75.5

Table 6-1: Classification Performance of PH-based steganalysis to detect stego images using G_6-ULBP landmarks.

Despite the rather small number of the images used for this pilot-like investigation, the results are encouraging and provides good evidence that topological data analysis is a promising tool to be more investigated and used as a steganalysis method in the future. There are many ways one can extend the approach discussed here such as using the number of persistent 1-dimensional holes (i.e. B_1), concatenation of persistent features extracted from the space of persistent barcodes and extracting other topological/network parameters. Also, comparing our method with other specific and universal steganalysis methods as well as testing it on other

steganographic methods too. Furthermore, the full persistent homology approach is expected to provide more insight into topological steganalysis, and perhaps expand the list of landmarks.

6.2 TDA-Guided Image Inpainting Algorithms

Image inpainting is the process of restoring missing image data in region(s) of an image to preserve continuity of its overall content and semantic, but it is also used to remove unwanted image objects. It has also been used to change image contents for many purposes including malicious ones. This section is devoted to describing the use of topological methods to improve existing digital inpainting algorithms. Although some initial investigations we carried out that TDA-approach using PH-tools can be useful in detecting malicious inpainting, we shall not discuss this issue here. The work reported in this section, was conducted in collaboration with then fellow Buckingham PhD student Dr Ahmed Al-Jaberi (currently at Basrah University, Iraq) whose research was focused on designing Partial Differential Equations for Digital image inpainting.

There are many ways one can classify the wealth of inpainting methods proposed in the literature in terms of (1) the mathematical and statistical algorithms, (2) the size of the missing regions (large missing-region inpainting algorithms verses small missing-region inpainting methods), (3) texture quantity outside missing-region, (4) domain specific inpainting algorithms (spatial verses frequency domain) and finally (4) exemplar-based inpainting (EBI) algorithms verses non-exemplar based inpainting algorithms. For detailed discussion and algorithms proposed regarding each inpainting classification scheme, we direct interested reader to see [142], chapter 2. Here, the focus is on EBI algorithms and the use of persistent homology to improve some limitations of EBI algorithms.

In general, the main difference between EBI and non-EBI algorithms is in the adopted method of information propagation into the mission region. Non-EBI algorithms propagate information pixel-by-pixel from the missing region neighbourhoods using partial differential equations (PDE). EBI approaches, on the other hand, recover the missing region by propagating textural/structural information patch (block) by patch from outside the missing region into the missing region. EBI schemes exploit the commonly accepted assumption that throughout different image

regions many patches contain similar textures/structures. The main challenge is the choice of a realistic patch similarity measure. Existing EBI algorithm rely on selecting small patches to start the process of information propagation into the missing region which can only model simple structure and texture similarities. Here, we use PH to model the topological shape of the patches surrounding the missing region by constructing Rips SC of ULBP landmarks at different distance thresholds and calculating the number of B_0 at each threshold. This topological data is input to machine learning classifiers (here SVM) to classify the patches according to high-textured (HT) patches and low-textured (LT) patches. Next, we describe the existing EBI technique and the limitations therein before proceeding to describe our topological approach to modify EBI and consequently improve the inpainted image when applying EBI.

6.2.1 Exemplar-Based Inpainting Method (EBI)

In 2004, Criminisi et al. proposed the first exemplar-based image inpainting algorithm to reconstruct image missing patches' texture and structure [143], simultaneously. The algorithm in [143] depends on the missing region reconstruction *order* of the patches, defined by a ***priority function***, that maintain the continuity and connectivity of object boundaries by propagating linear structures into the missing region before more complex texture is propagated. Unlike non-EBI techniques, Criminisi et al's algorithm proposed to recover missing region on a block-by-block approach, where they fix a block size of be 9-by-9 pixels to recover the missing region for any input image. We first need to introduce some notations. An input image I is assumed to consist of two disjoint regions; the *source* region ϕ representing the known areas and the *target* region Ω is the missing part of the image. The boundary pixel set of Ω is denoted by $\delta\Omega$. Figure (6-3), illustrate the process of EBI algorithm to recover a missing region of an image.
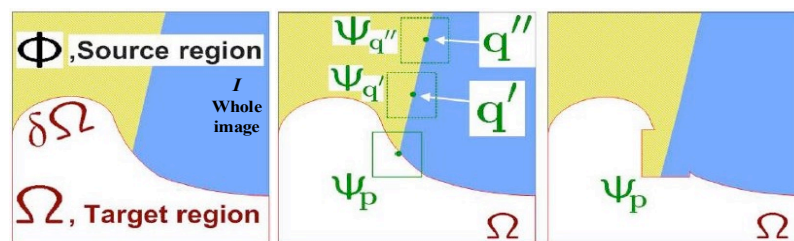

Figure 6-3: EBI process and notation [143]. Given the patch $\boldsymbol{\psi_p}$, $\boldsymbol{\partial\Omega}$ is the boundary of the target region Ω and *the* entire image is denoted with $\boldsymbol{I}$.

The priority function is a product of terms

$$P(p) = C(p)\,D(p) \tag{6.1}$$

where $C(p)$ is the confidence term and $D(p)$ is the data term, and they are defined as:

$$C(p) = \frac{\sum_{q \in \psi_p \cap (I-\Omega)} C(q)}{|\psi_p|} \tag{6.2}$$

$$D(p) = \frac{|\nabla I_p^{\perp} \cdot n_p|}{\alpha} \tag{6.3}$$

Here $|\psi_p|$ is the area of ψ_p, ∇I is a gradient of the image I, α is a normalization factor (e.g. $\alpha = 255$ for a typical grey-level image), $\nabla I_p^{\perp}$ is the isophote (direction and intensity) at point p, n_p is a unit vector orthogonal to $\partial\Omega$ in the point p and $\perp$ denotes the orthogonal operator. Note that:

- The *Data* term is a function defining the structural information for reconstructin linear structures using isophotes (flows), and hence is responsible for propagating structural information first.
- The *Confidence* term defines the reliability of information surrounding the pixels to reconstruct textural information.

Next step is to apply a matching function (e.g. Sum of Squared Distance) to find a target block that has similar structure and texture to replace the template block in the mission region. This process is repeated until the entire missing region is recovered, see figure (6-3).

The main drawback of EBI algorithm is that artifacts appear in the reconstructed image due to the incorrect selection of some blocks by the priority function resulting in initial incorrect completions and spiralling errors. This seems to be caused or exaceperated by the use of fixed 9x9 block size sespecially when the mission regions is surreounded by rich texture and structure [143]. Originally, Criminisi et al's algorithm was meant to replacing unwanted objects from images with background-like patches in a visually acceptable manner, but it doesn't work well, when removing a large object that is surrounded by rich texture [142]. Thus, EBI works well in removing small scraches from a photograph or even a large object surrounded by simple texture and structure.

There are many algorithms proposed to overcome the drawbacks of Criminisi et al's algorithm and improve the algorithm. These can be divided into two groups; the first group focused on proposing techniques to improve texture reconstruction such as [144][145][146][147][148]. The second group of work proposed to improve the reconstructed structure in mission region usning EBI , for instance [149][150][151][152][153]. For a detailed review, interested reader are referred to chapter 5, section 5.3 in [142]. Nonetheless, most of these improved methods use the same block size of 9-by-9, and to the best of our knowledge, no approach has yet addressed the block size selection in Criminisi et al's algorithm. The next section will include a topological approach to select the size of the patch propagation adaptively based on the topological quantification to measure the amount of texture and structure surrounding the missing region in a digital image.

6.2.2 Topological Exemplar based Inpainting (TEBI) Algorithm

To overcome the drawback of Criminisi et al's EBI algorithm in terms of the size of patch propagation, we use the TDA main tool of PH to reduce the amount of artifacts produced when recovering a missing region. We argue that our approach overcomes the issue of producing visible artifacts when using EBI to reconstruct a missing region whereby its surrounding area has a rich texture and structure.

Similar to the approach introduced in chapter 4, section 4.3, we build Rips SCs based on ULBP landmarks at different distance resolutions and calculate the number of conncted components (B_0) at each distance threshold for each of the ULBP geometries, and the eight rotations at each ULBP geometry. For each distance threshold, we have an 8-dimensional topological feature vector to be used for texture quantification at each distance thresholds. The rest of the following subsection is devoted to use these topological quantification to determine the appropriate patch size to propagate the information into the missing region.

6.2.2.1 *TEBI Experimental Setup and Results*

To evaluate the performance of the TEBI inpainting scheme, two datasets were constructed with a number of training-testing protocols. First, a dataset of 240 images were used to train linear SVM classifier on low-texture images and high-texture images. This set consisted of 120 images randomly selected from the google images known to be of low-texture (LT) type, and 120 images randomly selected from [154]

which are known to be of high-textural (HT) images. In figure (6-4), we show an example of low and high texture images used in our experiments.

In general, texture is not uniformly distributed in images, and our selected experimental images have different intensity of texture but the label of high/low of texture is given to an image based on the majority of image sub-regions texture. To classify texture type of an input image, five non-overlapping blocks selected randomly from each image. The size of the blocks are 25-by-25 pixels, and hence for our experiments we end up with 1200 sub-images where 600 of them are of HT type and the rest of the 600 sub-images are LT type. Four different training-testing schemes are used in our evaluation, as follows:

- 40 images (20 HT, 20 LT) for training and the rest of the 200 images for testing.
- 120 images (60 HT, 60 LT) for training and the rest of the 120 images for testing.
- 160 images (80 HT, 80 LT) for training and the rest of the 80 images for testing.
- 200 images (100 HT, 100 LT) for training and the rest of the 40 images for testing.

To determine a practical way of using TEBI, a number of parameters need to be chosen to classify image texture. The choices are: selecting the right ULBP geometry, best distance threshold to model texture and the appropriate linking of extracted topological invariant to the type of texture of the input image.
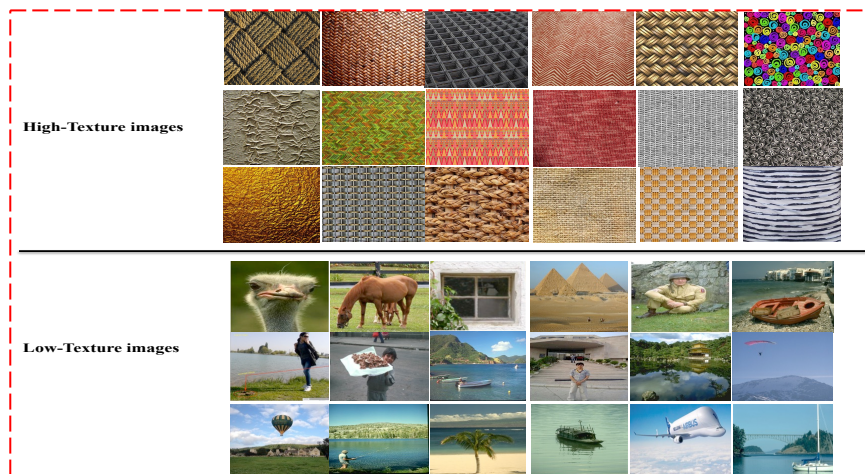
Figure 6-4: Example of High and low textural images used to test the performance of TEBI algorithm.

117

SVM classification results for the B_0-based PH scheme are presented in figure (6-5), for all the geometries of ULBP landmarks at 6 different experimentally-determined distance thresholds (T=0,3,5,7,13), and the 4 earlier defined evaluation protocols. Clearly, topological features calculated at T=10 performs better in differentiating HT regions from their LT counterparts when compared with other thresholds. Among the 7 ULBP geometries, G1, G2 and G5 are performing better in discriminating HT image regions from LT ones. Therefore, we use these geometries as candidates to quantify texture in missing regions surrounding areas and consequently select suitable patch sizes to propagate information (textural and structural) into missing region.

Figure 6-5: Topological-based Texture classification performance for different training-testing protocols.

The above charts also reveal that, different training-testing protocols do not have a big effect on the classification results, and this shows the effectiveness of the topological features on one hand and the irrelevance of training a large number of images for training.

Accordingly, an input image block/patch needs to bypass 3 checks to be classified as HT or LT image block. First, for each ULBP geometry, at least 5 out of the 8 rotations must vote in favour of LT so that an image subset labelled to be LT. Second, out of the 5 image subsets, at least 3 must vote in favour of LT for the image to be classified as LT. We follow the same procedure to classify HT image subsets. Finally, out of the 3 best performing ULBP geometries, at least 2 of them need to vote in favour of HT/LT, then the image subset will finally be treated as a HT or LT. Hence, a missing region's neighbourhood will be casted as a low or rich in texture. Following

the rules introduced here, the size of the patch propagation determined adaptively according to the following heuristic rules:

- A patch size of 3-by-3 will be selected if 3 image subsets voted in favour of HT.
- A patch size of 5-by-5 will be selected if 4 or 5 image subsets voted in favour of HT.
- For LT image subsets, select a patch size of 11-by-11 or 13-by-13 or 15-by-15 when 3 image subsets classified as LT. Otherwise, use a patch size of 21-by-21.

Original Image	Missing/Occluded Region
Reconstructed using Original EBI algorithm.	Reconstructed using Topological-EBI
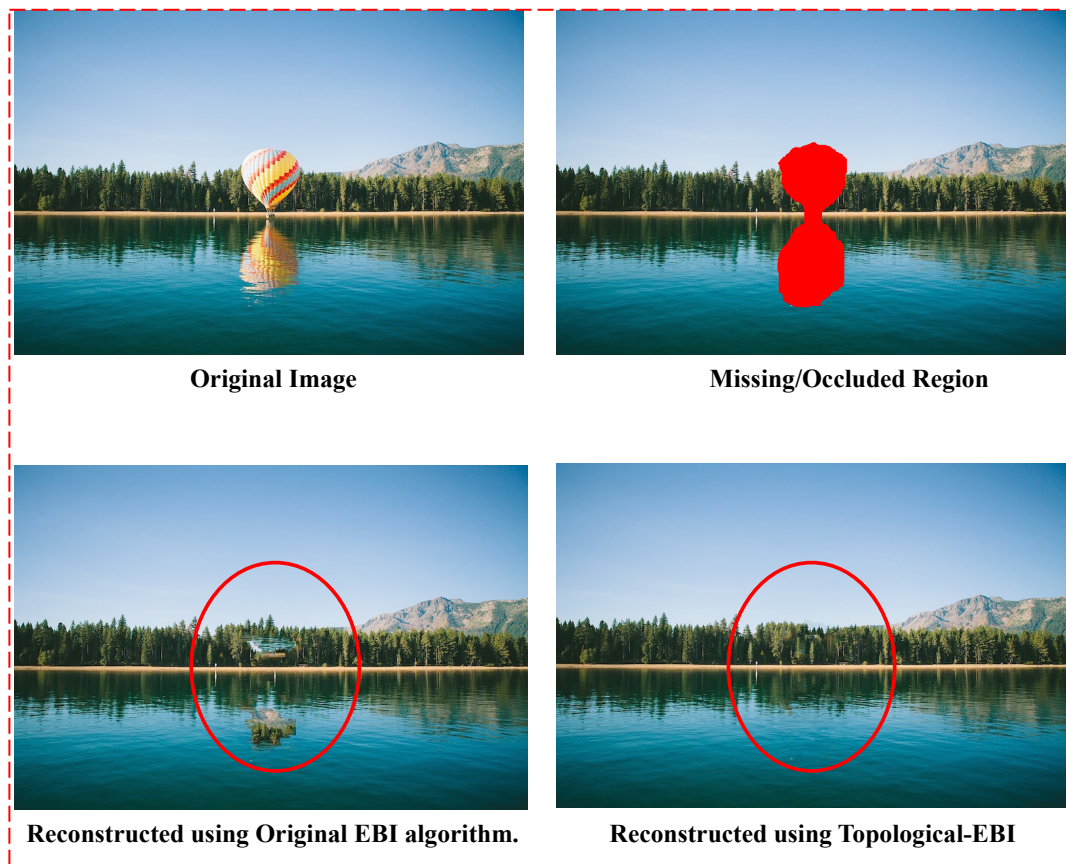
Figure 6-6: Results of TEBI algorithm applied to an image and compared the result with original EBI.

As it can be seen from the above figure, our proposed topological-EBI algorithm outperforms the original EBI algorithm, known as Criminisi et al's algorithm. The reconstructed image using original EBI suffers from uncorrelated and visually unacceptable texture and structure, see 1st column of the 2nd row in figure (6-6). This problem resolved by a large degree using TEBI in a visually acceptable manner, see 2nd column of 2nd row in figure (6-6). Furthermore, beside the original EBI, we compared our proposed TEBI approach with the algorithms proposed in [147][152] to

119

reconstruct missing region in images that vary in terms of texture and structure, see figure (6-7). More examples of applying our proposed TEBI method can be seen in [142], especially in chapter 5, section (5.5). The results demonstrated in figure (6-7) shows that our method outperforms state-of-the-art (Excluding CNN-based methods) EBI methods when the missing region is relatively large, and to reconstruct the missing region, one needs to extend the edges into the missing region. Beside modifying EBI, we also used persistent homology as an image quality assessment or assess the quality of the inpainted image.
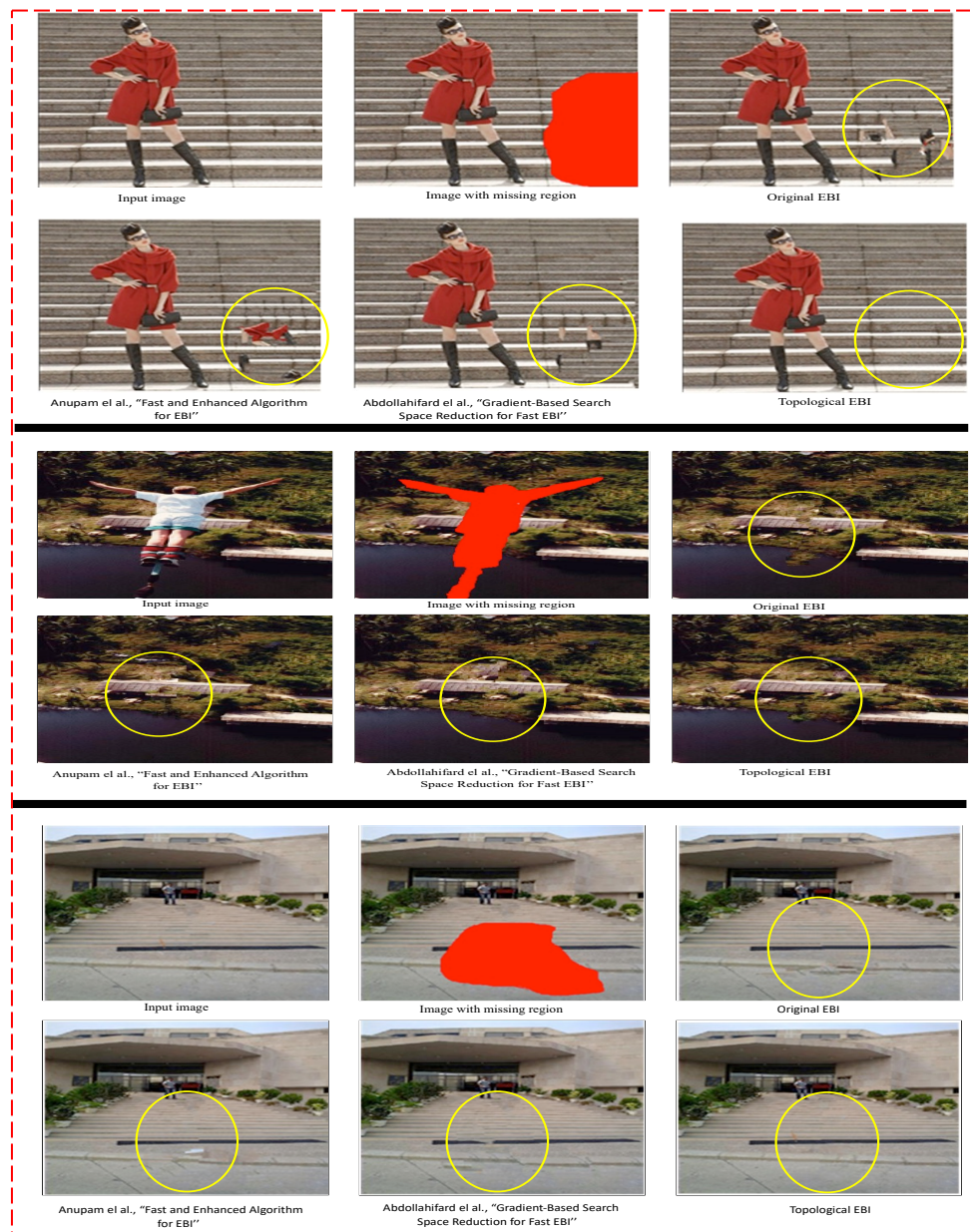

Figure 6-7: Examples of applying TEBI algorithm, and its comparison with other algorithms.

To assess the quality of inpainted images, in addition to visual inspection, in [142] (section 5..6.1) Al-Jaberi conducted a number of experiments evaluating the quality of inpainted images comparing our proposed TEBI with 3 more EBI algorithms using a number of statistical quality measurements and 5 different scenarios of missing regions. Al-Jaberi concluded that TEBI outperforms the other methods but slower than the other 3 methods to reconstruct the missing region due to the amount of computation entailed in the patch size selection and matching criteria. He also concluded that, when the surround area of the missing region has LT, then all of the 4 methods mentioned earlier are recovering the missing region successfully with very little difference in quality. Furthermore, in [142] PH has been used as a quality measurement tool to assess the topological quality of inpainted images, and concluded that TEBI outperforms the other 3 methods used in the evaluations protocols.

Finally, it is worth to mention that one of the weakness points about TEBI algorithm is that it still struggles to fully recover missing regions when there is a curved or cross-shaped structure. But the visual quality of inpainted images using TEBI outperforms Criminisi et al [143], Deng et al [153] and Anupam et al's algorithm [147]. All of the EBI methods struggle to recover missing region when there is no similarity between the structure and texture of the missing region with other regions in the rest of the image.

6.3 PH approach for Tumour Diagnoses of Medical Image Scans

Finally, in this section, we discuss the use of PH for medical image analysis. In particular, we use the same approach adopted in the case of morph detection to build PH feature vectors from images using automatic landmark selection methods and then build persistent barcodes to analyse breast cancer mammographic images. For the sake of self-containment, a brief general introduction on cancer will be given, followed by breast cancer factors and the mammography datasets we used in our experiments. Finally, experimental results of using PH to identify abnormal breast tumours from their normal counterparts demonstrated. Most of the information about the background of cancer and the breast cancer , in the next subsections, is heavily depend on the brilliant work of Taban Majeed's PhD thesis [155], especially chapter 2 and the main website of Department of Health and Human resources of USA

government in [156]. Readers familiar with general background of cancer, breast cancer and mammographic medical imaging can skip sections 6.3.1 and 6.3.2.

6.3.1 What is Cancer?

Naturally, human body cells divide and grow in a controlled way that monitored by different mechanisms in our body. The rate of cell division and growth is different from infants and adults. Normally, cells divide faster in childhood to allow the growth whereas in adults cells divide to replace lost cells as a result of injury or to replace dead cells. The process of cell division and growth which is out of control is called cancer [155][156]. The main difference between cancerous cells and normal cells is that cancer cells continue to divide without stopping while normal cells mature into unique cells with specific functionalities and stop from the division and growth. To remove unneeded cells from the body, signals will be sent to cells to stop dividing and start the apoptosis process, also known as programmed cell death. Unlike normal cells, cancer cells ignore these signals from the body and continue to divide. Cancer cells are forming solid tumours in many cases which are malignant and can spread into nearby tissues. Benign tumours, on the other hand, do not spread into neighbouring tissues, although sometimes they can be quite large in size. Cancer cells can spread to other parts of human body through lymphatic or vascular systems, known as metastatic cancer, which is the main cause of death among cancer patients. Below, we give an example of how normal cells look like versus cancer cells.
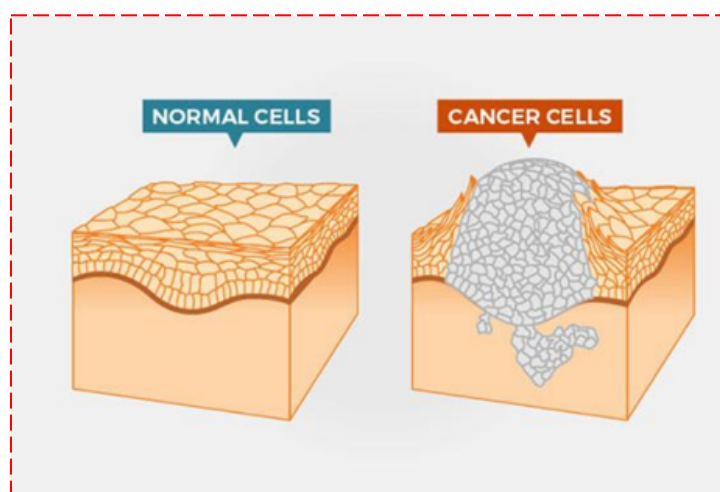

Figure 6-8: An example of Normal cells versus Cancer cells [156].

6.3.2 Breast Cancer

One of the main causes of death by cancer in UK and around the world is breast cancer. In UK alone, between 2015-2017, 11399 people died because of breast cancer [157]. This figure increases to 9.6 million deaths Worldwide in 2018. The Female breast anatomy illustrated in figure (6-9).


Breast profile	
A	Ducts
B	Lobules
C	Dilated section of duct
D	Nipple
E	Fat
F	Pectorals major muscle
G	Chest wall/rib cage
Enlargement	
A	Normal duct cells
B	Basement membrane
C	Lumen (centre of duct)
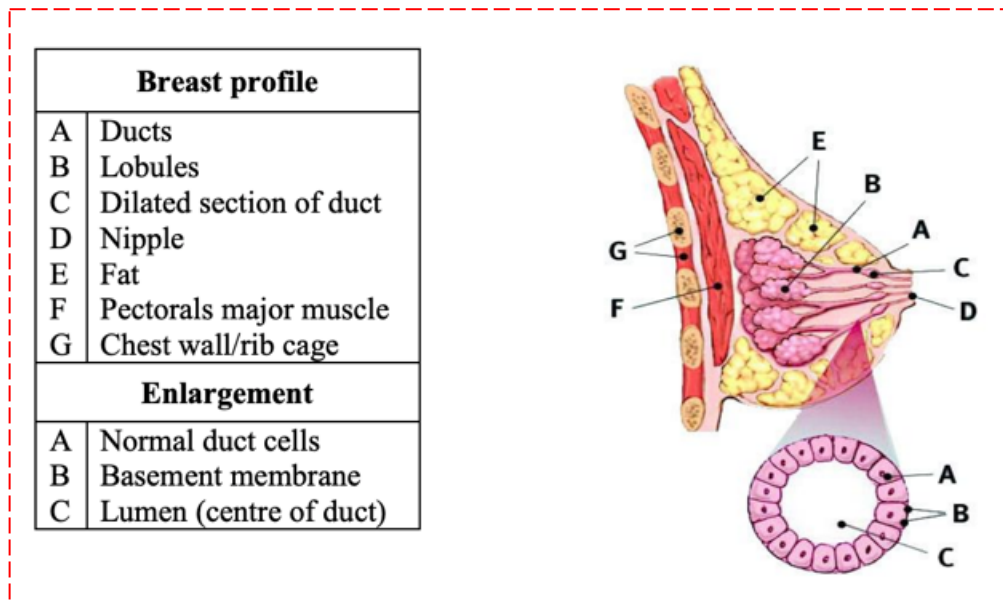
Figure 6-9: Anatomy of part of female breast [155].

As it can be seen from the above figure, female breast constituted of lobules (milk producing glands), ducts (carriers of milk from lobules to nipple) and stroma (the tissue surrounding the lobules and ducts). Cancers caused by lining the duct cells are called ductal cancer while lobular cancers are affecting the lobules cells. In general, breast tumours can be classified into 3 main groups; benign, in situ and invasive tumours. Benign tumours are abnormal cells but unable to spread to surrounding tissues and can be left untouched if they are not creating any complications. Majority of breast tumours detected by mammography are of benign type. In situ tumours are the early stage of invasive cancer and has the potential to become invasive. In this type, the cancer cells are still in the duct or lobule and not spread to the basal membrane. For early detection of in situ tumours, American Cancer society recommends clinical examination between the age of 20 to 39, every 3 years. After the age of 40, it recommends conducting annual mammography screening to prevent invasive tumours. Finally, invasive cancer is the final stage where the cancer cells broken the basal membrane.

There are many factors causing invasive cancer such as family history, genetic issues, race, obesity, geographical location, exposure to radiation and others. In all cases, the success of cancer treatment depends heavily on the stage/time the cancer identified.

There are many imaging techniques developed over the years for the purpose of cancer detection in general, and breast cancer in particular. For example, mammography, X-ray, ultrasound and Magnetic Resonance Imaging. Mammography is one of the imaging techniques widely deployed for the early detection of breast cancer. Digital mammography is a special type of X-ray that have many advantages over tradition mammography filming and in comparison, with other digital techniques. Breast screening using digital mammography (1) takes less examination time, (2) low cost (compared to MRI), (3) easy storage and (4) can be transmitted to other health professionals easily. We direct the interested reader to [155], chapter 2, section (2.2) to section (2.2.4) for a detailed discussion about mammograph image acquisition, object identification using mammographs and mammogram projections. An example of breast images acquired by mammograms is shown in figure (6-10).

Reading and analysing mammograms is not an easy task for radiologists. Among the difficulties face radiologists are low resolution of breast cancer mammograms, location and size of the lesion within the breast cancer tissue. Age of the patient is another factor which makes breast cancer detection to be a difficult task for radiologists due to the dense breast tissues in young patients. According to statistics 30% of breast cancers are undetected [158], and hence in many cases at least two radiologist read the same mammogram to reduce rate of undetected cases. Major drawback of double-reading is the cost and workload on radiologists and sometime two different radiologists assess the same breast cancer mammogram differently especially when the size of the region of interest (ROI) (i.e. lesion) is small [158]. Instead of using a radiologist as a second reader and assessor, computer aided detection (CAD) systems are used as a second reader but the final decision on the case will be made by the radiologist. Image processing procedures will be used by CAD systems to analysis breast cancer mammograms to help early detection of breast cancer and consequently increase survival rate among breast cancer patients. In general, image processing procedure for medical image analysis include, but not limited to, noise removal, segmentation, object and abnormality detection, feature extraction and classification.

6.3.3 TDA based Mammogram Image Analysis

In this section, we use TDA to differentiate benign breast tumours from malignant breast tumours using breast mammogram scan images by constructing Rips complexes for mammograms pixel landmarks at different distance thresholds, i.e. $t = 1,2,\dots,100$. The image landmarks method used here are again chosen from the ULBP geometries, and persistent homology features associated with these landmarks are extracted before feeding into KNN classifier. The hypothesis behind treating cancer as a form of tamper detection is that one expects that cancer cells tamper with and distort the naturally occurring texture and structure of human body cells. The images we use are pre-processed images that contain the ROI only and the images (from both datasets, which will be discussed in the section) are provided by Dr. Taban Majeed (Lecturer at Salahaddin University, Kurdistan Region, Iraq) who was also a fellow DPhil student of Buckingham, School of Computing. We show an example of constructed Rips complex for a benign and malignant tumour in figure (6-10) and figure (6-11).

In what follows, we introduce the two databases use in our evaluation of the use of TDA/PH for the detection of abnormality in breast mammograms as well as the evaluation measurements. In short, we use the same approach used to detect morphing in chapter 5.

6.3.4 Evaluation Measurements and Database Description

In this section we evaluate the performance of our proposed PH-based approach, by following the traditional practice of clinicians who use the statistical measures of sensitivity, specificity and accuracy defined as follows:

Sensitivity: is the rate/proportion of breast cancer patients (having malignant tumours) truly classified as patients of having breast cancer, and is determined as follows:
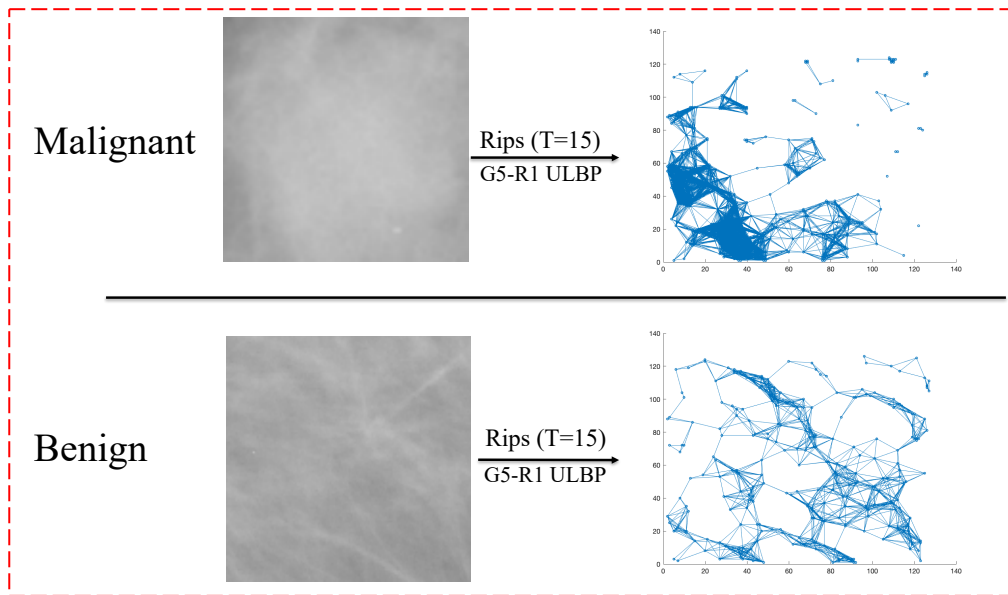
Figure 6-10: Rips complex constructed using G_5-R1 of ULBP for benign and malignant case of Mini-MIAS dataset.
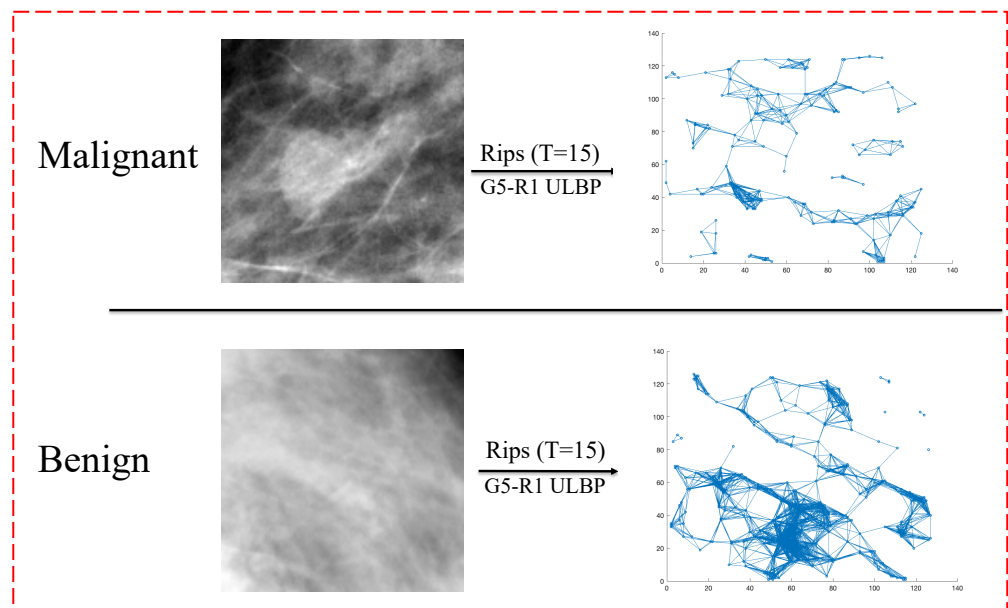
**Figure 6-11:** Rips complex constructed using G_5-R1 of ULBP for benign and malignant case of DDSM dataset.

$$Sensitivity = \frac{True\ positive}{True\ positive + False\ negative}$$

where True Positive (TP) refers to cancer patients truly identified as patients having breast cancer positively, False Negative (FN) is the breast cancer patients misclassified as negative of having breast cancers.

Specificity: is the rate of correctly classifying patients negative of breast cancer, and is determined as follows:

$$Specificity = \frac{True\ negative}{True\ negative + False\ positive}$$

where true negative (TN) refers to number of truly classified women clear of the breast cancer and false positive (FP) means the number of cases wrongly classified as breast cancer positive which in face are clear of having cancer.

Accuracy: is the overall true performance rate of the CAD system on predicting the cases presented to it, and is determined as follows:

$$Accuracy = \frac{TP + TN}{TP + TN + FP + FN}.$$

The above evaluation measurements have been computed on images from two different mammogram datasets which are widely used and publicly available. The first one is called Mini-MIAS dataset [159], which refers to Mini Mammographic Image Analysis Society. The second dataset is known as DDSM [160], where DDSM stands for Digital Database for Screening Mammography. A number of benchmarking mammographic datasets are available for experimental purpose in which they vary according to certain pre-defined criteria like type and structure of the digital mammogram, dense, fatty or glandular tissues, noise level in the images and the number of benign and malignant cases in these datasets. We opt to use Mini-MIAS and DDSM due to the fact that images in both datasets captured in uncontrolled conditions, images contain sufficient noise and low-resolution images.

Mini-MIAS contain 322 digital mammographic images (113 Abnormal, 209 Normal) of breast that contain fatty , dense and granular cases [159]. In addition, Mini-MIAS contain different types of abnormalities such as calcification, ill-defined masses, architectural symmetry and distortion. In figure (6-10), examples of mammogram images in Mini-MIAS dataset illustrated. DDSM dataset, on the other hand, contains 2620 mammogram images where 512 images selected randomly in our experiments, 302 normal cases and 257 abnormal cases. All of the images are cropped ROI of size 128-by-128 in both datasets. Further details about these datasets can be found in chapter 2 of Taban Majeed's doctoral thesis in [155], publicly available at

127

Finally, to evaluate our PH-based method to differentiate benign tumours from malignant tumours, we used the same classification schemes used in previous chapters, i.e. 30%,50% and 70% of the data used for training KNN classifier respectively and the rest of the images used for testing.
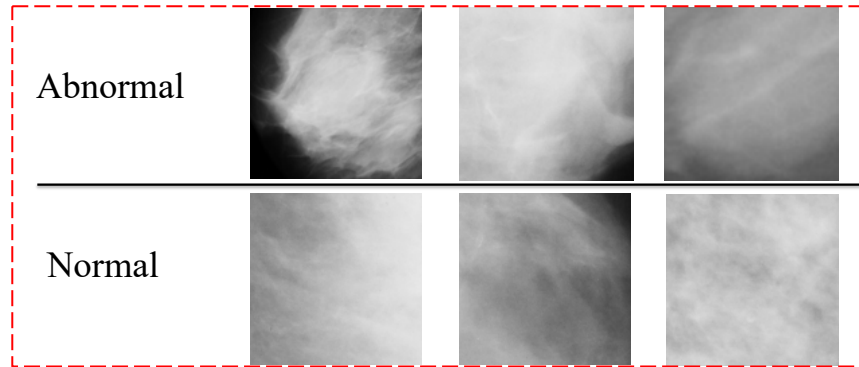
Figure 6-12: Examples of ROI for Normal and Abnormal cases from Mini-MIAS dataset.
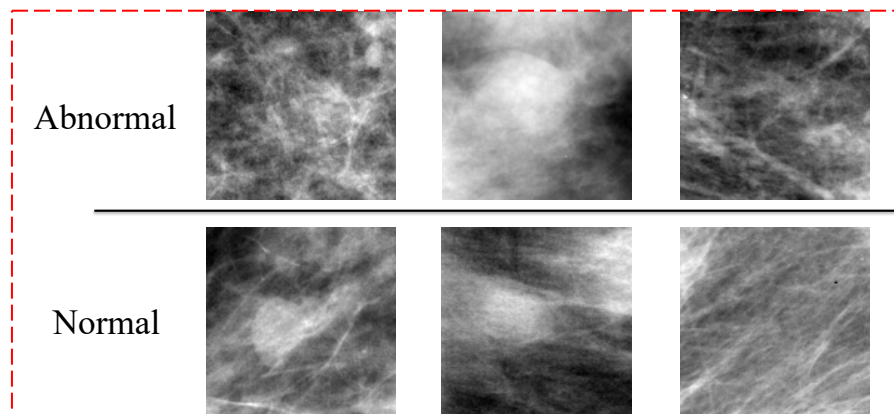
Figure 6-13: Examples of ROI for Normal and Abnormal cases from DDSM dataset.

6.3.5 PH-based Breast Cancer Detection – Experimental Results

For each image in Mini-MIAS and DDSM dataset, we construct Rips complexes based on ULBP landmark selection at an increasing distance threshold starting from $t = 1$ to $t = 100$, this process repeated for each ULBP rotation and for each ULBP geometry. At each threshold t, we calculate the number of connected components and 1-dimensional holes (i.e. B_0 and B_1 respectively) where this information is later stored in a form of persistent barcode. Next, the space of persistent barcodes vectorised using the persistent binning yielding a topological feature vector which has dimension 100 for a single rotation of any ULBP geometry. We then concatenate the

topological feature vectors of the 8 rotations of each one of the 7 geometries of ULBP, and hence ending up with a topological feature vector of dimension 800 which will be feed into KNN classifier.

The results obtained using KNN (k=1) with the topological features extracted from mammogram images are reported in table 2 and table 3. In particular, the results obtain using persistent B_0 for both Mini-MIAS and DDSM datasets can be seen in table 2, whereas table 3 is showcasing the results obtained using persistent B_1.

Dataset	DTS	Sensitivity	Specificity	Acc
Mini-MIAS (G_5)	30%training	84.076	97.568	92.831
	50%training	85.661	98.038	93.706
	70%training	86.5	98.095	94.031
DDSM (G_5)	30%training	62.378	65.346	63.98
	50%training	64.609	68.437	66.681
	70%training	66.416	71.011	68.905

Table 6-2: Classification Results of Persistent **B_0** to differentiate Benign tumours from malignant tumours.

Dataset	DTS	Sensitivity	Specificity	Acc
Mini-MIAS (G_3)	30%training	82.051	97.185	91.871
	50%training	84.268	97.596	92.931
	70%training	85.824	97.857	93.639
DDSM (G_7)	30%training	62.289	71.404	67.222
	50%training	61.688	73.846	68.274
	70%training	82.727	75.007	78.548

Table 6-3: Classification Results of persistent **B_1** to differentiate benign tumours from malignant tumours.

Table (6-2) clearly shows that the number of persistent B_0 performs well for the Mini-MIAS dataset in differentiating benign cases from malignant ones. We note that the sensitivity rate is lower than specificity, meaning that the number of detected malignant cases is lower than the number of benign cases. However, increased training images results in increased detection rate of malignancy by about 3%. Unfortunately, table (6-2) also shows that the PH-based approach in detecting malignant tumours in DDSM dataset is not as good as in the Mini-MIAS dataset. Increasing the number of images in training to 70% still not boosted the overall classification accuracy to above 70%. But similar to Mini-MIAS, the sensitivity rate is lower than specificity.

Table (6-3), on the other hand, shows the classification performance of KNN using persistent B_1 as the input feature. Again, the persistence of B_1 topological features performs better on Mini-MIAS dataset than DDSM dataset. The performance of persistent B_1 is very close to the results obtained using persistent B_0, and hence shows the strength of the number of 1-dimensional holes to detect malignant tumours. The only difference is that it is not the same geometry of ULBP that performs good, whereby in the case of using persistent B_1, it is the G_3 of ULBP that performs best among the 7 geometries of ULBP landmarks of Mini-MIAS dataset. In DDSM dataset, the best performing geometry is G_7 when persistent B_1 is used as the input topological feature to KNN. But interestingly, the overall classification accuracy increased by 11% when the image percentage used in the training increased from 30% to 70%. Furthermore, the sensitivity rate is 82% when 70% of the data is used to train KNN classifier, and this indicate the discriminative power of persistent B_1 to be consider among different datasets. Note that we are only reporting the results of best performing geometry among the 7 ULBP geometries for both B_0 and B_1 persistent features as well as the both datasets used in our experiments. In this vein, for Mini-MIAS dataset the second and third best performing ULBP geometries are G_3 and G_4 when B_0 is used as the topological features and G_4 and G_6 in DDSM dataset. In the case of using persistent B_1, second and third best performing geometries are G_4 and G_6 in Mini-MIAS dataset and G_3 and G_5 in DDSM dataset.

Finally, the analysis presented in this section demonstrated the usefulness of using our approach of PH-based classification to differentiate malignant breast tumours from benign breast tumours. The performance is not consistent across the two datasets used in our experiments and hence needs further improvements. However, the inconsistent performance can be investigated by using the Mapper in the same way we discussed in chapter 5. Moreover, the high performance with one of the databases is an incentive to mitigate the inconsistency by conducting more investigation with other types of landmarks, combining the two Betti numbers B_0 and B_1, and deploying other local topological information such as local persistent homology and degree distributions, for improved and consistent classification techniques in future.

6.4 Summary

In this chapter, we tried to investigate the viability of extending the use of TDA in other image analysis applications or to help with improving certain image processing/enhancement tasks. The results of 3 case studies were presented on the potentials of using TDA and its PH tools in diverse areas of image applications. Although, these cases differ fundamentally in their practical use including multi-media security, image reconstruction with its variety of applications, and biomedical image diagnostics. What is common in these applications is the nature of image distortions being difficult to visualise change to the spatial distribution of certain localised textural primitives. These 3 diverse cases have therefore the viability of topological data analysis approaches to these and potentially many more image processing/analysis applications whereby the spatial distribution of groups of textural primitives become sensitive to minute changes. In all cases, we noted great potentials for using the full benefits of PH-based tools, but due to time constraints we defer such a research work on other applications and deeper analysis for future consideration.

Chapter 7

Conclusion and Future Directions

7.1 Conclusions

Digital image analysis is one the most active fields of research nowadays due to many factors including the rapid increase in the availability of cheap and powerful devices to produce images like mobile phones, the popularity of social media platforms for real time share media objects, and the emergence of advanced machine learning and Artificial intelligence tools. At the core, image analysis algorithms attempt to develop application-dependent quantitative measures that can be used to distinguish between images in terms of content, class labels, appearance of anomalous events/objects. Machine learning algorithms for image analysis, often work by learning a model to represent the distinct groups of images for a sufficiently large sample, and decisions are made about new images in terms of the differences between the quantitative measure of the input image and those of the members of the different labelled groups in the learnt model. For simplicity, these differences in the quantitative measures are referred to as distortion, even when the input image is not obtained from an existing sample by image distortion. There are many reasons behind the appearance of digital image distortion, (1) harmless (e.g. beautification filters) or malicious (e.g. morphing) (2) natural (e.g. body cell texture distortion) or artificial (e.g. steganography and morphing). Designing tools to effectively analyse the quantified distortion data for the above, or other, image analysis applications is very challenging.

The research work in this thesis was devoted to investigate the effectiveness of the newly developed tool of *persistent homology* (PH), which is mainly depend on algebraic topology, to analysis different type of digital image tampering. Existing, and most commonly used, topology-independent machine learning algorithms for image analysis learn quantitative models of one or more image texture and do not pay attention to the spatial distribution of the significant texture. Emerging TDA-based image processing/analysis algorithms, on the other hand, aim to build sequences of topological (Simplicial or cell complex) representation at different level of levels and

132

analyse the persistence nature of certain homological invariants (e.g. Betti numbers). Most existing PH-based image analysis schemes are constructed through intensity-based filtration with no specific attention to texture features. The initial observations that the spatial image texture primitives are often sensitive to malicious tampering or naturally occurring changes, incentivise our work to develop a new image analysis strategy that fuses the TDA approach with the conventional texture analysis approach. The distinctiveness of our new approach is that it constructs sequences of simplicial complex representation of images in terms of automatically computable texture-based landmarks, and the corresponding PH features are extracted using distance-based filtrations. This approach allows the development of a large number of TDA-based image analysis schemes.

The stated aim and objectives of this thesis was to (1) use PH to design new and effective image tampering detection tools to address the malicious problems occur as a result of tampering such as morphing detection, steganalysis, cancer detection and low-level image texture quantification. (2) Develop a simple, yet effective approach to vectorise the space of persistent barcodes to develop PH-based tamper detection tools. (3) Design novel image landmark selection methods that are both effective and automatic and (4) finally test the performance of PH-based image distortion analysis tools on a large image database that downloaded from different sources.

The achievements of our work can be summarized as follows:

1- We proposed 4 techniques to select texture image landmarks to construct Rips complexes and compute the persistent homology feature representation of digital images. The 4 landmark selection methods are: Local Binary Patterns (LBP), 8-neighbour superpixel (8NSP), Radial local binary patterns (R-LBP) and center-symmetric LBP (CS-LBP). Experimental investigations revealed that using LBP and constructing the B_0 (i.e. the number of persistent connected components) barcodes, can detect up to 99% of morphed images in the Utrecht DB, up to 86% in London DB and 98% of Print-scanned morphed images. The performance of B_0 schemes for the 8-NSP, R-LBP and CS-LBP landmarks for morph detection in the Utrecht DB achieved 99%, 96% and 92% overall accuracy, respectively. For the London DB, the performance is lower than that of Utrecht DB whereby the overall accuracy of morph detection performance is 86%, 84% and 78% for 8-NSP, R-LBP and CS-LBP, respectively. The inconsistency of accuracy of morph detection between the

two datasets were shown to be due to significant differences in the way these databases were built. Apart from 8-NSP, building Rips complexes and computing persistent B_1 based on the other 3 landmarks have been shown to yield similar morph detection rates to using B_0. To some extent this shows the strength and robustness of our approach (using either B_0 or B_1).

2- We proposed to vectorise the space of persistent barcodes using an approach known as persistent binning (PB), in two forms: (1) at each PB-value, concatenate the homological invariants computed over different subsets (i.e. rotations) of landmarks (chapter 4); and (2) fuse the entire PB-values of the persistent barcodes of all rotations of the selected landmark technique (Chapter 5). Advantages and disadvantages of both approaches discussed in detail in Chapter 4 and Chapter 5 respectively by testing on a large set of face images to design effective morph detection tools.

3- Beside persistent homological invariants in dimension zero (B_0), we also used persistent homological invariants in dimension one (B_1) to analysis different image tampering problems such as morphing and breast cancer detection. As before, in many cases the performance of B_1 is similar to that of B_0.

4- Our PH-based morph detectors are shown to be very effective to differentiate fake faces from their genuine counterparts across different datasets. Beside overall accuracy of PH-based morph detection tools, the rate of false positives (genuine faces misclassified as morphs) and false negatives (morphed faces misclassified as genuine) are acceptable or comparable to other face morph detection techniques which are not based on PH.

5- Earlier results on morphing detection motivated us to go further in our investigation beyond morphing to investigate the PH-based approach on other types of image processing/analysis applications. We proposed topological methods to detect stego-images, improve exemplar-based inpainting technique, breast tumour classification using mammograms and finally used as a general image quality assessment tool. In steganalysis, homological invariants showed to be effective to detect stego-images without prior knowledge of the steganographic methods used to hide the secret message. Incorporating PH into exemplar-based inpainting algorithm improved it to become state-of-the-art and outperform all other exemplar-based inpainting approaches. Results are not consistent when we used PH to differentiate

benign breast tumours from malignant breast tumours on two different mammogram datasets. Using Mini-MIAS dataset, PH invariant at dimension zero and one achieved up to 94% accuracy while on DDSM dataset the highest achieved accuracy is 78% which is obtained using homological invariant at dimension one. As for the quality assessment, PH proved to be very effective to quantify the quality of face images under different illumination conditions such as shadow and blurring.

Success in conducting the research investigations of the kinds reported in this thesis, requires the availability of efficient easy to use software to compute the various topological parameters and display the outcome in a manner to facilitate developing hypotheses as well as demonstrating the conclusions that the researcher promote. Although, various elements of the necessary TDA computations are available but no integrated software is publicly available. Throughout the period of my program of study, I initiated such a task in collaboration with ex-colleague (Dashti Ahmed Ali, a professional software developer in Ontario-Canada) from Koya University, Iraqi-Kurdistan. The software is entitled "DAAR Topology" and the current version is a stand-alone application that works on Mac, Windows, and Linux operating systems. The software has an interface, which provide the user with a number of facilities in relation to TDA – based computations on image analysis. In Figure 7-1, we show few screenshots of the software interface as examples of the work-in-progress.

The interface enables the user to select a passport-like face image, and then using the dlib library we automatically extract and crop out the frontal face. Then the user has the choice of selecting landmark methods, and their corresponding geometries and rotations. Next, the user has 5 options of visualization which are: Barcodes in dimension 0,1 and 2 as well as the Rips complexes. Also, there is an option to visualise Persistent diagrams in dimension 0 and 1 on the same plot.

In future, we want to expand this to include Medical image analysis, Steganalysis and general image texture analysis. Furthermore, we aim to include the prediction section whereby based on the face images we have, we train KNN classifier to be ready and predict the label of the input face to be genuine or fake, but first we need to gather a larger number of genuine face datasets which are more diverse and only then this section will be activated.

Finally, we also plan to include a section in the software that enables the user to input a folder of face images and the software extract topological invariants, of the selected landmarks, of all the images in that folder and output a matrix of topological features ready for further analysis. This step is important to researcher whom want to do experiments on a large number of face/medical images. More work needs to be done in the future before releasing the software.
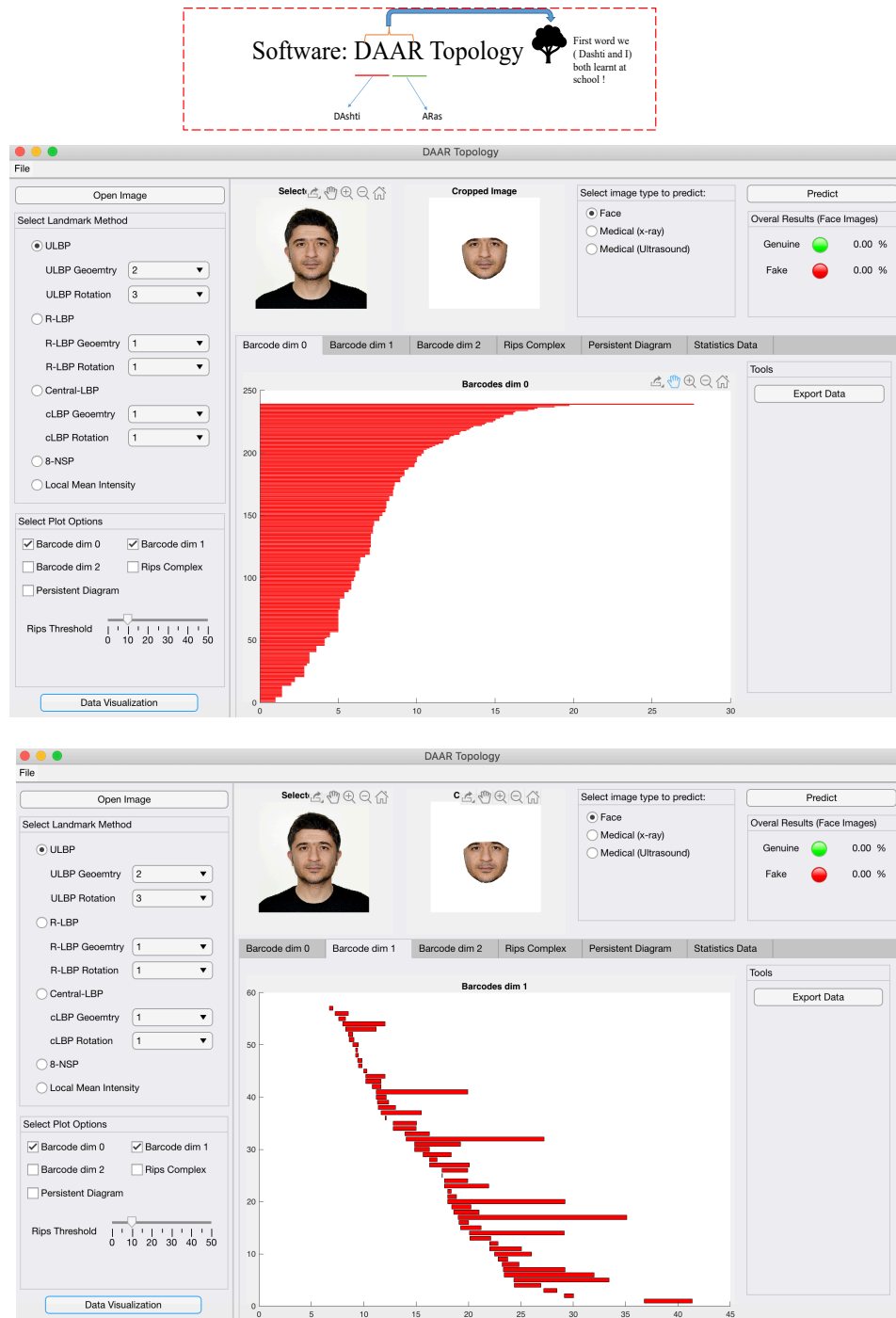

Figure 7-1: Snapshots of DAAR topology software**.**

7.2 Future Challenges and Related Work-in-Progress

The research work reported in this thesis demonstrated the applicability of persistent homology for different image tampering detection problems such as morphed face detection, steganalysis, medical image analysis and image quality assessment. However, this work has proved to be an open-ended project to develop a new innovative TDA-based strategy for image analysis in a diverse range of applications. It is unrealistic for a PhD project to complete a substantial amount of research tasks. The significant successes achieved in the limited set of applications, revealed the potential for many more contributions to deal with a variety of challenges. In the closing part of this chapter and thesis we shall highlight below a list of few potential research directions that need to be explored in future:

1- During the writing up stage of this thesis, DeepFake video and image generation have emerged as a serious threat which cannot be ignored especially when the quality of produced fake videos are becoming convincingly better. Image/video tampering is becoming an easy task due to openly available models of Convolutional autoencoders and generative adversarial networks (GAN)s. The smartphone application *FaceApp* produces visually seamless and realistic face image manipulation [161] allowing change of hair style, age, pose, gender and other attributes. *DeepFaceLab* [162], is another freely available desktop application whereby users can create DeepFake videos using sufficient image frames of both original and target individuals. Since DeepFake videos are so realistic (if trained well), they can be used for the purpose of revenge-porn, fake news, creating fake celebrity pornographic videos, fake surveillance videos, misleading court when videos/image are used as the only evidence. We refer the reader to [163][164] for detailed explanation of how DeepFake works. These tools and algorithms have not been intended for these purposes, but to deal with some useful applications. While technology cannot be de-invented, we need to develop strategy to limit their misuse, and here we report on a pilot study we recently conducted to show that TDA-approach with its PH tools can make a useful contribution.

As with the case of morphing attacks, one expects that DeepFake procedures have the effect of distorting some texture features in the original face region in

some if not all video frames. In order to determine whether our PH morph detection schemes are capable of detecting DeepFake videos, our small pilot study is based on 20 videos (10 deepfake videos and their corresponding genuine sources downloaded from the internet). From each video, we selected a frame where the face is in a neutral (or near-neutral) state and cropped out the frontal face region and changed into grayscale. We investigated the ability of a small set of 2ULBP landmark to generate PH feature vectors that can easily distinguish between DeepFake and genuine videos. The outcome confirmed the viability of using the PH tool to detect Deepfake videos. For example, we found that the number of B_0 computed from first, fifth and sixth rotation of G_2 of 2ULBP landmarks clearly detected deepfake videos from their genuine counterpart. Here, the feature vector consists of 3 number as follow:

$$f = \left(B_0 \left(R_1 \right), B_0 \left(R_5 \right), B_0 \left(R_6 \right) \right)$$

where R_1, R_5, R_6 are 1st, 5th and 6th rotations of G_2 of 2ULBP. This can be easily seen by depicting this feature vector in 3D at an increasing sequence of thresholds, see Figure 7-2 and Figure 7-3.
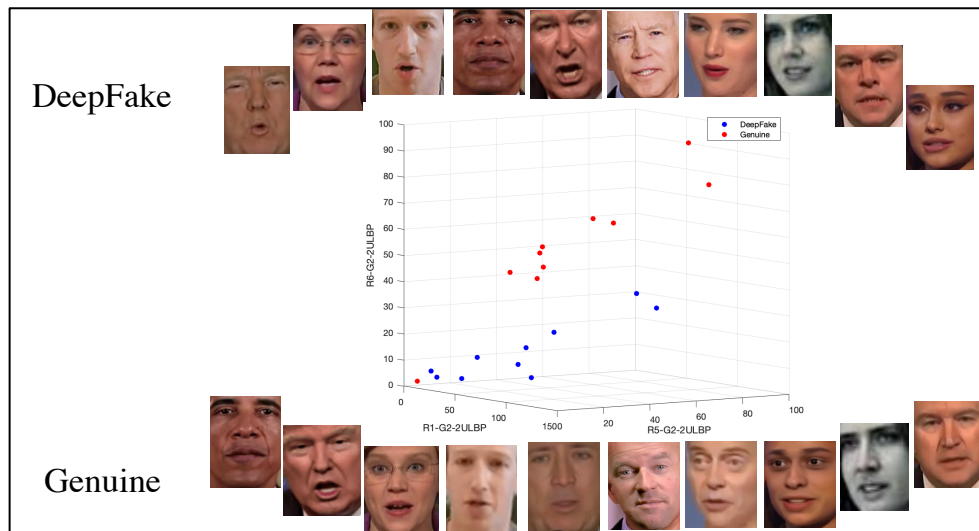

Figure 7-2: 3D plot of B_0 features for 1st , 5th and 6th rotation of G$_2$ of 2ULBP where each is representing coordinate. It can be seen that there is a clear discrimination between deepfake produced faces and genuine faces.
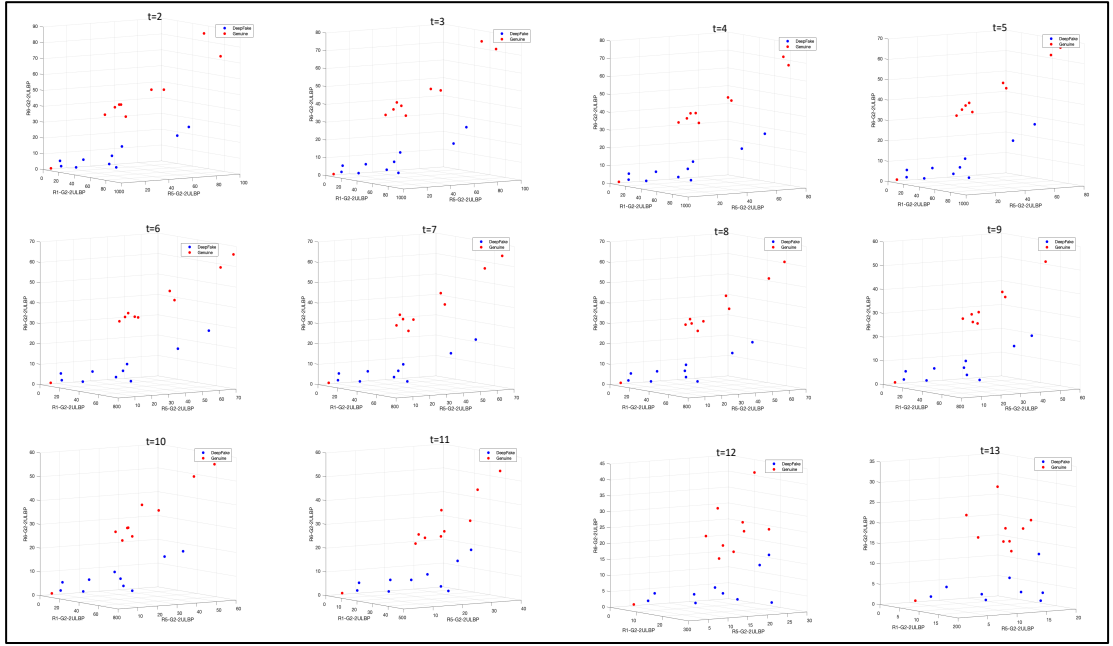
Figure 7-3: 3D plot of B_0 features for 1st , 2nd and 3rd rotation of G_2 of 2ULBP where each is representing coordinate. It can be seen that there is a clear discrimination between deepfake produced faces and genuine faces across different thresholds of building Rips complexes.

Next step in this direction, is to try to show credible evidences on the validity of the concluding hypothesis from this small pilot by expanding the PH-based deepfake detector, presented here, and test performance on a significantly larger dataset of deepfake videos. Furthermore, we should extend this work and vectorise the space of persistent barcodes, beside our developed concept of persistent binning to investigate the use of other approaches proposed in literature such as persistent images [64], persistent landscapes[63], persistent paths and signatures [63] and extracting statistics such as average of birth of bars, average of death of bars etc. In our future work, we shall compare the classification performance of our binning approach with the persistent barcode vectorisation approaches mentioned earlier, and the possibility of concatenating homological features of two or more methods together to analyse different image tampering problems.

2- The topological analysis in this thesis contained the number of connected components and the number of 1-dimensional holes (loops) which are calculated using different image landmarks. The input is a 2D grayscale image whereby the natural approach is to consider computing zero- and one-dimensional homological invariants. In our future work, we shall model the 2D grayscale image to be considered for the computation of 2-dimensional homology invariant known as the number of cavities (or voids). To achieve

139

this, we treat pixels 2D positions (indices) as xy-coordinates and the pixel value intensities as the z-coordinates. Below we illustrate an example of the new face model where we plan to include in our future investigation to compute homological features in dimension 0,1 and 2.
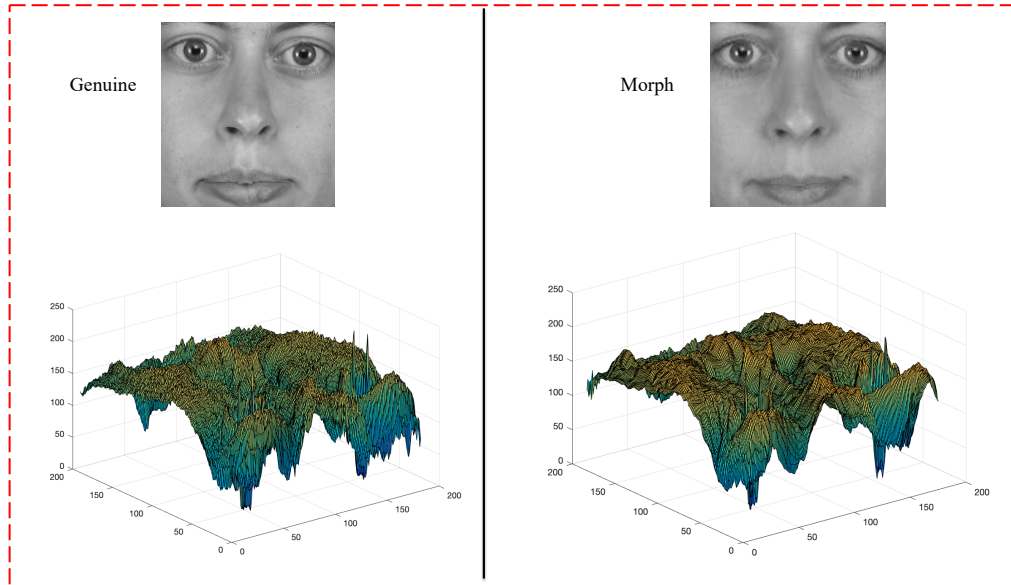

Figure 7-4: New face model to construct topology from face images and compute cavities for both genuine and morphed faces.

3- Accuracy Trend (Persistent Classification): another in progress investigation is to examine the effect of increasing the dimension of topological features feed into KNN classifier. In other words, at $t = 1$ we compute homological invariants of constructed Rips complex for the 8-rotations of 2ULBP codes which result in 8-dimensional feature vector. Adding to it topological features computed as $t = 2$, we obtain a 16-dimensional topological feature vector, and record the classification performance for each t. The reason behind this process is to see whether adding more topological features boost the classification performance or not? At this point, we want to remind the reader that in Chapter 5, we concatenated all of the computed topological features from $t = 1$ to $t = 100$, resulting in an 800-dimensioanl features vector. The reason we decided to stop at $t = 100$ is to make sure that all of the images reaches 1 connected component. But in practise, this might not be necessary and beyond some threshold, the classification performance will not increase if not decrease. In what follows, we shall present some limited amount of work in this direction, but a much more intensive study would be very useful.

140

Using ULBP as our landmark to start with and the two face image datasets of Utrecht and London DB and their corresponding generated morphed faces using splicing, complete and combine approach. We concluded that beyond $t = 30$, we are not going to gain any classification gain.
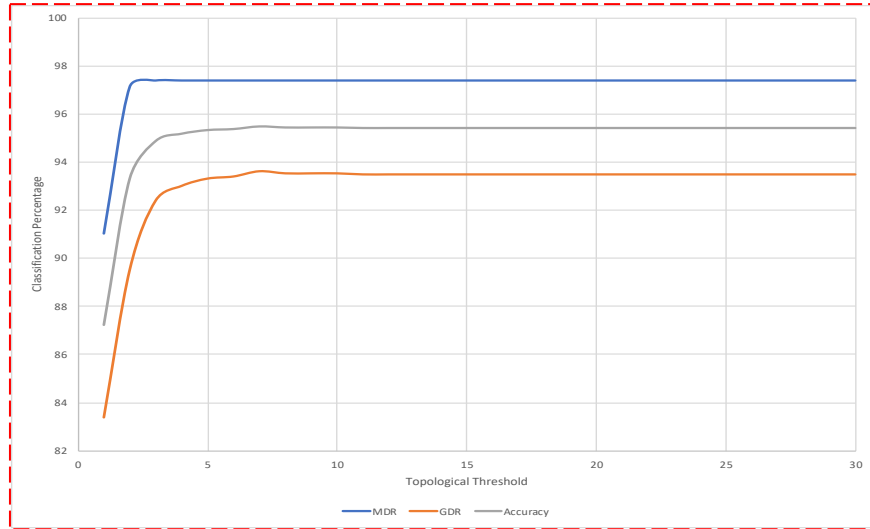

Figure 7-5: Accuracy Trend of splicing-Utrecht DB that shows the effect of increasing topological features at **dimension zero.**
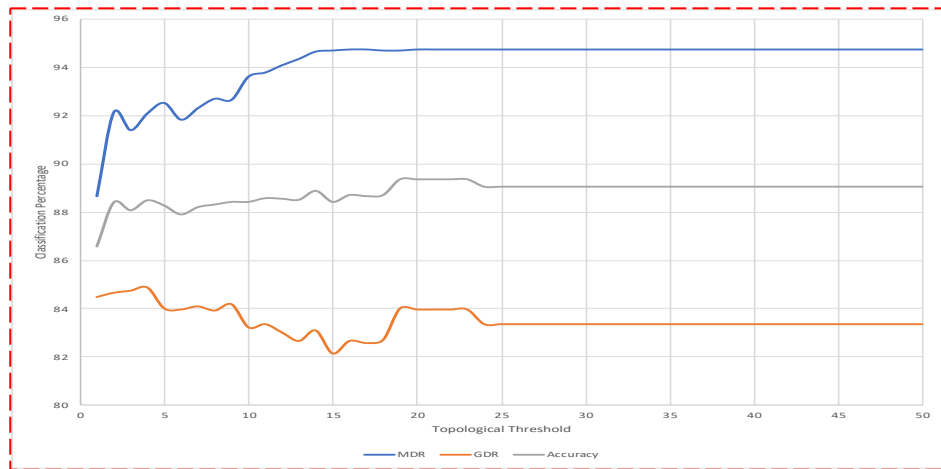

Figure 7-6: Accuracy Trend of splicing-Utrecht DB that shows the effect of increasing topological features at **dimension one.**

In figure (7-5) and figure (7-6), MDR and GDR refers to the morph detection rate and genuine detection rate, respectively. The higher the MDR and GDR are, the higher the overall accuracy. MDR and GDR are calculated similar to sensitivity and specificity, defined in Chapter 6 (section 6.3.3), where positive refers to an image being morphed, and negative is genuine. Figures (7-5) and (7-6) clearly shows that beyond $t = 30$, no classification boost gained by adding topological features in either dimensions when testing Utrecht DB and

splicing technique. In fact, in figure (7-5) well before $t = 30$ the classification accuracy stabilises and become consistent.
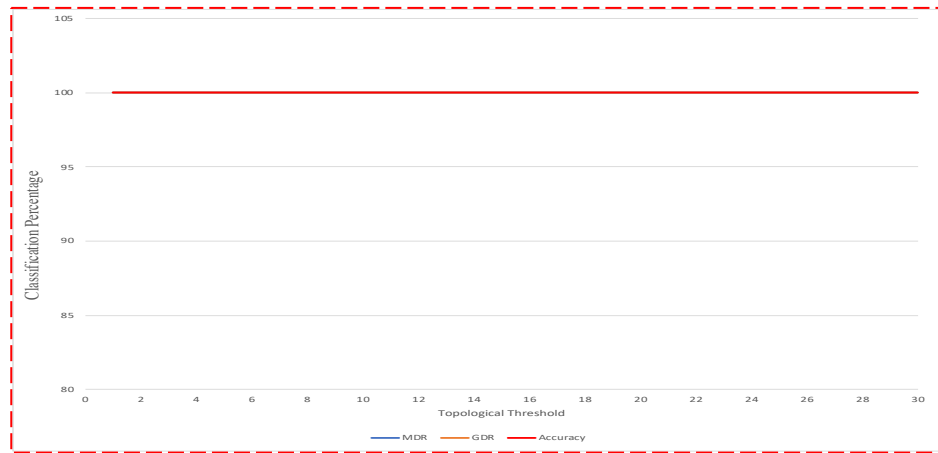
Figure 7-7: Accuracy Trend of combined-Utrecht DB that shows the effect of increasing topological features at dimension zero and one.
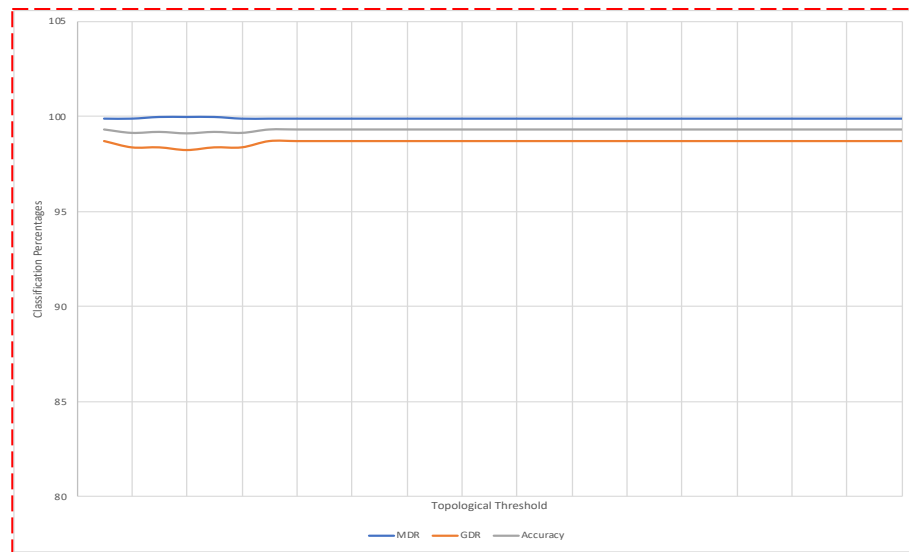

Figure 7-8: Accuracy Trend of complete-Utrecht DB that shows the effect of increasing topological features at dimension zero**.**

142
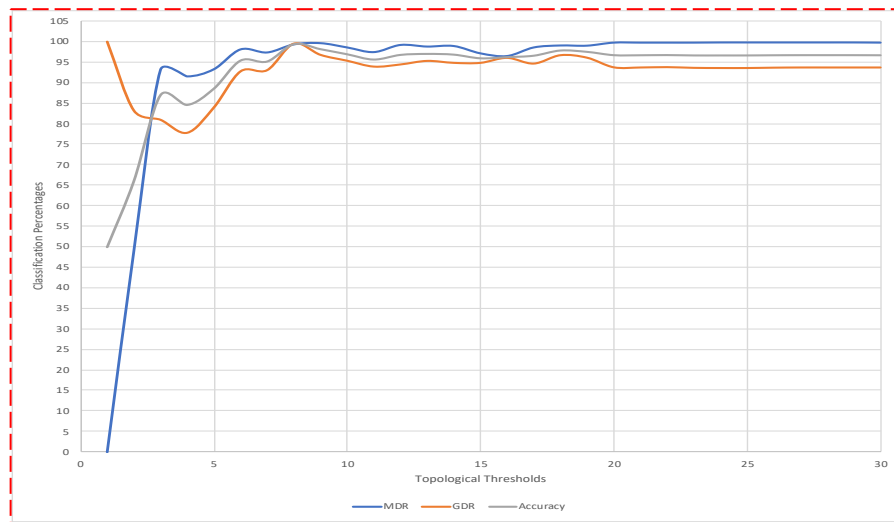
Figure 7-9: Accuracy Trend of complete-Utrecht DB that shows the effect of increasing topological features at dimension one.

Figures (7-7) to (7-9) shows the classification trend of Utrecht DB, using 2ULBP landmark, and the best geometries for each morphing technique detection. The reason behind inconsistent scales of y-axis in the figures is only to zoom-in the effect of adding more features to the classification performance. It is consistent that in Utrecht DB, morphed face detection performance is not increasing after $t = 30$ which means that instead of using topological features of 800-dimension, using only 240-dimensional topological feature vector is enough in practise. Next, we demonstrate the London DB accuracy trend, through figures (7-10) to (7-15).
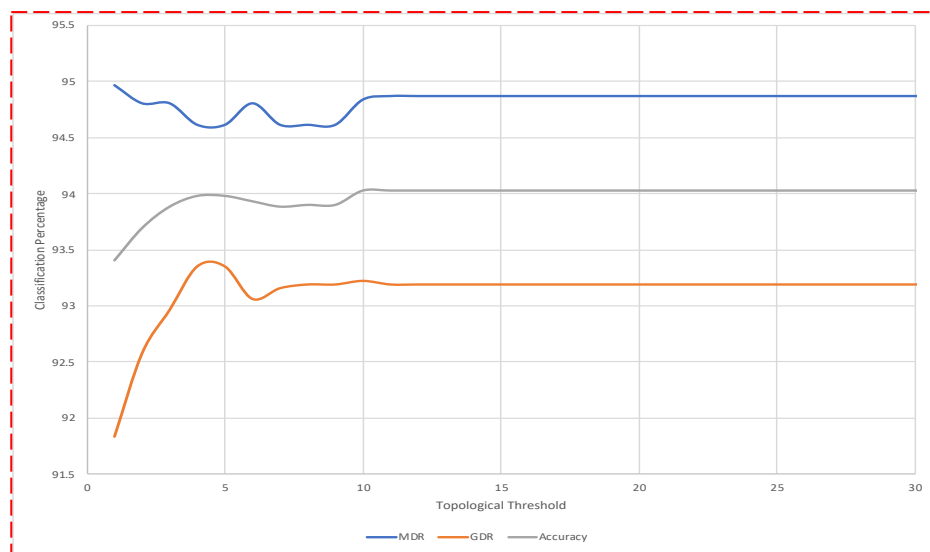
Figure 7-10: Accuracy Trend of splicing-London DB that shows the effect of increasing topological features at dimension zero. The landmark used is 2ULBP and the geometry is G_4.

143
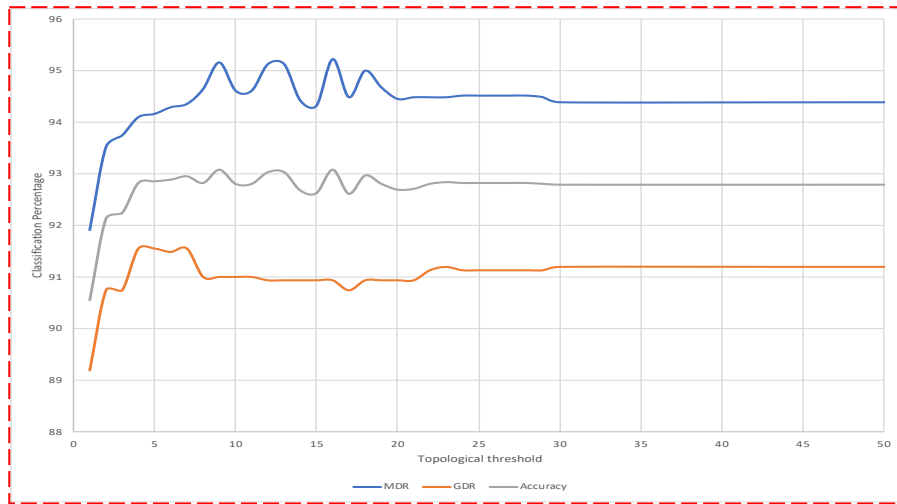
Figure 7-11: Accuracy Trend of splicing-London DB that shows the effect of increasing topological features at dimension one. The landmark used is 2ULBP and the geometry is G_4.
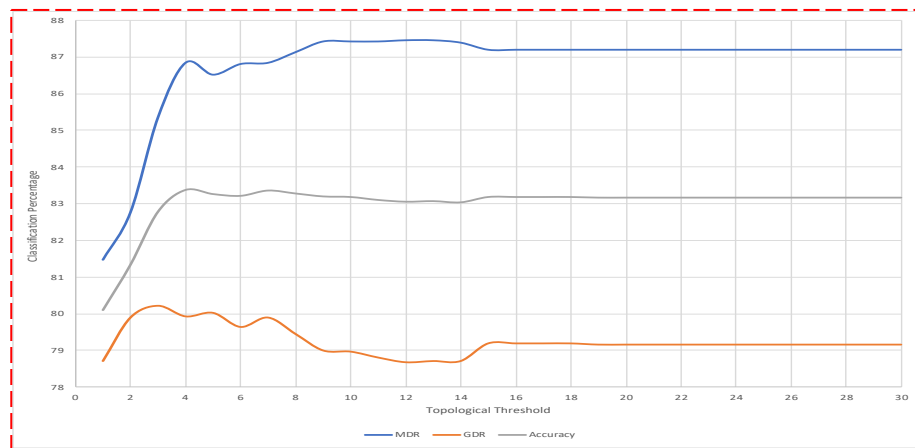
Figure 7-12: Accuracy Trend of combine-London DB that shows the effect of increasing topological features at dimension zero. The landmark used is 2ULBP and the geometry is G_5.
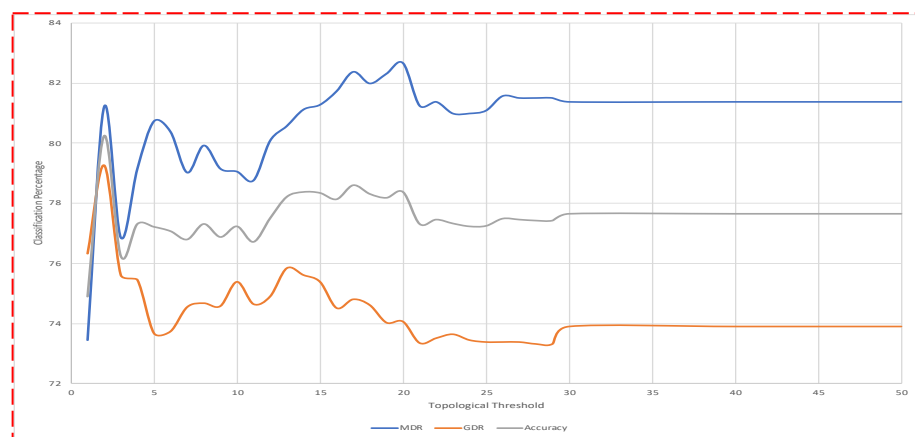
Figure 7-13: Accuracy Trend of combine-London DB that shows the effect of increasing topological features at dimension one. The landmark used is 2ULBP and the geometry is G_5.

144
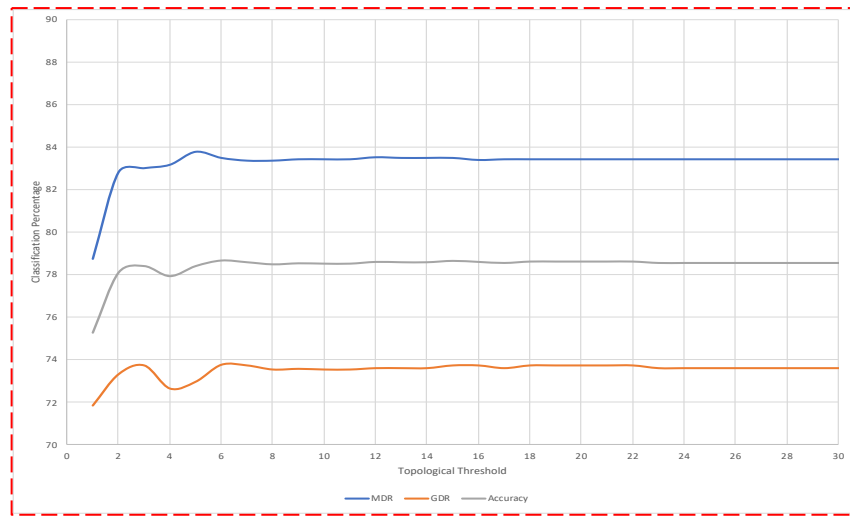
Figure 7-14: Accuracy Trend of complete-London DB that shows the effect of increasing topological features at dimension zero. The landmark used is 2ULBP and the geometry is G_5.
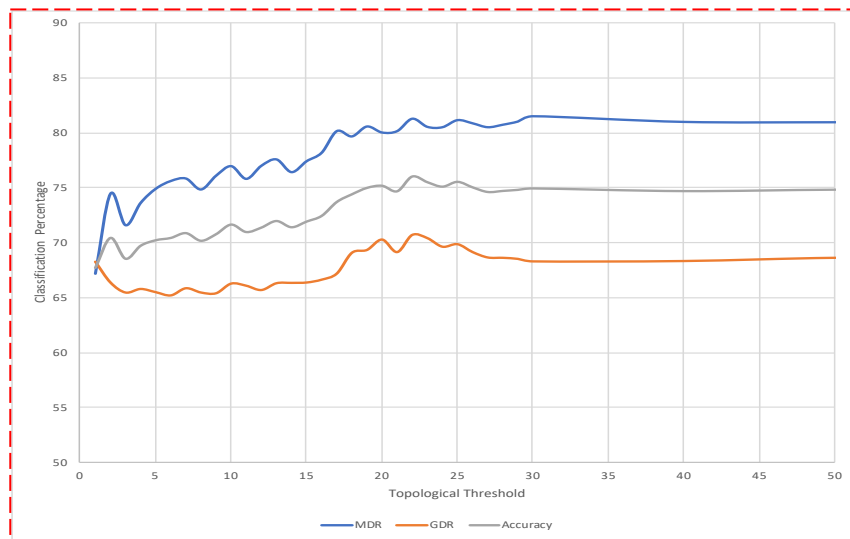

Figure 7-15: Accuracy Trend of complete-London DB that shows the effect of increasing topological features at dimension one. The landmark used is 2ULBP and the geometry is G_5.

In London DB, similar to Utrecht DB, classification performance is not increasing after $t = 30$, across all three morphing techniques of splicing, combine and complete morphing. It is worth to note that, Utrecht DB classification performance converges sooner to than London DB but in both datasets beyond $t = 30$ no gain achieved in the classification. Albeit the fact that the pick of the classification performance is not at $t = 30$, but no consistent region can be determined at this stage to be considered for the

145

persistent classification performance. Of course, this claim needs to be validated in future by testing a larger number of face images to determine a universal stopping criterion/threshold to construct persistent barcodes.

4- Persistent Vertex Degree (Local homology): Throughout our study, we focused on global homology features of the constructed simplicial complexes and ignored parameters like distribution of vertex degree within the connected components. However, we noted these distributions are somewhat sensitive to image tampering and may provide effective forensic tools. In fact two Rips complexes with the same number of connected components or number of holes/loops, may have locally different distributions of vertex degree (for example see figure (6-2), figure (6-10) and figure (6-11) in Chapter 6). Accordingly, computing the persistent (vertex) degree at each vertex (i.e. landmark pixel) is another future work to extend our current investigation into such local homology parameters.

5- Extending the set of Landmarks to construct other topological structures: Another obvious future direction to the work presented in this thesis is the extension of the set of landmarks used to build topologies from images. In our analysis, we have used $LBP_{(8,1)}$ where 8 refers to the eight neighbouring pixels and 2 refers to the radius of the selected circle selected. One can repeat the same analysis using other types of LBP such as $LBP_{(8,2)}$, $LBP_{(16,2)}$, $LBP_{(4,1)}$ and others. Further, we can also use what is known as threshold-based LBP, whereby instead of ≥ 0 condition in LBP, we impose an extra condition by changing the threshold from zero to a chosen threshold by the user. Local derivative patterns [165], entropy of image pixels or image patches and selecting image pixel landmarks according to patch intensity statistics distribution …etc.

6- One of the challenges in developing robust morph detection algorithms in passport scenarios is the lack of publicly available datasets that could help mitigating the problem of overfitting as we discussed in chapter 5. In an attempt to do so, our collaborators in Germany made morphed faces from both Utrecht and London DB that is publicly available in (https://omen.cs.uni-magdeburg.de/disclaimer/index.php). One need to re-evaluate the performance of our PH-base schemes in such cases and perhaps contribute to the effort of producing larger datasets by gathering a larger dataset of diverse

passport images and generate corresponding morphs. One other related issue is that in passport scenarios, the quality of produced morphed face images are expected to be more convincing and visually faultless, if it were to avoid detection by border control officers. In this respect, we note that passport images are meant to be taken in a controlled illumination environment and in border checking it may be difficult to produce perfect illumination conditions. This may result in high and undesirable false rejections. This is a strong motivation to investigate the effect of varying illumination on PH-based morph detection.

7- Testing our PH-based steganalysis approach on more steganographic methods is another future work as well as comparing our topology steganalysis with other steganalysis techniques which are mostly statistical based. Furthermore, in this thesis, we considered 100% payload of the secret message whereby we use the entire carrier image pixels to embed, we plan to extend this to lower rate of payloads such as 90%, 80%, 70%, …, 10% payload. This means, instead of using/changing all of cover images' pixel values, we only change say 10% of the pixel values which makes the task of stego detection harder.

8- Using our approach of building more than one topology from a single medical image demonstrated a viable potential for more analysis in future, especially improving the results obtained from DDSM dataset. In our analysis, LBP has been selected as the landmark selection, we shall investigate the use of R-LBP, CS-LBP and concatenation of different landmarks and geometries of the same landmark to improve the breast tumour classification. Furthermore, we also plan to extend the work on other types of medical images, other than mammograms, such as Ultrasound images as well as other types of cancer.

References

[1]   G. Carlsson, "TOPOLOGY AND DATA," *Bull. New. Ser. Am. Math. Soc.*, vol. 46, no. 209, pp. 255–308, 2009.

[2]   N. Srivastava, G. Hinton, A. Krizhevsky, and R. Salakhutdinov, "Dropout: A Simple Way to Prevent Neural Networks from Overfitting," *J. Mach. Learn. Res.*, vol. 15, pp. 1929–1958, 2014.

[3]   L. H. Gilpin, D. Bau, B. Z. Yuan, A. Bajwa, M. Specter, and L. Kagal, "Explaining explanations: An overview of interpretability of machine learning," in *Proceedings - 2018 IEEE 5th International Conference on Data Science and Advanced Analytics, DSAA 2018*, 2019, pp. 80–89.

[4]   D. N. Reshef *et al.*, "Detecting Novel Associations in Large Data Sets," *Science (80-.).*, vol. 334, no. 6062, pp. 1518–1524, Dec. 2011.

[5]   N. Al-Hassan, "Mathematically inspired approaches to face recognition in uncontrolled conditions: super resolution and compressive sensing," The University of Buckingham, 2014.

[6]   T. Hassan, "Data-independent vs. data-dependent dimension reduction for pattern recognition in high dimensional spaces," The University of Buckingham, 2017.

[7]   G. Carlsson, T. Ishkhanov, V. de Silva, and A. Zomorodian, "On the Local Behavior of Spaces of Natural Images," *Int. J. Comput. Vis.*, vol. 76, no. 1, pp. 1–12, Jan. 2008.

[8]   A. B. Lee, K. S. Pedersen, and D. Mumford, "The nonlinear statistics of high-contrast patches in natural images," *Int. J. Comput. Vis.*, vol. 54, no. 1–3, pp. 83–103, Aug. 2003.

[9]   D. Al-Karawi, "Texture Analysis based machine learning algorithms for ultrasound ovarian tumour classification within clinical practices," The university of Buckingham, 2019.

[10]   M. Nicolau, A. J. Levine, and G. Carlsson, "Topology based data analysis

identifies a subgroup of breast cancers with a unique mutational profile and excellent survival," *Proc. Natl. Acad. Sci.*, vol. 108, no. 17, pp. 7265–7270, Apr. 2011.

[11] F. Belchi, M. Pirashvili, J. Conway, M. Bennett, R. Djukanovic, and J. Brodzki, "Lung Topology Characteristics in patients with Chronic Obstructive Pulmonary Disease," *Nat. Sci. Reports*, vol. 8, no. 1, p. 5341, Dec. 2018.

[12] J. Lamar-León, E. B. García-Reyes, and R. Gonzalez-Diaz, "Human gait identification using persistent homology," in *Lecture Notes in Computer Science (including subseries Lecture Notes in Artificial Intelligence and Lecture Notes in Bioinformatics)*, 2012.

[13] J. Munkres, *Elements of Algebraic Topology*, 1st ed. California: Addison-Wiley, 1984.

[14] A. Hatcher, *Algebraic topology*. Cambridge University Press, 2002.

[15] A. Zomorodian, *Topology for Computing*. Cambridge University Press, 2005.

[16] R. Ghrist, *ELEMENTARY APPLIED TOPOLOGY*, 1.0. Createspace, 2014.

[17] Google, "sphere , torus and klein bottle - Google Search," *Google Images*, 2019. [Online]. Available: https://www.google.co.uk/search. [Accessed: 18-Nov-2019].

[18] J. M. Montesinos-Amilibia, *Classical Tessellations and Three-Manifolds*. Berlin, Heidelberg: Springer Berlin Heidelberg, 1987.

[19] "Fathom the Universe: Rolled up dimensions," 2019. [Online]. Available: https://fathom-the-universe.tumblr.com/post/58140859428/rolled-up-dimensions-this-is-a-projection-of. [Accessed: 18-Nov-2019].

[20] B. Fischl, A. Liu, and A. M. Dale, "Automated manifold surgery: Constructing geometrically accurate and topologically correct models of the human cerebral cortex," *IEEE Trans. Med. Imaging*, vol. 20, no. 1, pp. 70–80, Jan. 2001.

[21] P. Y. Lum *et al.*, "Extracting insights from the shape of complex data using topology," *Sci. Rep.*, vol. 3, no. 1, p. 1236, Dec. 2013.

[22] V. Nanda and R. Sazdanović, "Simplicial models and topological inference in biological systems," in *Natural Computing Series*, vol. 48, Springer, Berlin, Heidelberg, 2014, pp. 109–141.

[23] E. H. Spanier, *Algebraic Topology*. New York, NY: Springer New York, 1981.

[24] Jeff Erickson, "Computational Topology - Homology," *University of illinois.* [Online]. Available: http://jeffe.cs.illinois.edu/teaching/comptop/2009/notes/homology.pdf.

[25] K. Glen Wang, "THE BASIC THEORY OF PERSISTENT HOMOLOGY," *University of Chicago.* [Online]. Available: http://math.uchicago.edu/~may/REU2012/REUPapers/WangK.pdf.

[26] J. Erickson, "Computational Topology -Homology," *University of illinois.* [Online]. Available: http://jeffe.cs.illinois.edu/teaching/comptop/2009/notes/homology.pdf.

[27] N. Otter, M. A. Porter, U. Tillmann, P. Grindrod, and H. A. Harrington, "A roadmap for the computation of persistent homology," *arXiv*, Jun. 2015.

[28] K. Mischaikow and V. Nanda, "Morse Theory for Filtrations and Efficient Computation of Persistent Homology," *Discrete Comput. Geom.*, vol. 50, no. 2, pp. 330–353, Sep. 2013.

[29] U. Bauer, "Ripser," *online-Github*, 2016. [Online]. Available: https://github.com/Ripser/ripser. [Accessed: 24-Jun-2019].

[30] H. Adams, A. Tausz, and M. Vejdemo-Johansson, "javaPlex: A Research Software Package for Persistent (Co)Homology," Springer, Berlin, Heidelberg, 2014, pp. 129–136.

[31] U. Bauer, M. Kerber, and J. Reininghaus, "Distributed Computation of Persistent Homology," in *2014 Proceedings of the Sixteenth Workshop on Algorithm Engineering and Experiments (ALENEX)*, Philadelphia, PA: Society for Industrial and Applied Mathematics, 2014, pp. 31–38.

[32] "Dionysus." [Online]. Available: https://www.mrzv.org/software/dionysus/. [Accessed: 24-Jun-2019].

[33] C. Maria, J.-D. Boissonnat, M. Glisse, and M. Yvinec, "The Gudhi Library: Simplicial Complexes and Persistent Homology," Springer, Berlin, Heidelberg, 2014, pp. 167–174.

[34] J. Binchi, M. Rucco, G. Petri, and F. Vaccarino, "jHoles: A Tool for Understanding Biological Complex Networks via Clique Weight Rank Persistent Homology," *Electron. Notes Theor. Comput. Sci.*, vol. 306, pp. 5–18, Jul. 2014.

[35] D. Cohen-Steiner, H. Edelsbrunner, and J. Harer, "Stability of Persistence Diagrams," *Discrete Comput. Geom.*, vol. 37, no. 1, pp. 103–120, Jan. 2007.

[36] R. Ghrist, "Barcodes: The persistent topology of data," in *Bulletin of the American Mathematical Society*, 2008, vol. 45, no. 1, pp. 61–75.

[37] F. Chazal and B. Michel, "An introduction to Topological Data Analysis: fundamental and practical aspects for data scientists," *arXiv*, Oct. 2017.

[38] E. Munch, "A User's Guide to Topological Data Analysis.," *J. Learn. Anal.*, vol. 4, no. 2, pp. 47–61, 2017.

[39] G. R. Bowman *et al.*, "Structural insight into RNA hairpin folding intermediates," *J. Am. Chem. Soc.*, vol. 130, no. 30, pp. 9676–9678, Jul. 2008.

[40] B. Rieck and H. Leitte, "Persistent Homology for the Evaluation of Dimensionality Reduction Schemes," *Comput. Graph. Forum*, vol. 34, no. 3, pp. 431–440, Jun. 2015.

[41] V. de Silva and R. Ghrist, "Coverage in sensor networks via persistent homology," *Algebr. Geom. Topol.*, vol. 7, no. 1, pp. 339–358, Apr. 2007.

[42] M. Gameiro, Y. Hiraoka, S. Izumi, M. Kramar, K. Mischaikow, and V. Nanda, "A topological measurement of protein compressibility," *Jpn. J. Ind. Appl. Math.*, vol. 32, no. 1, pp. 1–17, Mar. 2015.

[43] V. Kovacev-Nikolic, P. Bubenik, D. Nikolić, and G. Heo, "Using persistent homology and dynamical distances to analyze protein binding," *arXiv*, Dec. 2014.

[44] A. H. Rizvi *et al.*, "Single-cell topological RNA-seq analysis reveals insights

into cellular differentiation and development," *Nat. Biotechnol.*, vol. 35, no. 6, pp. 551–560, Jun. 2017.

[45] N. Singh, H. D. Couture, J. S. Marron, C. Perou, and M. Niethammer, "Topological Descriptors of Histology Images," Springer, Cham, 2014, pp. 231–239.

[46] J. Lamar-León, E. B. García-Reyes, and R. Gonzalez-Diaz, "Human Gait Identification Using Persistent Homology," Springer, Berlin, Heidelberg, 2012, pp. 244–251.

[47] J. Lamar-Leon, R. Alonso-Baryolo, E. Garcia-Reyes, and R. Gonzalez-Diaz, "Persistent homology-based gait recognition robust to upper body variations," in *2016 23rd International Conference on Pattern Recognition (ICPR)*, 2016, pp. 1083–1088.

[48] J. L. Leon, A. Cerri, E. G. Reyes, and R. G. Diaz, "Gait-Based Gender Classification Using Persistent Homology," Springer, Berlin, Heidelberg, 2013, pp. 366–373.

[49] J. Lamar-Leon, R. A. Baryolo, E. Garcia-Reyes, and R. Gonzalez-Diaz, "Gait-Based Carried Object Detection Using Persistent Homology," Springer, Cham, 2014, pp. 836–843.

[50] P. Bendich, J. S. Marron, E. Miller, A. Pieloch, and S. Skwerer, "Persistent Homology Analysis of Brain Artery Trees.," *Ann. Appl. Stat.*, vol. 10, no. 1, pp. 198–218, 2016.

[51] C. Curto, "What can topology tell us about the neural code?," *Bull. Am. Math. Soc.*, vol. 54, no. 1, pp. 63–78, Sep. 2016.

[52] P. Dotko *et al.*, "TOPOLOGICAL ANALYSIS OF THE CONNECTOME OF DIGITAL RECONSTRUCTIONS OF NEURAL MICROCIRCUITS," *arXiv*, 2016.

[53] C. Giusti, R. Ghrist, and D. S. Bassett, "Two's company, three (or more) is a simplex," *J. Comput. Neurosci.*, vol. 41, no. 1, pp. 1–14, Aug. 2016.

[54] L. Kanari *et al.*, "Quantifying topological invariants of neuronal

morphologies," *arXiv*, 2016.

[55] M. Ferri, "Progress in Persistence for Shape Analysis (Extended Abstract)," Springer, Cham, 2016, pp. 3–6.

[56] C. S. Pun, K. Xia, and S. X. Lee, "Persistent-Homology-based Machine Learning and its Applications -- A Survey," *arXiv*, Nov. 2018.

[57] F. A. Khasawneh and E. Munch, "Chatter detection in turning using persistent homology," *Mech. Syst. Signal Process.*, vol. 70–71, pp. 527–541, Mar. 2016.

[58] F. A. Khasawneh, E. Munch, and J. A. Perea, "Chatter Classification in Turning using Machine Learning and Topological Data Analysis," *IFAC-PapersOnLine*, vol. 51, no. 14, pp. 195–200, Jan. 2018.

[59] N. Giansiracusa, R. Giansiracusa, and C. Moon, "Persistent homology machine learning for fingerprint classification," *arXiv*, Nov. 2017.

[60] Z. Cang, L. Mu, K. Wu, K. Opron, K. Xia, and G.-W. Wei, "A topological approach for protein classification," *arXiv*, Oct. 2015.

[61] S. Kališnik, "Tropical Coordinates on the Space of Persistence Barcodes," *Found. Comput. Math.*, vol. 19, no. 1, pp. 101–129, Feb. 2019.

[62] B. Zielinski, M. Lipinski, M. Juda, M. Zeppelzauer, and P. Dlotko, "Persistence Codebooks for Topological Data Analysis," *arXiv*, Feb. 2018.

[63] P. Bubenik, "The persistence landscape and some of its properties," *arXiv*, Oct. 2018.

[64] H. Adams *et al.*, "Persistence Images: A Stable Vector Representation of Persistent Homology," *J. Mach. Learn. Res.*, vol. 18, no. 1, pp. 218–252, Jul. 2017.

[65] I. Chevyrev, V. Nanda, and H. Oberhauser, "Persistence paths and signature features in topological data analysis," *IEEE Trans. Pattern Anal. Mach. Intell.*, Jun. 2018.

[66] G. Singh, F. Mémoli, and G. Carlsson, "Topological Methods for the Analysis of High Dimensional Data Sets and 3D Object Recognition," *Eurographics*

Symp. Point-Based Graph., pp. 91–100, 2007.

[67] F. Belchí, J. Brodzki, M. Burfitt, and M. Niranjan, "A numerical measure of the instability of Mapper-type algorithms," *arXiv*, Jun. 2019.

[68] M. Nicolau, A. J. Levine, and G. Carlsson, "Topology based data analysis identifies a subgroup of breast cancers with a unique mutational profile and excellent survival.," *Proc. Natl. Acad. Sci. U. S. A.*, vol. 108, no. 17, pp. 7265–70, Apr. 2011.

[69] L. De Cecco *et al.*, "Head and neck cancer subtypes with biological and clinical relevance: Meta-analysis of gene-expression data.," *Oncotarget*, vol. 6, no. 11, pp. 9627–42, Apr. 2015.

[70] D. Romano *et al.*, "Topological methods reveal high and low functioning neuro-phenotypes within fragile X syndrome.," *Hum. Brain Mapp.*, vol. 35, no. 9, pp. 4904–15, Sep. 2014.

[71] T. S. C. Hinks *et al.*, "Innate and adaptive T cells in asthmatic patients: Relationship to severity and disease mechanisms.," *J. Allergy Clin. Immunol.*, vol. 136, no. 2, pp. 323–33, Aug. 2015.

[72] T. S. C. Hinks *et al.*, "Multidimensional endotyping in patients with severe asthma reveals inflammatory heterogeneity in matrix metalloproteinases and chitinase 3-like protein 1.," *J. Allergy Clin. Immunol.*, vol. 138, no. 1, pp. 61–75, 2016.

[73] J. P. R. Schofield *et al.*, "Stratification of asthma phenotypes by airway proteomic signatures.," *J. Allergy Clin. Immunol.*, vol. 144, no. 1, pp. 70–82, Jul. 2019.

[74] J. L. Nielson *et al.*, "Topological data analysis for discovery in preclinical spinal cord injury and traumatic brain injury," *Nat. Commun.*, vol. 6, Oct. 2015.

[75] P. G. Cámara, "Topological methods for genomics: Present and future directions," *Current Opinion in Systems Biology*, vol. 1. Elsevier Ltd, pp. 95–101, 01-Feb-2017.

[76] J. M. Chan, G. Carlsson, and R. Rabadan, "Topology of viral evolution," *Proc. Natl. Acad. Sci. U. S. A.*, vol. 110, no. 46, pp. 18566–18571, Nov. 2013.

[77] G. Sarikonda *et al.*, "CD8 T-cell reactivity to islet antigens is unique to type 1 while CD4 T-cell reactivity exists in both type 1 and type 2 diabetes.," *J. Autoimmun.*, vol. 50, pp. 77–82, May 2014.

[78] L. Li *et al.*, "Identification of type 2 diabetes subgroups through topological analysis of patient similarity.," *Sci. Transl. Med.*, vol. 7, no. 311, p. 311ra174, Oct. 2015.

[79] L. Duponchel, "Exploring hyperspectral imaging data sets with topological data analysis," *Anal. Chim. Acta*, vol. 1000, pp. 123–131, Feb. 2018.

[80] Y. Lee, S. D. Barthel, P. Dłotko, S. M. Moosavi, K. Hess, and B. Smit, "Quantifying similarity of pore-geometry in nanoporous materials," *Nat. Commun.*, vol. 8, May 2017.

[81] M. Pirashvili, L. Steinberg, F. Belchi Guillamon, M. Niranjan, J. G. Frey, and J. Brodzki, "Improved understanding of aqueous solubility modeling through topological data analysis," *J. Cheminform.*, vol. 10, no. 1, Nov. 2018.

[82] M. Kamruzzaman, A. Kalyanaraman, B. Krishnamoorthy, S. Hey, and P. Schnable, "Hyppo-X: A Scalable Exploratory Framework for Analyzing Complex Phenomics Data," *arXiv*, Jul. 2017.

[83] L. Duponchel, "When remote sensing meets topological data analysis," *J. Spectr. Imaging*, vol. 7, 2018.

[84] A. Savic, G. Toth, and L. Duponchel, "Topological data analysis (TDA) applied to reveal pedogenetic principles of European topsoil system.," *Sci. Total Environ.*, vol. 586, pp. 1091–1100, May 2017.

[85] M. Carrière, B. Michel, and S. Oudot, "Statistical Analysis and Parameter Selection for Mapper," *arXiv*, Jun. 2017.

[86] G. Carlsson, T. Ishkhanov, V. De Silva, and A. Zomorodian, "On the local behavior of spaces of natural images," *Int. J. Comput. Vis.*, vol. 76, no. 1, pp. 1–12, Jan. 2008.

[87] V. Kurlin, "A fast persistence-based segmentation of noisy 2D clouds with provable guarantees," *Pattern Recognit. Lett.*, vol. 83, pp. 3–12, Nov. 2016.

[88] T. Qaiser, K. Sirinukunwattana, K. Nakane, Y. W. Tsang, D. Epstein, and N. Rajpoot, "Persistent Homology for Fast Tumor Segmentation in Whole Slide Histology Images," in *Procedia Computer Science*, 2016, vol. 90, pp. 119–124.

[89] P. Lawson, A. B. Sholl, J. Q. Brown, B. T. Fasy, and C. Wenk, "Persistent Homology for the Quantitative Evaluation of Architectural Features in Prostate Cancer Histology," *Sci. Rep.*, vol. 9, no. 1, p. 1139, Dec. 2019.

[90] T. Ojala, M. Pietikäinen, and D. Harwood, "A comparative study of texture measures with classification based on featured distributions," *Pattern Recognit.*, vol. 29, no. 1, pp. 51–59, Jan. 1996.

[91] T. Ahonen, A. Hadid, and M. Pietikäinen, "Face Recognition with Local Binary Patterns," Springer, Berlin, Heidelberg, 2004, pp. 469–481.

[92] T. Ojala, M. Pietikainen, and T. Maenpaa, "Multiresolution gray-scale and rotation invariant texture classification with local binary patterns," *IEEE Trans. Pattern Anal. Mach. Intell.*, vol. 24, no. 7, pp. 971–987, Jul. 2002.

[93] A. T. Asaad, R. D. Rashid, and S. A. Jassim, "Topological image texture analysis for quality assessment," in *Proceedings of SPIE - The International Society for Optical Engineering*, 2017, vol. 10221.

[94] R. Gonzalez and R. Woods, *Digital Image Processing*, 3rd ed. New Jersey: Pearson, 2008.

[95] A. Makrushin, T. Neubert, and J. Dittmann, "Automatic Generation and Detection of Visually Faultless Facial Morphs," in *Proc. of the 12th Int. Joint Conf. on Comp Vision, Imaging and Comp. Graphics Theory and Apps.*, 2017, pp. 39–50.

[96] G. Wolberg and George, *Digital image warping*. IEEE Computer Society Press, 1990.

[97] M. Ferrara, A. Franco, and D. Maltoni, "Face Demorphing," *IEEE Trans. Inf. Forensics Secur.*, vol. 13, no. 4, pp. 1008–1017, Apr. 2018.

156

[98]   A. Asaad and S. Jassim, "Topological Data Analysis for image tampering detection," *Lect. Notes Comput. Sci.*, vol. 10431 LNCS, 2017.

[99]   A. Makrushin, C. Kraetzer, T. Neubert, and J. Dittmann, "Generalized Benford's Law for Blind Detection of Morphed Face Images," in *Proceedings of the 6th ACM Workshop on Information Hiding and Multimedia Security - IH&MMSec '18*, 2018, pp. 49–54.

[100] P. Hancock, "Psychological Image Collection at Stirling (PICS)-2D face sets," *Utrecht ECVP http://pics.stir.ac.uk/2D_face_sets.htm*. [Online]. Available: http://pics.stir.ac.uk/2D_face_sets.htm. [Accessed: 17-Jan-2018].

[101] R. Raghavendra, K. B. Raja, and C. Busch, "Detecting morphed face images," in *2016 IEEE 8th International Conference on Biometrics Theory, Applications and Systems, BTAS 2016*, 2016.

[102] International Air Transport Association, "IATA - Automated Border Control Implementation." [Online]. Available: http://www.iata.org/whatwedo/passenger/Pages/automated-border-control.aspx. [Accessed: 11-Jan-2018].

[103] M. Ferrara, A. Franco, and D. Maltoni, "The magic passport," in *IEEE International Joint Conference on Biometrics*, 2014, pp. 1–7.

[104] U. Scherhag, R. Raghavendra, K. B. Raja, M. Gomez-Barrero, C. Rathgeb, and C. Busch, "On the vulnerability of face recognition systems towards morphed face attacks," in *Proceedings - 2017 5th International Workshop on Biometrics and Forensics, IWBF 2017*, 2017.

[105] D. J. Robertson, R. S. S. Kramer, and A. M. Burton, "Fraudulent ID using face morphs: Experiments on human and automatic recognition," *PLoS One*, vol. 12, no. 3, 2017.

[106] A. Makrushin, T. Neubert, and J. Dittmann, "Humans Vs. Algorithms: Assessment of Security Risks Posed by Facial Morphing to Identity Verification at Border Control - VISIGRAPP 2019," in *14th VISAPP19*, 2019.

[107] A. Makrushin, T. Neubert, and J. Dittmann, "Humans Vs. Algorithms: Assessment of Security Risks Posed by Facial Morphing to Identity

Verification at Border Control - VISIGRAPP 2019," in *14th VISAPP19*, 2019.

[108] M. Hildebrandt, T. Neubert, A. Makrushin, and J. Dittmann, "Benchmarking face morphing forgery detection: Application of stirtrace for impact simulation of different processing steps," in *Proceedings - 2017 5th International Workshop on Biometrics and Forensics, IWBF 2017*, 2017.

[109] T. Neubert, "Face Morphing Detection: An Approach Based on Image Degradation Analysis," in *Lecture Notes in Computer Science*, vol. 10431, Magdeburg, Germany.: Springer, Cham, 2017, pp. 93–106.

[110] T. Neubert, A. Makrushin, M. Hildebrandt, C. Kraetzer, and J. Dittmann, "Extended StirTrace benchmarking of biometric and forensic qualities of morphed face images," *IET Biometrics*, vol. 7, no. 4, pp. 325–332, Jul. 2018.

[111] T. Neubert, C. Kraetzer, and J. Dittmann, "Reducing the False Alarm Rate for Face Morph Detection by a Morph Pipeline Footprint Detector," in *2018 26th European Signal Processing Conference (EUSIPCO)*, 2018, pp. 1002–1006.

[112] C. Kraetzer, A. Makrushin, T. Neubert, M. Hildebrandt, and J. Dittmann, "Modeling Attacks on Photo-ID Documents and Applying Media Forensics for the Detection of Facial Morphing," in *Proceedings of the 5th ACM Workshop on Information Hiding and Multimedia Security - IHMMSec '17*, 2017, pp. 21–32.

[113] B. Amos, B. Ludwiczuk, and M. Satyanarayanan, "OpenFace: A general-purpose face recognition library with mobile applications," 2016.

[114] L.-B. Zhang, F. Peng, and M. Long, "Face Morphing Detection Using Fourier Spectrum of Sensor Pattern Noise," in *2018 IEEE International Conference on Multimedia and Expo (ICME)*, 2018, pp. 1–6.

[115] R. Raghavendra, K. Raja, S. Venkatesh, and C. Busch, "Face morphing versus face averaging: Vulnerability and detection," in *2017 IEEE International Joint Conference on Biometrics (IJCB)*, 2017, pp. 555–563.

[116] N. Damer, A. M. Saladie, A. Braun, and A. Kuijper, "MorGAN: Recognition Vulnerability and Attack Detectability of Face Morphing Attacks Created by Generative Adversarial Network," in *2018 IEEE 9th International Conference*

on Biometrics Theory, Applications and Systems (BTAS), 2018, pp. 1–10.

[117] L. Wandzik, G. Kaeding, and R. V. Garcia, "Morphing Detection Using a General- Purpose Face Recognition System," in *2018 26th European Signal Processing Conference (EUSIPCO)*, 2018, pp. 1012–1016.

[118] U. Scherhag, C. Rathgeb, and C. Busch, "Morph Detection from Single Face Image," in *Proceedings of the 2018 2nd International Conference on Biometric Engineering and Applications - ICBEA '18*, 2018, pp. 6–12.

[119] C. Seibold, A. Hilsmann, and P. Eisert, "Reflection Analysis for Face Morphing Attack Detection," in *2018 26th European Signal Processing Conference (EUSIPCO)*, 2018, pp. 1022–1026.

[120] K. Simonyan and A. Zisserman, "Very Deep Convolutional Networks for Large-Scale Image Recognition," *arXiv*, Sep. 2014.

[121] A. Krizhevsky, A. Krizhevsky, I. Sutskever, and G. E. Hinton, "Imagenet classification with deep convolutional neural networks," *Adv. Neural Inf. Process. Syst.*, p. 2012.

[122] R. Raghavendra, K. B. Raja, S. Venkatesh, and C. Busch, "Transferable Deep-CNN Features for Detecting Digital and Print-Scanned Morphed Face Images," in *IEEE Computer Society Conference on Computer Vision and Pattern Recognition Workshops*, 2017, vol. 2017-July, pp. 1822–1830.

[123] C. Seibold, W. Samek, A. Hilsmann, and P. Eisert, "Detection of Face Morphing Attacks by Deep Learning," Springer, Cham, 2017, pp. 107–120.

[124] C. Szegedy *et al.*, "Going Deeper with Convolutions," in *Proceedings of the IEEE Computer Society Conference on Computer Vision and Pattern Recognition*, 2015, pp. 1–9.

[125] O. M. Parkhi, A. Vedaldi, and A. Zisserman, "Deep Face Recognition," in *Proceedings of the British Machine Vision Conference (BMVC)*, 2015, pp. 41.1-41.12.

[126] F. Schroff, D. Kalenichenko, and J. Philbin, "FaceNet: A Unified Embedding for Face Recognition and Clustering," *arXiv*, Mar. 2015.

[127] M. Ferrara, A. Franco, and D. Maltoni, "Face demorphing in the presence of facial appearance variations," in *2018 26th European Signal Processing Conference (EUSIPCO)*, 2018, pp. 2365–2369.

[128] U. Scherhag, D. Budhrani, M. Gomez-Barrero, and C. Busch, "Detecting Morphed Face Images Using Facial Landmarks," Springer, Cham, 2018, pp. 444–452.

[129] T. Cover and P. Hart, "Nearest neighbor pattern classification," *IEEE Trans. Inf. Theory*, vol. 13, no. 1, pp. 21–27, Jan. 1967.

[130] T. Ahonen, A. Hadid, and M. Pietikainen, "Face Description with Local Binary Patterns: Application to Face Recognition," *IEEE Trans. Pattern Anal. Mach. Intell.*, vol. 28, no. 12, pp. 2037–2041, Dec. 2006.

[131] Ren and Malik, "Learning a classification model for segmentation," in *Proceedings Ninth IEEE International Conference on Computer Vision*, 2003, pp. 10–17 vol.1.

[132] B. Fulkerson, A. Vedaldi, and S. Soatto, "Class segmentation and object localization with superpixel neighborhoods," in *IEEE 12th Inter. Conf. on Computer Vision*, 2010, pp. 670–677.

[133] M. Heikkilä, M. Pietikäinen, and C. Schmid, "Description of interest regions with local binary patterns," *Pattern Recognit.*, vol. 42, no. 3, pp. 425–436, Mar. 2009.

[134] L. DeBruine and B. Jones, "Face Research Lab London Set," *figshare*, 2017. [Online]. Available: https://figshare.com/articles/Face_Research_Lab_London_Set/5047666. [Accessed: 21-Feb-2019].

[135] F. T. Liu, K. M. Ting, and Z. H. Zhou, "Isolation-based anomaly detection," *ACM Trans. Knowl. Discov. Data*, vol. 6, no. 1, Mar. 2012.

[136] S. Hariri, M. C. Kind, and R. J. Brunner, "Extended Isolation Forest," *arXiv*, Nov. 2018.

[137] R. D. Rashid, H. Sellahewa, and S. A. Jassim, "Biometric feature embedding

using robust steganography technique," in *Proceedings Volume 8755, Mobile Multimedia/Image Processing, Security, and Applications.*, 2013, vol. 8755, p. 875503.

[138] V. Sedighi, J. Fridrich, and R. Cogranne, "Content-adaptive pentary steganography using the multivariate generalized Gaussian cover model," in *Proceedings Volume 9409, Media Watermarking, Security, and Forensics 2015*, 2015, p. 94090H.

[139] R. D. Rashid, "Robust Steganographic Techniques for Secure Biometric-based Romote Authenntication," The University of Buckingham, 2015.

[140] A. T. Asaad, S. A. Jassim, and R. D. Rashid, "Topological data analysis as image steganalysis technique," in *Mobile Multimedia/Image Processing, Security, and Applications 2018*, 2018, vol. 10668, p. 17.

[141] P. Bas, T. Filler, and T. Pevný, "'Break our steganographic system': The ins and outs of organizing BOSS," in *Lecture Notes in Computer Science (including subseries Lecture Notes in Artificial Intelligence and Lecture Notes in Bioinformatics)*, 2011, vol. 6958 LNCS, pp. 59–70.

[142] A. A. Al-Jaberi, "An evaluation of partial differential equations based digital inpainting algorithms," The University of Buckingham, 2019.

[143] A. Criminisi, P. Perez, and K. Toyama, "Region Filling and Object Removal by Exemplar-Based Image Inpainting," *IEEE Trans. Image Process.*, vol. 13, no. 9, pp. 1200–1212, Sep. 2004.

[144] N. S. and N. Mehta, "Region Filling and Object Removal by Exempeler Based Image Inpainting," *Int. J. Inven. Eng. Sci.*, vol. 1, no. 3, pp. 26–31, 2013.

[145] W.-H. Cheng, C.-W. Hsieh, S.-K. Lin, C.-W. Wang, and J.-L. Wu, "Robust Algorithm for Exemplar-based Image Inpainting," in *Process. Int. Conf. Comput. Graph*, 2005, pp. 64–69.

[146] M. Desai, "Modified Fast and Enhanced Exemplar based Inpainting Algorithm for Solving Unknown Row Filling problem," *Int. J. Comput. Appl.*, vol. 56, no. 9, pp. 20–24, Oct. 2012.

[147] Anupam, P. Goyal, and S. Diwakar, "Fast and enhanced algorithm for exemplar based image inpainting," in *Proceedings - 4th Pacific-Rim Symposium on Image and Video Technology, PSIVT 2010*, 2010, pp. 325–330.

[148] S. Hesabi and N. Mahdavi-Amiri, "A modified patch propagation-based image inpainting using patch sparsity," in *AISP 2012 - 16th CSI International Symposium on Artificial Intelligence and Signal Processing*, 2012, pp. 43–48.

[149] K. S. P. Sengottuvelan and E. Balamurugan, "A Novel Exemplar based Image Inpainting Algorithm for Natural Scene Image Completion with Improved Patch Prioritizing," *Int. J. Comput. Appl.*, vol. 36, no. 4, pp. 1–6, 2011.

[150] W. and V. A. P. J.M, "Region Filling and Object Removal by ExemplarBased Image Inpainting," *Int. J. Sci. Eng. Res.*, vol. 3, no. 1, pp. 1–6, 2012.

[151] Z. Xu and J. Sun, "Image inpainting by patch propagation using patch sparsity," *IEEE Trans. Image Process.*, vol. 19, no. 5, pp. 1153–1165, May 2010.

[152] M. J. A. and S. Kalantar, "Gradient-Based Search Space Reduction for Fast Exemplar-Based Image Inpainting," in *International Conference on New Research Achievements in Electrical and Computer Engineering*, 2016, pp. 1–6.

[153] L.-J. Deng, T.-Z. Huang, and X.-L. Zhao, "Exemplar-Based Image Inpainting Using a Modified Priority Definition," *PLoS One*, vol. 10, no. 10, p. e0141199, Oct. 2015.

[154] M. Cimpoi, S. Maji, I. Kokkinos, S. Mohamed, and A. Vedaldi, "Describing textures in the wild," in *Proceedings of the IEEE Computer Society Conference on Computer Vision and Pattern Recognition*, 2014.

[155] T. Majeed, "Segmentation, Super-resolution and Fusion for Digital Mammogram Classification," The University of Buckingham, 2016.

[156] U. Department of Health, "What Is Cancer?," 2019. [Online]. Available: http://www.cancer.gov/cancertopics/cancerlibrary/what-is-cancer. [Accessed: 09-Dec-2019].

[157] "Breast cancer statistics | Cancer Research UK." [Online]. Available: https://www.cancerresearchuk.org/health-professional/cancer-statistics/statistics-by-cancer-type/breast-cancer. [Accessed: 09-Dec-2019].

[158] Y. M. Elshinawy, "Pre-cad normal mammogram detection algorithm based on tissue type," Howard University, 2010.

[159] J. Suckling *et al.*, "Mammographic Image Analysis Society (MIAS) database," *The University of Cambridge*, 2015. [Online]. Available: https://www.repository.cam.ac.uk/handle/1810/250394. [Accessed: 20-Sep-2012].

[160] M. Heath, K. Bowyer, D. Kopans, R. Moore, and P. Kegelmeyer, "The digital database for screening mammography," in *Proceedings of the Fifth International Workshop on Digital Mammography*, 2001, pp. 212–218.

[161] W. Lab, "FaceApp," 2017. [Online]. Available: https://faceapp.com/app. [Accessed: 20-Aug-2019].

[162] "DeepFaceLab." [Online]. Available: https://github.com/iperov/DeepFaceLab. [Accessed: 11-Jul-2019].

[163] Y. Li, M.-C. Chang, and S. Lyu, "In Ictu Oculi: Exposing AI Generated Fake Face Videos by Detecting Eye Blinking," *arXiv*, 2018.

[164] D. Guera and E. J. Delp, "Deepfake Video Detection Using Recurrent Neural Networks," in *Proceedings of AVSS 2018 - 2018 15th IEEE International Conference on Advanced Video and Signal-Based Surveillance*, 2019.

[165] B. Zhang, Y. Gao, S. Zhao, and J. Liu, "Local derivative pattern versus local binary pattern: Face recognition with high-order local pattern descriptor," *IEEE Trans. Image Process.*, vol. 19, no. 2, pp. 533–544, Feb. 2010.